

A molecular cross-linking approach for hybrid metal oxides

Dahee Jung^{1,2}, Liban M. A. Saleh¹, Zachariah J. Berkson³, Maher F. El-Kady^{1,2}, Jee Youn Hwang¹, Nahla Mohamed^{1,4}, Alex I. Wixtrom¹, Ekaterina Titarenko¹, Yanwu Shao¹, Kassandra McCarthy¹, Jian Guo⁵, Ignacio B. Martini¹, Stephan Kraemer⁶, Evan C. Wegener⁷, Philippe Saint-Cricq¹, Bastian Rühle¹, Ryan R. Langeslay⁸, Massimiliano Delferro⁹, Jonathan L. Brosmer¹⁰, Christopher H. Hendon⁹, Marcus Gallagher-Jones^{1,2}, Jose Rodriguez^{1,2}, Karena W. Chapman¹⁰, Jeffrey T. Miller⁷, Xiangfeng Duan^{1,2}, Richard B. Kaner^{1,2,5}, Jeffrey I. Zink^{1,2}, Bradley F. Chmelka³ and Alexander M. Spokoyny^{1,2*}

There is significant interest in the development of methods to create hybrid materials that transform capabilities, in particular for Earth-abundant metal oxides, such as TiO₂, to give improved or new properties relevant to a broad spectrum of applications. Here we introduce an approach we refer to as ‘molecular cross-linking’, whereby a hybrid molecular boron oxide material is formed from polyhedral boron-cluster precursors of the type [B₁₂(OH)₁₂]²⁻. This new approach is enabled by the inherent robustness of the boron-cluster molecular building block, which is compatible with the harsh thermal and oxidizing conditions that are necessary for the synthesis of many metal oxides. In this work, using a battery of experimental techniques and materials simulation, we show how this material can be interfaced successfully with TiO₂ and other metal oxides to give boron-rich hybrid materials with intriguing photophysical and electrochemical properties.

Rapid global industrialization has led to a high stress on terrestrial elemental resources, particularly for elements that are capable of mediating transformative processes¹. As a consequence, oxides of elements such as iron, silicon, titanium and aluminium are extremely attractive as they are Earth abundant, and their use has impacted a number of diverse and important areas, including energy storage², catalysis³ and light harvesting⁴. However, despite their importance, the capability of these metal oxides to mediate transformative processes is limited, and the ability to fine-tune the properties of these materials through mild and operationally straightforward methods remains challenging, because there are a limited number of techniques available to do so^{4–7}. As an example, titanium dioxide (TiO₂) has attracted significant attention in the field of renewable energy, due to its potential as a photocatalyst for important transformations, such as solar energy to electricity and water splitting^{8–10}. However, its wide optical bandgap (~3.2 eV) renders it extremely inefficient as it can only capture ultraviolet light and excludes visible light, which makes up 50% of the solar spectrum⁷. To maximize the light-absorptive capabilities of TiO₂, the oxide may be subjected to various chemical modifications (Fig. 1a). Most efforts have focused on the use of molecular organic and inorganic dyes to sensitize the surface of the oxide (Fig. 1a, approach i), elemental doping with light elements (approach ii) or defect engineering (approach iii)^{4,6,11–13}.

By analogy with elemental doping, we hypothesized that it should be possible to cross-link robust molecules made of light elements

within a framework of a metal oxide material. Such an endeavour would be prohibitive if restricted to more fragile organic molecules, such as those used to dope organic semiconductors¹⁴ and are inherently unstable under most conditions required to prepare oxides that require prolonged annealing at >500 °C in air, such as crystalline TiO₂ (ref. 4). We therefore viewed polyhedral boron-rich clusters as being potentially suitable molecules for such an undertaking (Fig. 1b), in particular, the anionic dodecaborate cluster (B₁₂H₁₂²⁻), a three-dimensional (3D) aromatic analogue of benzene^{15–23}. The π electrons in benzene are delocalized over 2D, whereas the π electrons in dodecaborate are delocalized in 3D over the entire molecule. These unique properties result in a highly robust molecular scaffold, withstanding temperatures as high as 600 °C and resistant towards strong acids and bases^{16,24}. We hypothesized that this combination of properties would allow the unprecedented cross-linking of intact molecules to oxide materials, as they would be able to withstand the harsh preparation conditions. Here we report the first successful synthesis of a hybrid boron-cluster-containing boron oxide material using this ‘molecular cross-linking’ strategy, as well as its ability to interface with metal oxides. Importantly, this method creates a material with dramatically altered photophysical and electrochemical properties.

Hybrid molecular boron oxide materials

We focused on the use of the perhydroxylated derivative of dodecaborate, [B₁₂(OH)₁₂]²⁻ (Fig. 1b, referred to as 1 in Supplementary Information),

¹Department of Chemistry and Biochemistry, University of California, Los Angeles, Los Angeles, CA, USA. ²California NanoSystems Institute (CNSI), University of California, Los Angeles, Los Angeles, CA, USA. ³Department of Chemical Engineering, University of California, Santa Barbara, Santa Barbara, CA, USA. ⁴Department of Chemistry, Faculty of Science, Cairo University, Giza, Egypt. ⁵Department of Materials Science and Engineering, University of California, Los Angeles, Los Angeles, CA, USA. ⁶Materials Research Center, University of California, Santa Barbara, Santa Barbara, CA, USA. ⁷Davidson School of Chemical Engineering, Purdue University, West Lafayette, IN, USA. ⁸Chemical Sciences and Engineering Division, Argonne National Laboratory, Argonne, IL, USA. ⁹Department of Chemistry and Biochemistry, University of Oregon, Eugene, OR, USA. ¹⁰X-ray Science Division, Advanced Photon Source, Argonne National Laboratory, Argonne, IL, USA. *e-mail: spokoyny@chem.ucla.edu

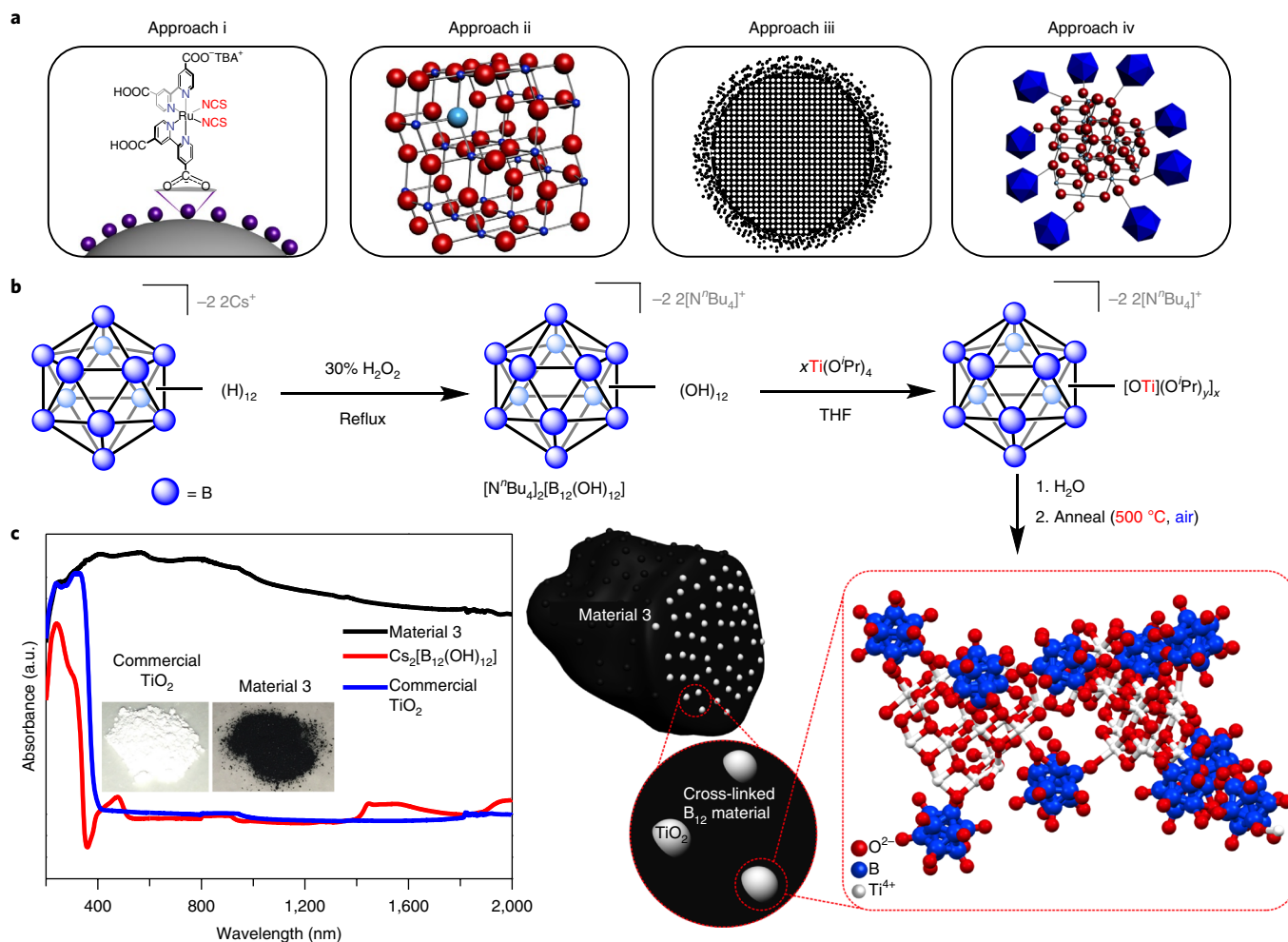


Fig. 1 | Overview of existing modification methods compared with molecular cross-linking and the preparation of molecularly cross-linked TiO_2 (3).

a, Different approaches for the chemical modification of metal oxides: use of organic and inorganic dyes to sensitize metal oxide surfaces (i); elemental doping of metal oxides with light elements to induce changes in their bulk properties (ii); the introduction of defects in ordered crystalline metal oxides to change their optical properties (iii); and, in this work, a molecular cross-linking approach, whereby whole molecules are interfaced with metal oxides to effect changes in their photo- and electrochemical properties (iv). **b**, Synthetic route towards the synthesis of material 3 that utilizes the robust polyhedral boron cluster $[N^mBu_4]_2[B_{12}(OH)_{12}]$ as a key precursor. **c**, Diffuse-reflectance UV-vis data for material 3, plotted alongside data for TiO_2 and $Cs_2[B_{12}(OH)_{12}]$ to highlight the dramatic difference in light-absorption properties of all three materials (left); simplified, non-rigorous model that depicts the proposed structure of the hybrid molecular boron oxide material 3 (right), and the calculated local structure (inset). a.u., arbitrary units.

as a precursor due to its amenability to further functionalization²⁵. Thermogravimetric analysis (TGA) of the salt $Cs_2[B_{12}(OH)_{12}]$ was carried out to assess the general robustness of the cluster, and revealed minimal mass loss for $Cs_2[B_{12}(OH)_{12}]$ up to $900^\circ C$ (Supplementary Fig. 1). A similar analysis of the more synthetically useful derivative $[N^mBu_4]_2[B_{12}(OH)_{12}]$ was not possible because of its strongly hygroscopic nature, and so a bulk sample of $[N^mBu_4]_2[B_{12}(OH)_{12}]$ was annealed at $500^\circ C$ in air, with the intention to analyse the product by other methods. We were surprised to recover a black powder (referred to herein as material 2) rather than the expected white material as in the case of $Cs_2[B_{12}(OH)_{12}]$. This is extremely unusual, as the vast majority of boron-rich clusters are white powders and, to the best of our knowledge, there currently does not exist any material that contains boron and oxygen and is black. Intrigued by the uniquely intense colour of material 2, we subjected the sample to diffuse-reflectance ultraviolet-visible (UV-vis) spectroscopic analysis. Material 2 demonstrated absorption from the ultraviolet range all the way to the near infrared (NIR) range (Supplementary Fig. 2). Material 2 was probed further by powder X-ray diffraction (PXRD), scanning electron

microscopy (SEM) and transmission electron microscopy (TEM) to acquire its structural information (Supplementary Figs. 2 and 3). X-ray photoelectron spectroscopy (XPS) analysis was employed to probe the elemental composition on the surface of material 2, excluding the presence of elemental boron (Supplementary Fig. 4). A cross-linked polymer of intact clusters and boron oxide had been formed, and effectively trapped the carbon-containing fragments before they could combust in air during the annealing process (Supplementary Fig. 5 and Supplementary Table 1).

With the hybrid molecular boron oxide material 2 in hand, we explored the possibility of interfacing material 2 with Earth-abundant metal oxide nanoparticles, focusing on TiO_2 . This interfacing would potentially engender properties not normally found in boron-rich materials. Given that the previous effort to interface $[N^mBu_4]_2[B_{12}(OH)_{12}]$ with organic functional groups via perfunctionalization led to $[B_{12}(OR)_{12}]^{2-}$ motifs featuring B–O–C bonding connectivities^{25–28}, we hypothesized that one could develop a strategy that leads to the formation of B–O–Ti interactions from $[B_{12}(OH)_{12}]^{2-}$. A common precursor for the synthesis of TiO_2 is titanium

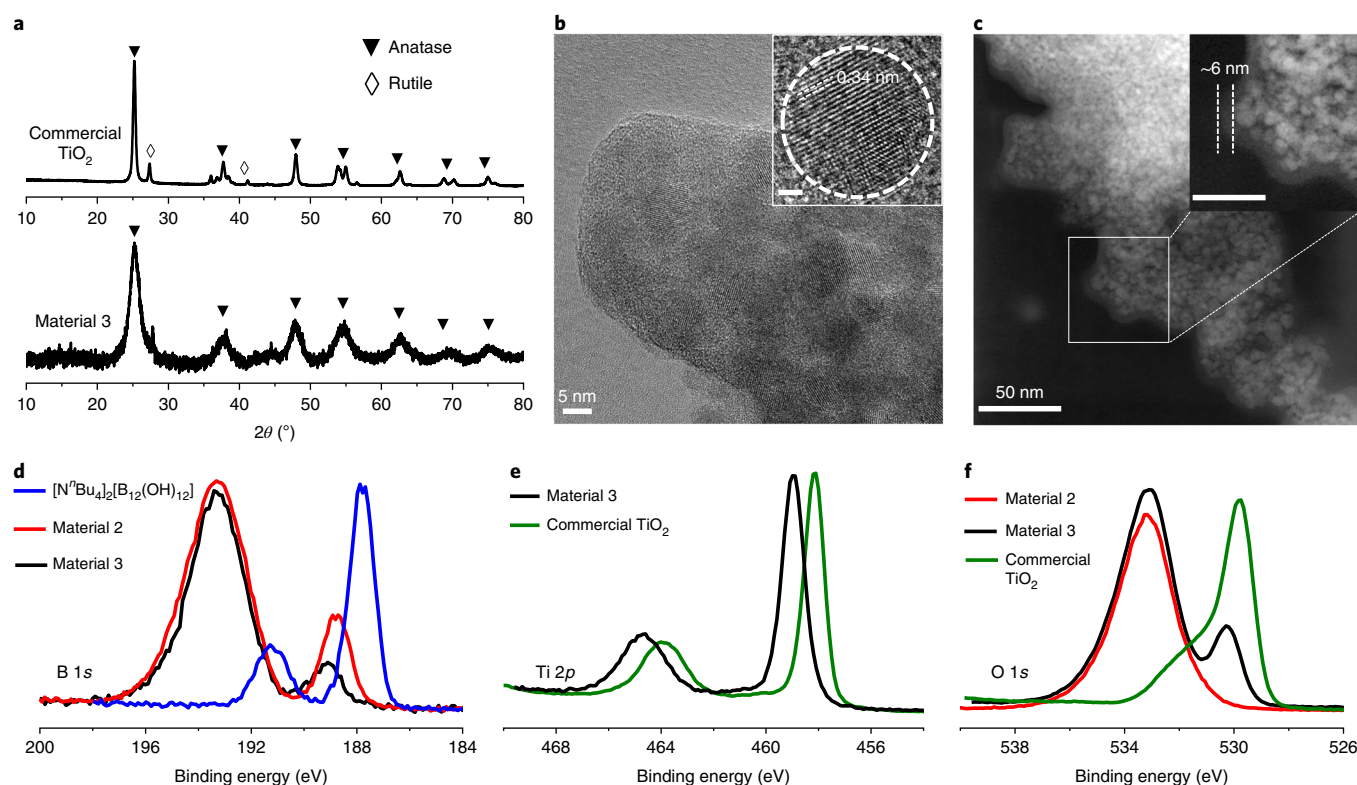


Fig. 2 | Structural data for material 3. **a**, PXRD of commercial TiO_2 and material 3 revealed the presence of crystalline TiO_2 in the anatase phase, which is the expected phase when annealed at 500°C , with the broadness of the peaks indicative of very small crystalline domains. **b**, TEM image of material 3. The inset shows the HRTEM of a crystalline TiO_2 domain free of disorder in material 3 (inset scale bar, 2 nm). **c**, STEM image of material 3 that highlights the densely packed TiO_2 nanoparticles embedded in material 2. The inset shows an expansion of the outer amorphous layer in material 3, attributed to material 2 (inset scale bar, 25 nm). **d**, The boron 1s region of $[\text{N}^t\text{Bu}_4]_2[\text{B}_{12}(\text{OH})_{12}]$ shows two peaks at 187.8 eV and 191.2 eV, which can be explained by the ability of $[\text{B}_{12}(\text{OH})_{12}]^{2-}$ and its derivatives to access multiple well-defined oxidation states (main text gives the details). For materials 2 and 3, the boron 1s region contains a peak at 189.2 eV that corresponds to an intact cluster, and another at 193.1 eV that corresponds to boron oxide. The about +2 eV change in binding energy observed for the peak associated with the intact cluster in materials 2 and 3 compared with $[\text{N}^t\text{Bu}_4]_2[\text{B}_{12}(\text{OH})_{12}]$ can be attributed to the intact cluster being more oxidized, possibly as a mixture of 2- and 1- oxidation states. **e**, The titanium 2p region of material 3 shows peaks at 459.1 eV and 464.8 eV, respectively, slightly shifted from those of pristine TiO_2 , but indicative of Ti^{4+} . **f**, The oxygen 1s region for TiO_2 , materials 2 and 3.

tetraisopropoxide ($\text{Ti}(\text{O}^i\text{Pr})_4$), an air and moisture sensitive liquid. Controlled hydrolysis of this liquid, followed by annealing at the appropriate temperature is a common route to produce various phases of crystalline TiO_2 (ref. 4). We hypothesized that reacting $[\text{N}^t\text{Bu}_4]_2[\text{B}_{12}(\text{OH})_{12}]$ with $\text{Ti}(\text{O}^i\text{Pr})_4$ would result in protonolysis, the elimination of isopropyl alcohol and the formation of a B–O–Ti linkage (Fig. 1b). A test reaction mixture of $[\text{N}^t\text{Bu}_4]_2[\text{B}_{12}(\text{OH})_{12}]$ with $\text{Ti}(\text{O}^i\text{Pr})_4$ was subjected to a ^1H solution NMR spectroscopic analysis, and the resultant spectrum clearly showed the presence of isopropyl alcohol (Supplementary Fig. 6), which verifies a B–O–Ti bond formation. The reaction of $[\text{N}^t\text{Bu}_4]_2[\text{B}_{12}(\text{OH})_{12}]$ with $\text{Ti}(\text{O}^i\text{Pr})_4$ produces a clear red–orange solution, which was subsequently hydrolysed to form a red–orange gel (Supplementary Fig. 7). After calcining at 120°C , the now dark–orange solid was annealed at 500°C in air to produce material 3 as a shiny black solid, which contrasted sharply with the white colour of both pristine TiO_2 and the pre-annealed $[\text{N}^t\text{Bu}_4]_2[\text{B}_{12}(\text{OH})_{12}]$ (Fig. 1c). Material 3 is remarkably stable, as evidenced by our inability to dissolve it even after prolonged exposure to a variety of organic solvents, strong acids, strong bases and 3% H_2O_2 , consistent with its hypothesized highly cross-linked composition (Supplementary Fig. 8).

Structural characterizations of material 3

Diffuse-reflectance UV–vis spectroscopic analysis of material 3 produced similar results to that found for material 2, with a strong

and sustained absorption from the ultraviolet to NIR range (Fig. 1c). Structural information for material 3 was then obtained from PXRD, SEM (Supplementary Fig. 9) and high-resolution TEM (HRTEM) (Fig. 2 and Supplementary Fig. 10). The PXRD of material 3 provides evidence for crystalline anatase TiO_2 , and the HRTEM images display crystalline TiO_2 domains with no evidence of disorder (Fig. 2b, inset). Further evidence for anatase is provided by selected area electron diffraction and *d*-spacing measurements (Supplementary Fig. 11). Additional structural information was provided by scanning TEM (STEM) (Fig. 2c) and a 3D reconstruction (Supplementary Fig. 12), providing a cross-sectional view of the material, depicted as a model in Fig. 1c. Specifically, densely embedded TiO_2 nanocrystals are observed, with an additional ~ 6 nm thick band of amorphous material on the edges, which is attributed to the interfaced material 2. To interrogate the content of the amorphous component in material 3, we first examined this material using Raman spectroscopy. The six Raman active modes for anatase TiO_2 (ref. 12) were not detected, and instead only bands associated with the boron cluster at 1,370 and 1,600 cm^{-1} were observed (Supplementary Fig. 13), which suggests that the TiO_2 is not present in any significant quantity on the surface of material 3. XPS measurements of material 3 were carried out, with the measurements of $[\text{N}^t\text{Bu}_4]_2[\text{B}_{12}(\text{OH})_{12}]$ and TiO_2 providing benchmark values (Fig. 2d–f). The boron 1s region reveals the presence of intact boron clusters at 189.2 eV and boron oxide at 193.1 eV

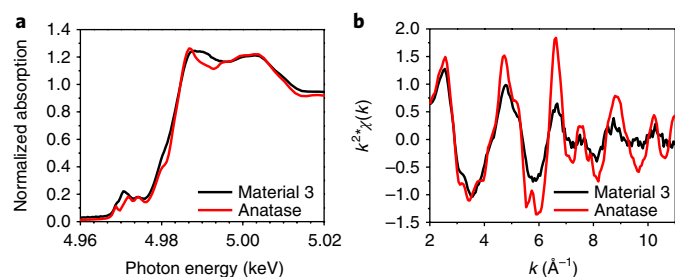


Fig. 3 | XANES and EXAFS data for anatase TiO_2 and material 3. **a**, XANES measurements on material 3 were compared with those measured for anatase TiO_2 . The Ti K edge structure for material 3 matches that found for anatase, which confirms the presence of anatase with titanium exclusively in the 4+ oxidation state. **b**, The k -squared weighted EXAFS function of material 3 and anatase. From these data, an average Ti–O bond distance of 1.95 Å for TiO_2 in material 3 can be extracted, which is expected for TiO_2 in the anatase phase.

(Fig. 2d and Supplementary Fig. 14). The higher binding energy for the intact clusters in material 3 suggests they are more oxidized than the clusters in the starting material $[\text{N}^n\text{Bu}_4]_2[\text{B}_{12}(\text{OH})_{12}]$, which

have a lower binding energy of 187.8 eV (Fig. 2d). XPS also shows the presence of residual carbon at 284.5 eV in the sample despite annealing in air at 500 °C (Supplementary Fig. 15). Although some of the carbon content can be attributed to the unavoidable presence of adventitious carbon from the air, combustion analysis confirmed the presence of ~8.7% carbon in the material, assigned as graphitic carbon based on the XPS binding energy (Supplementary Table 2). The appearance of graphitic carbon suggests a likely templating effect imposed by the clusters, reminiscent of the cross-linked ‘molecular frameworks’ recently reported^{29,30}, albeit with significantly lower carbon content in the case of material 3. To clarify the proposed trapping events during the synthesis and annealing processes that led to material 3, we subjected pre-annealed material 3 to TGA–mass spectroscopy (MS) analysis measured in air (Supplementary Figs. 16–18). The experimental conditions to form material 3 favour retaining carbon despite the high temperatures and oxygenated atmosphere, which ultimately suggests trapping through templation (Supplementary Table 3).

As the penetration depth of the XPS beam reaches ~10 nm, titanium 2p peaks could be observed for material 3 (Fig. 2e), consistent with the presence of Ti(IV) in the sample. To confirm the oxidation state of Ti in bulk 3, X-ray absorption near-edge spectroscopy (XANES) measurements were performed (Fig. 3, summarized in

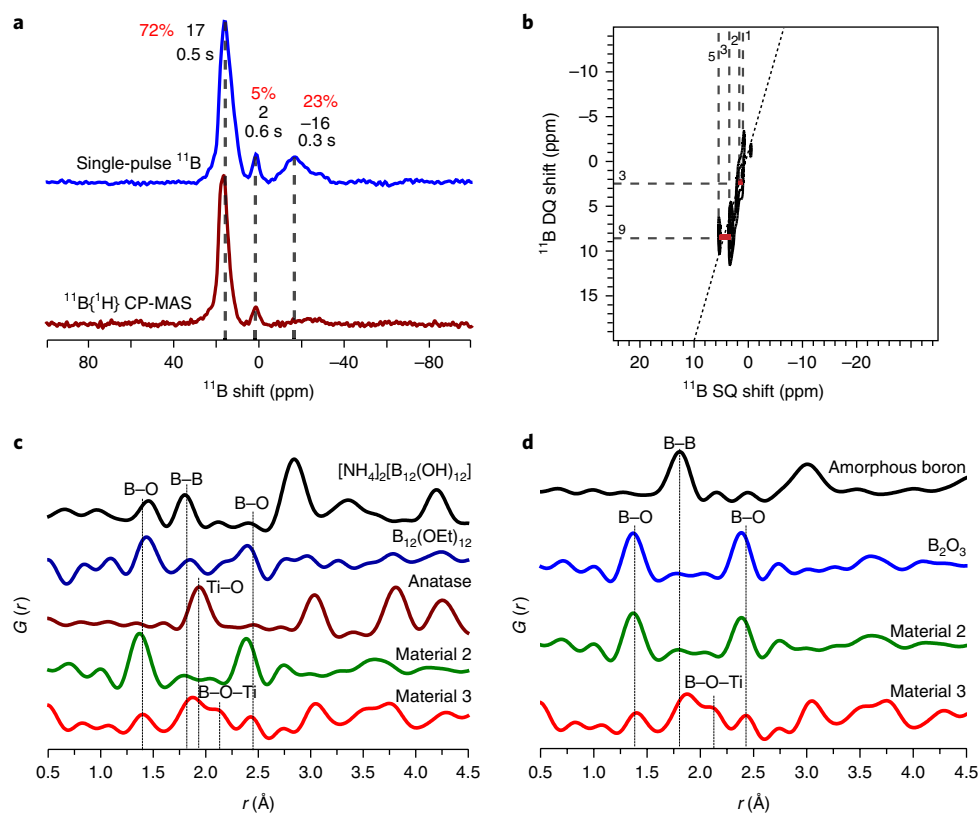


Fig. 4 | Solid-state ^{11}B MAS NMR and PDF analysis. **a**, Solid-state 1D single-pulse ^{11}B MAS NMR (top) and $^{11}\text{B}\{^1\text{H}\}$ CP-MAS (bottom) spectra of material 3 acquired at 18.8 T and 298 K that show three resolved ^{11}B signals at –16, 2 and 17 ppm, assigned to subsurface boron clusters, surface boron clusters and boron oxide/borates, with relative percentages of 23, 5 and 72%, respectively. **b**, 2D J -mediated (through-bond) $^{11}\text{B}\{^{11}\text{B}\}$ correlation spectrum of material 3. Correlated ^{11}B signals detected across the double-diagonal dotted line establish unambiguously the through-bond covalent connectivities of distinct ^{11}B species. The correlated signal pairs at ^{11}B (SQ,DQ) shifts of (5 ppm, 9 ppm) and (3 ppm, 9 ppm) and (2 ppm, 3 ppm) and (1 ppm, 3 ppm) (red lines) provide direct evidence of ^{11}B – ^{11}B bonds in material 3. **c**, PDF analysis of materials 2 and 3, directly compared with $[\text{NH}_4]_2[\text{B}_{12}(\text{OH})_{12}]$ and $[\text{B}_{12}(\text{OEt})_{12}]$ controls to provide data on B–O and B–B bond distances in intact clusters in various oxidation states, and anatase TiO_2 to assess directly the Ti–O bond distances. Clear correlations can be observed, which confirm the presence of both B–O and B–B bonds in materials 2 and 3; that there are B–B bonds is significant as they are diagnostic for the presence of intact clusters. **d**, Additional PDF analysis of materials 2 and 3 with B_2O_3 and amorphous elemental boron controls to provide data on the B–O and B–B bond distances in the oxide and element, respectively. Although the PDF analyses for material 2 and B_2O_3 look superficially similar, more careful observation reveals the presence of B–B bonds in material 2.

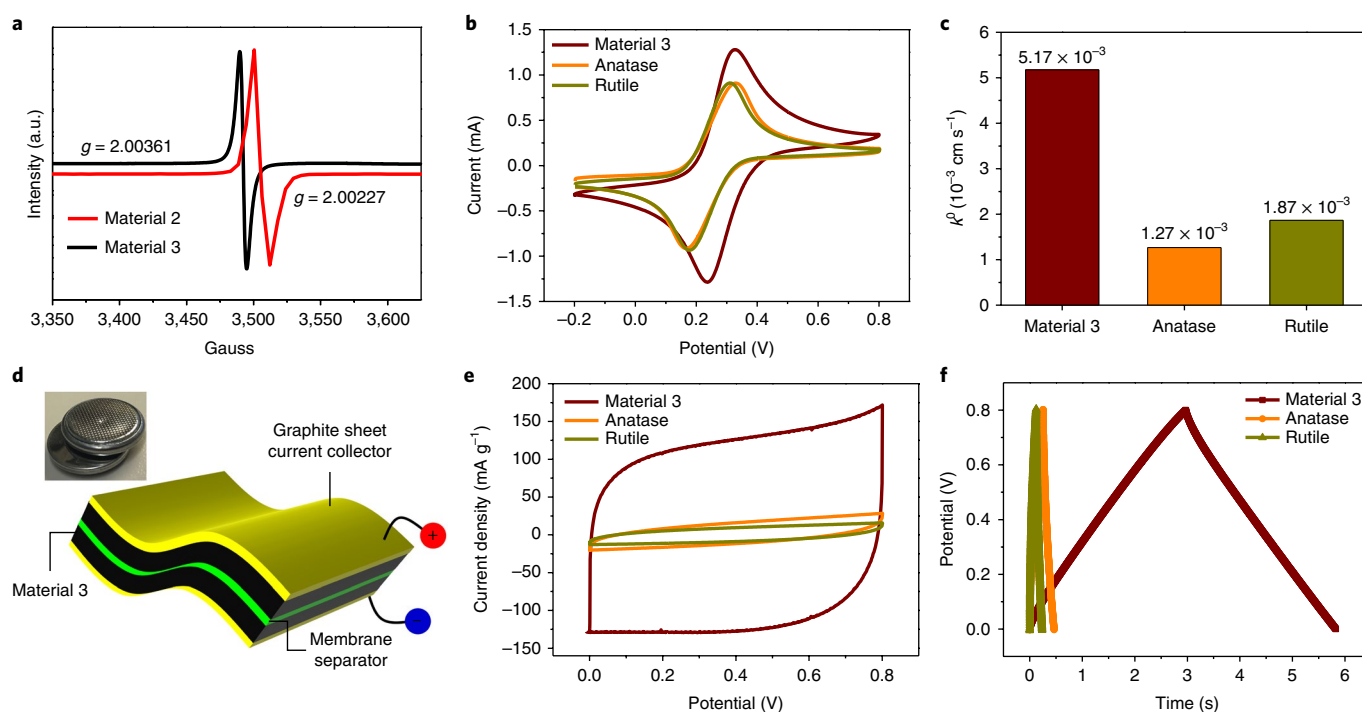


Fig. 5 | Data for the electrochemical properties of material 3. **a**, EPR spectroscopy at room temperature of materials 2 and 3. Each material produces a peak with g values of 2.00227 and 2.00361, respectively, very close to that found for single molecular boron cluster radicals. The origin of the paramagnetism is related to material 2 and the paramagnetism is perturbed when TiO_2 is introduced to material 2. **b**, CV curves for the ferri/ferrocyanide redox couple that compare the heterogeneous electron-transfer rate of material 3 with those of anatase and rutile TiO_2 . Material 3 produces the smallest peak-to-peak separation in the CV curves, which indicates an enhancement in electrochemical performance with respect to TiO_2 . **c**, Bar chart that shows the electron-transfer-rate constants for material 3, anatase and rutile TiO_2 . The electron transfer rate for material 3 is three to four times faster than that for pure phases of TiO_2 . **d**, A schematic illustration of a pouch-cell supercapacitor. **e**, CV curves obtained at a scan rate of $1,000 \text{ mV s}^{-1}$ for the pouch-cell supercapacitors consisting of material 3, anatase and rutile TiO_2 . The integrated area is dramatically increased in material 3. **f**, Galvanostatic charge/discharge curves of material 3, anatase and rutile TiO_2 supercapacitors at a current density of 0.04 mA cm^{-2} . The charge/discharge curves of material 3 exhibit an ideal triangular and symmetric shape, which indicates a good energy-storage capability.

Supplementary Table 4). The obtained data confirm the presence of Ti(IV) with no observable Ti sites in lower oxidation states.

Form of boron in material 3

Although the data obtained thus far support the model depicted in Fig. 1c, identification of the presence of intact clusters in material 3 remained indirect. Furthermore, although we could also conclude that no borides or carbides were present in material 3 on the surface, they are well known to form from boron-cluster materials in the bulk, albeit at high temperatures and under a reducing inert environment^{31,32}. We therefore turned to solid-state NMR (SSNMR) spectroscopy to further probe the bulk structural features of material 3 (Fig. 4a,b and Supplementary Figs. 19–22). The presence of intact B_{12} -based clusters in material 3 is demonstrated directly by 1D and 2D solid-state ^{11}B magic-angle-spinning (MAS) NMR measurements, which are sensitive to the local environments of ^{11}B atoms in the material. The 1D single-pulse ^{11}B MAS NMR spectrum of material 3 (Fig. 4a, top) shows a relatively broad (13 ppm full-width at half-maximum (FWHM)) signal at -16 ppm, which is assigned to intact B_{12} -based clusters, based on comparison with a reference material that contained intact B_{12} -based clusters, $\text{Cs}_2[\text{B}_{12}(\text{OH})_{12}]$ (Supplementary Fig. 19). Two additional ^{11}B signals were detected at 2 and 17 ppm, the latter of which is assigned on the basis of its ^{11}B shift position to boron oxides or borates in the material³³. The relatively narrow signal at 2 ppm (~ 3 ppm FWHM) is assigned to intact or partially intact B_{12} -based clusters at particle surfaces, similar to those described in the literature for ^{11}B MAS NMR measurements of B-doped TiO_2 (ref. 33). The presence of hydroxylated moieties, such

as surface-bound hydroxyls or residual water, is demonstrated by the 1D $^{11}\text{B}\{^1\text{H}\}$ cross-polarization (CP) MAS spectrum of material 3 (Fig. 4a, bottom), which shows that the ^{11}B signals at 17 and 2 ppm are enhanced by ^1H - ^{11}B cross-polarization transfer. The relative intensity of the signal at -16 ppm is greatly reduced in the $^{11}\text{B}\{^1\text{H}\}$ CP MAS spectrum compared with the single-pulse ^{11}B spectrum, which indicates that the majority of the molecular B_{12} -based clusters in material 3 are not hydroxylated.

Distinct surface moieties in the B_{12} -based clusters in material 3 are connected via covalent bonds, as determined by the solid-state 2D $^{11}\text{B}\{^{11}\text{B}\}$ J -mediated (through-covalent-bond) MAS NMR spectrum (Fig. 4b). The spectrum is presented as a 2D contour plot having single-quantum (SQ) and double-quantum (DQ) ^{11}B shift axes with pairs of signals from J -coupled ^{11}B species that are correlated across the diagonal at SQ shift positions Ω_1 and Ω_2 and at the same DQ shift ($\Omega_1 + \Omega_2$). Such 2D J -mediated measurements are sensitive principally to J couplings (~ 20 Hz) between directly bonded ^{11}B - ^{11}B spin pairs; J couplings between next-nearest-neighbour ^{11}B species (for example, ^{11}B -O- ^{11}B) are an order of magnitude weaker (~ 2 Hz) (ref. 34). The 2D J -mediated $^{11}\text{B}\{^{11}\text{B}\}$ NMR spectrum in Fig. 4b of material 3 shows two pairs of correlated signal intensity at the (SQ, DQ) shift coordinates of (5 ppm, 9 ppm) and (3 ppm, 9 ppm) and at (2 ppm, 3 ppm) and (1 ppm, 3 ppm) (red lines) from ^{11}B species that are covalently linked. These 2D NMR results establish unambiguously that underlying the ^{11}B signal at 2 ppm in Fig. 4b are at least four very narrow (~ 0.5 ppm FWHM) ^{11}B signals that arise from distinct covalently connected ^{11}B moieties in locally ordered environments at the particle surfaces. No J -correlated signals are

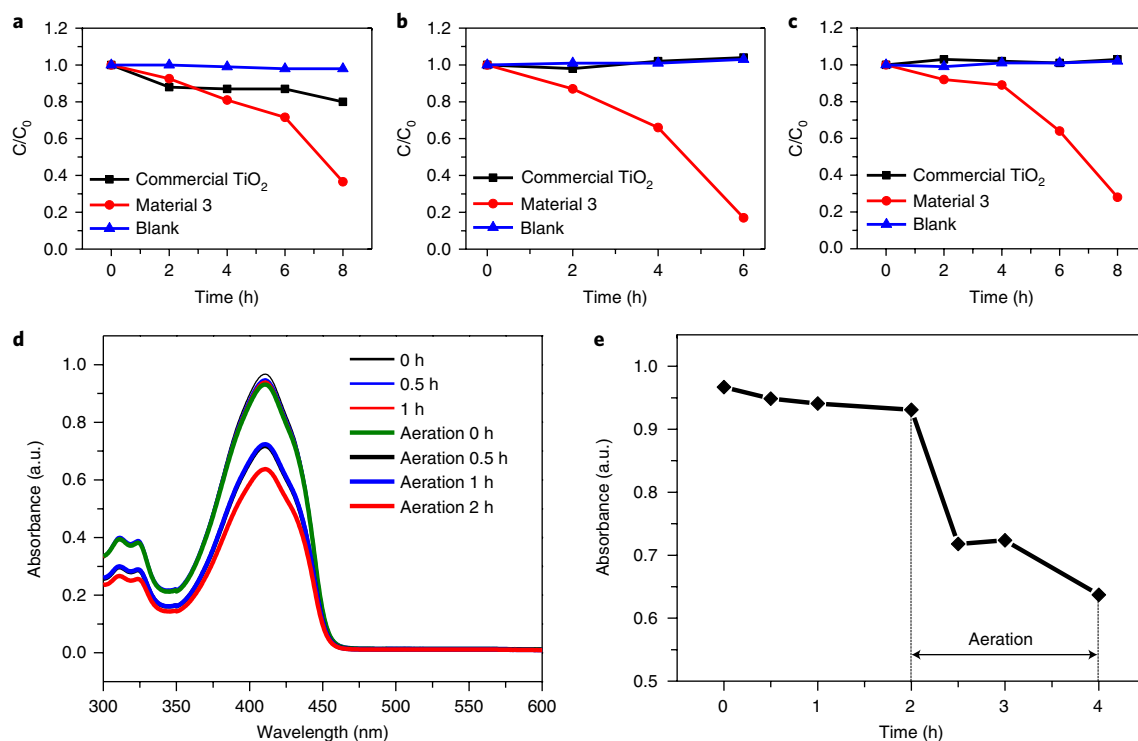


Fig. 6 | Photochemical data for material 3. **a–c**, Photocatalytic degradation of three dyes, alizarin red S (ARS) (**a**), methylene blue (MB) (**b**) and rhodamine B (RhB) (**c**), under red (~ 630 nm) LED light conditions. In each case, material 3 was found to catalyse the photodegradation of the dye at substantially faster rates than commercial TiO₂. **d**, UV-vis spectrum that depicts the progression of the consumption of 1,3-diphenylisobenzofuran (DPBF) in the presence of material 3 and irradiation with red (~ 630 nm) LED lights. DPBF is a sensitive fluorescent probe for ROS, and a decrease in its absorbance at 410 nm is indicative of the production of ROS. Aeration of the reaction mixture leads to increased rates of consumption of DPBF, consistent with ROS production. **e**, The chart shows the rate of consumption of DPBF.

observed for the peaks at 17 and -16 ppm, consistent with the weak $^{11}\text{B}-\text{O}-^{11}\text{B}$ J couplings associated with the boron oxide moieties and the influence of paramagnetic relaxation. The nanoscale proximities of these species can, nevertheless, be determined from analogous dipolar-mediated spectra that exploit much stronger dipolar interactions between nearby ^{11}B atoms. In addition to the same 2D intensity correlations, a complementary 2D dipolar-mediated (through space, <1 nm) $^{11}\text{B}\{^{11}\text{B}\}$ MAS NMR spectrum (Supplementary Fig. 22) shows an additional correlated ^{11}B signal at (-27 ppm, 14 ppm). This intensity correlation is associated with the B_{12} -based clusters and the boron oxide species, and thus establishes their nanoscale proximities in material 3.

Finally, to further our understanding of the clusters in materials 2 and 3, we conducted a pair distribution function (PDF) analysis of the high-energy X-ray scattering data obtained for the cluster-based materials (Fig. 4c,d), which is a powerful method that provides atomic-scale local structural information within a material as peaks within the PDF correspond directly to bond distances and atom–atom distances. Crucially, information about a material may be extracted directly from the PDF independently of a structural model, which allows the identification of local bonding and coordination environments even in amorphous materials³⁵. Features that correspond to B–O bond distances (~ 1.40 Å) can clearly be observed for material 2 (Supplementary Fig. 23), whereas features that correspond to cluster-based B–B bond distances (~ 1.75 Å to ~ 1.87 Å) are significantly reduced in intensity when compared with the molecular cluster control samples, probably because the cross-linked clusters adopt a more random arrangement. For material 3, peaks that correspond to B–O, B–B and Ti–O distances can be found, with an additional peak observed at ~ 2.13 Å, which corresponds to the distance expected for a Ti–O–B linkage. Overall, the

measurements are consistent with the findings from the SSNMR data and confirm the presence of intact boron clusters in both materials 2 and 3.

The combined comprehensive structural characterization of material 3 validates the proposed model for material 3 as being a hybrid molecular boron oxide material that consists of a cross-linked network of intact boron cluster units and boron oxide, within which are embedded TiO₂ nanocrystals in the anatase phase (Supplementary Figs. 24–31 and 39).

Electrochemical properties of material 3

Previously, $[\text{B}_{12}(\text{OH})_{12}]^{2-}$ and several functionalized derivatives of it were shown to display pseudometallic redox-active behaviour³⁶. The potential presence of clusters in material 3 in different redox states prompted us to probe the electronic properties of material 3. First, we subjected material 3 to electroparamagnetic resonance (EPR) spectroscopy (Fig. 5a) and observed a spectrum that featured a characteristic singlet with g values very close to that found for single molecular boron cluster radicals^{26,37}. Superconducting quantum interference device (SQUID) magnetometry performed on material 3 (Supplementary Fig. 32) revealed a decrease in magnetic susceptibility with increasing temperature, which indicates material 3 was paramagnetic. EPR spectroscopy of material 2 also produced a singlet with a similar g value to that of material 3, which suggests that the origin of the paramagnetism is related to the cross-linked hybrid molecular boron oxide material 2.

The potential redox activity of material 3 prompted us to investigate it electrochemically (Supplementary Figs. 33–38 and 42–47). Use of the ferri/ferrocyanide redox couple can provide useful information about the electron-transfer capability of electrochemically active materials and their potential competence as an electrocatalyst

(Fig. 5b)³⁸. The electron-transfer-rate constant of material 3 is significantly faster than that observed for both forms of TiO₂ (Fig. 5c), material 2 and graphitic carbon (Supplementary Figs. 33–35). The results of these measurements on material 3 highlight the ability of the hybrid molecular boron oxide material to confer favourable electronic properties on metal oxides (Supplementary Figs. 40 and 41).

Given the electrochemically active nature and high electrical conductivity of material 3, we further assembled pouch-cell supercapacitors using material 3 as an active-layer component (Fig. 5d). The pouch-cell supercapacitor that consisted of material 3 exhibited outstanding performances in comparison with both forms of TiO₂ (Fig. 5e,f). The CV curve of material 3 displayed a quasirectangular shape, and the charge/discharge curves followed the ideal triangular and symmetric profiles. The calculated gravimetric capacitance of material 3 was found to be 112.2 mF g⁻¹ at the scan rate of 1,000 mV s⁻¹, which is significantly greater than both anatase (33.3 mF g⁻¹) and rutile TiO₂ (15.0 mF g⁻¹). These excellent performances compared with that of pristine TiO₂ can be attributed to the cross-linking in material 3, which renders this material more conductive³⁹. Moreover, nanosized TiO₂ (<10 nm) not only provides a larger electrode–electrolyte contact area, but also effectively decreases the ion-diffusion length, which leads to a reduced ionic diffusion resistance and charge-transfer resistance⁴⁰ (Supplementary Fig. 47). These results highlight the promising energy-storage capability of material 3.

Photocatalytic activities of material 3

Given the substantial interest in visible-light assisted photochemical processes that feature photosensitized TiO₂ materials^{4,5,12,13}, we hypothesized whether the remarkable light-absorption properties of material 3 (Fig. 1c) could be leveraged for photochemical processes mediated by visible light. We investigated the use of material 3 as a photocatalyst for the visible-light driven photocatalytic decomposition of a variety of water contaminants (Fig. 6a–c). Using simple, low-power red (630 nm) light-emitting diodes (LEDs) as the light source, the photodegradations of three common dye contaminants were observed to proceed at faster rates for material 3 than for pristine TiO₂ used as a control. The mechanistic study of the observed photodegradation suggests that material 3 can be photoexcited with visible light and engage in an efficient electron transfer with oxygen gas molecules to produce reactive oxygen species (ROS) capable of degrading organic contaminants (Fig. 6d,e, and Supplementary Fig. 48)⁴¹. Importantly, given that material 3 contains no precious-metal components (only Ti, B, C and O), this presents a potentially powerful and cost-effective approach for waste remediation.

Outlook

The successful modification of TiO₂ demonstrates the value of molecular cross-linking as a new and previously unattainable strategy for effecting changes in the properties of metal oxide materials, enabled by the inherent robustness of an inorganic molecular cluster^{42–45}. Our preliminary experiments suggest that one can expand the repertoire for this method towards hybrid materials that contain ZrO₂. Importantly, these hybrids feature similar cross-linked morphology to that observed in TiO₂ (Supplementary Figs. 49–58). This approach expands on the existing strategies that allow the incorporation of molecular fragments within inorganic materials^{46–49}. The exhaustive structural characterization of material 3 supports its description as a cross-linked hybrid molecular boron oxide material embedded with TiO₂ nanoparticles. The unique structure of the material engenders dramatically improved electro- and photochemical behaviours, evidenced by fast electron-transfer rates, low resistivity and the ability to photodegrade common dye contaminants under red light, and the molecular cross-linking of TiO₂ is, indeed, responsible for all the observed features. The simplicity and potential generality of the route, in which interfacing molecular clusters

with a metal oxide via a facile reaction that proceeds at room temperature and uses readily available precious-metal-free precursors, makes it potentially amenable to a wide range of other metals and associated applications.

Methods

Methods, including statements of data availability and any associated accession codes and references, are available at <https://doi.org/10.1038/s41563-018-0021-9>.

Received: 24 February 2017; Accepted: 9 January 2018;

Published online: 5 March 2018

References

- Jaffe, R. L. et al. *Energy Critical Elements: Securing Materials for Emerging Technologies* (Materials Research Society/American Physical Society, Washington DC, 2011).
- Reddy, M. V., Subba Rao, G. V. & Chowdari, B. V. R. Metal oxides and oxysalts as anode materials for Li ion batteries. *Chem. Rev.* **113**, 5364–5457 (2013).
- McFarland, E. W. & Metiu, H. Catalysis by doped oxides. *Chem. Rev.* **113**, 4391–4427 (2013).
- Chen, X. & Mao, S. S. Titanium dioxide nanomaterials: synthesis, properties, modifications, and applications. *Chem. Rev.* **107**, 2891–2959 (2007).
- Asahi, R., Morikawa, T., Irie, H. & Ohwaki, T. Nitrogen-doped titanium dioxide as visible-light-sensitive photocatalyst: designs, developments, and prospects. *Chem. Rev.* **114**, 9824–9852 (2014).
- Kapilashrami, M., Zhang, Y., Liu, Y.-S., Hagfeldt, A. & Guo, J. Probing the optical property and electronic structure of TiO₂ nanomaterials for renewable energy applications. *Chem. Rev.* **114**, 9662–9707 (2014).
- Schneider, J. et al. Understanding TiO₂ photocatalysis: mechanism and materials. *Chem. Rev.* **114**, 9919–9986 (2014).
- Fujishima, A. & Honda, K. Electrochemical photolysis of water at a semiconductor. *Nature* **238**, 37–38 (1972).
- Ma, Y. et al. Titanium dioxide-based nanomaterials for photocatalytic fuel generations. *Chem. Rev.* **114**, 9987–10043 (2014).
- Bai, Y., Mora-Seró, I., De Angelis, F., Bisquert, J. & Wang, P. Titanium dioxide nanomaterials for photovoltaic applications. *Chem. Rev.* **114**, 10095–10130 (2014).
- Khan, S. U. M., Al-Shahry, M. & Ingler, W. B. Jr Efficient photochemical water splitting by a chemically modified n-TiO₂. *Science* **297**, 2243–2245 (2002).
- Chen, X., Liu, L., Yu, P. Y. & Mao, S. S. Increasing solar absorption for photocatalysis with black hydrogenated titanium dioxide nanocrystals. *Science* **331**, 746–750 (2011).
- Chen, X., Liu, L. & Huang, F. Black titanium dioxide (TiO₂) nanomaterials. *Chem. Soc. Rev.* **44**, 1861–1885 (2015).
- Salzmann, I. & Heimel, G. Toward a comprehensive understanding of molecular doping organic semiconductors. *J. Electron Spectrosc. Relat. Phenom.* **204**, 208–222 (2015).
- Pitochelli, A. R. & Hawthorne, M. F. The isolation of the icosahedral B₁₂H₁₂²⁻ ion. *J. Am. Chem. Soc.* **82**, 3228–3229 (1960).
- Spokoyny, A. M. New ligand platforms featuring boron-rich clusters as organomimetic substituents. *Pure Appl. Chem.* **85**, 903–919 (2013).
- Sivaev, I. B., Bregadze, V. I. & Sjöberg, S. Chemistry of closo-dodecaborate anion [B₁₂H₁₂]²⁻: a review. *Collect. Czech. Chem. Commun.* **67**, 679–727 (2002).
- Hawthorne, M. F. & Pushechnikov, A. Polyhedral borane derivatives: unique and versatile structural motifs. *Pure Appl. Chem.* **84**, 2279–2288 (2012).
- Dash, B. P., Satapathy, R., Maguire, J. A. & Hosmane, N. S. Polyhedral boron clusters in materials science. *New J. Chem.* **35**, 1955–1972 (2011).
- Hansen, B. R. S., Paskevicius, M., Li, H.-W., Akiba, E. & Jensen, T. R. Metal boranes: progress and applications. *Coord. Chem. Rev.* **323**, 60–70 (2016).
- Cheng, F. & Jäkle, F. Boron-containing polymers as versatile building blocks for functional nanostructured materials. *Polym. Chem.* **2**, 2122–2132 (2011).
- Núñez, R., Romero, I., Teixidor, F. & Viñas, C. Icosahedral boron clusters: a perfect tool for the enhancement of polymer features. *Chem. Soc. Rev.* **45**, 5147–5173 (2016).
- Alexandrova, A. N., Boldyrev, A. I., Zhai, H.-J. & Wang, L.-S. All-boron aromatic clusters as potential new inorganic and building blocks in chemistry. *Coord. Chem. Rev.* **250**, 2811–2866 (2006).
- Muetterties, E. L. *Boron Hydride Chemistry* (Academic, New York, NY, 1975).
- Farha, O. K. et al. Synthesis of stable dodecaalkoxy derivatives of hypercloso-B₁₂H₁₂. *J. Am. Chem. Soc.* **127**, 18243–18251 (2005).
- Wixtrom, A. I. et al. Rapid synthesis of redox-active dodecaborane B₁₂(OR)₁₂ clusters under ambient conditions. *Inorg. Chem. Front.* **3**, 711–717 (2016).

27. Messina, M. S. et al. Visible-light induced olefin activation using 3D aromatic boron-rich cluster photooxidants. *J. Am. Chem. Soc.* **138**, 6952–6955 (2016).
28. Qian, E. A. et al. Atomically precise organomimetic cluster nanoparticles assembled via perfluoroaryl-thiol S_NAr chemistry. *Nat. Chem.* **9**, 333–340 (2017).
29. Pan, L. et al. Hierarchical nanostructured conducting polymer hydrogel with high electrochemical activity. *Proc. Natl Acad. Sci. USA* **109**, 9287–9292 (2012).
30. To, J. W. F. et al. Ultrahigh surface area three-dimensional porous graphitic carbon from conjugated polymeric molecular framework. *ACS Cent. Sci.* **1**, 68–76 (2015).
31. Mirabelli, M. G. L. & Sneddon, L. G. Synthesis of boron carbide via poly(vinylpentaborane) precursors. *J. Am. Chem. Soc.* **110**, 3305–3307 (1988).
32. Su, K. & Sneddon, L. G. A polymer precursor route to metal borides. *Chem. Mater.* **5**, 1659–1668 (1993).
33. Feng, N. et al. Boron environments in B-doped and (B,N)-codoped TiO_2 photocatalysts: a combined solid-state NMR and theoretical calculation study. *J. Phys. Chem. C* **115**, 2709–2719 (2011).
34. Barrow, N. S. et al. Towards homonuclear J -solid-state NMR correlation experiments for half-integer quadrupolar nuclei: experimental and simulated ^{11}B MAS spin-echo dephasing and calculated $^2J_{BB}$ coupling constants for lithium diborate. *Phys. Chem. Chem. Phys.* **13**, 5778–5789 (2011).
35. Billinge, S. J. L. & Kanatzidis, M. G. Beyond crystallography: the study of disorder, nanocrystallinity and crystallographically challenged materials with pair distribution functions. *Chem. Commun.* **0**, 749–760 (2004).
36. Lee, M. W., Farha, O. K., Hawthorne, M. F. & Hansch, C. H. Alkoxy derivatives of dodecaborate: discrete nanomolecular ions with tunable pseudometallic properties. *Angew. Chem. Int. Ed.* **46**, 3018–3022 (2007).
37. Van, N. et al. Oxidative perhydroxylation of $[closo-B_{12}H_{12}]^{2-}$ to the stable inorganic cluster redox system $[B_{12}(OH)_{12}]^{2-/-}$: experiment and theory. *Chem. Eur. J.* **16**, 11242–11245 (2010).
38. Li, Y. et al. An oxygen reduction electrocatalyst based on carbon nanotube-graphene complexes. *Nat. Nanotech.* **7**, 394–400 (2012).
39. Guo, Y.-G., Hu, Y.-S., Sigle, W. & Maier, J. Superior electrode performance of nanostructured mesoporous TiO_2 (anatase) through efficient hierarchical mixed conducting networks. *Adv. Mater.* **19**, 2087–2091 (2007).
40. Jiang, C., Hosono, E. & Zhou, H. Nanomaterials for lithium ion batteries. *Nano Today* **1**, 28–33 November, (2006).
41. Gomes, A., Fernandes, E. & Lima, J. L. F. C. Fluorescence probes used for detection of reactive oxygen species. *J. Biochem. Biophys. Methods* **65**, 45–80 (2005).
42. Yin, Q. et al. A fast soluble carbon-free molecular water oxidation catalyst based on abundant metals. *Science* **328**, 342–345 (2010).
43. Yan, H. et al. Hybrid metal-organic chalcogenide nanowires with electrically conductive inorganic core through diamondoid-directed assembly. *Nat. Mater.* **16**, 349–355 (2017).
44. Bag, S., Trikalitis, P. N., Chupas, P. J., Armatas, G. S. & Kanatzidis, M. G. Porous semiconducting gels and aerogels from chalcogenide clusters. *Science* **317**, 490–493 (2007).
45. Song, J. et al. A multiunit catalyst with synergistic stability and reactivity: a polyoxometalate-metal organic framework for aerobic decontamination. *J. Am. Chem. Soc.* **133**, 16839–16846 (2011).
46. Yaghi, O. M., Li, G. & Li, H. Selective binding and removal of guests in a microporous metal-organic framework. *Nature* **378**, 703–706 (1995).
47. Bachman, J. E., Smith, Z. P., Li, T., Xu, T. & Long, J. R. Enhanced ethylene separation and plasticization resistance in polymer membranes incorporating metal-organic framework nanocrystals. *Nat. Mater.* **15**, 845–849 (2016).
48. Wang, C., Xie, Z., deKrafft, K. E. & Lin, W. Doping metal-organic frameworks for water oxidation, carbon dioxide reduction and organic photocatalysis. *J. Am. Chem. Soc.* **133**, 13445–13454 (2011).
49. Goellner, J. F., Gates, B. C., Vayssilov, G. N. & Rösch, N. Structure and bonding of a site-isolated transition metal complex: rhodium dicarbonyl in highly dealuminated zeolite Y. *J. Am. Chem. Soc.* **122**, 8056–8066 (2000).

Acknowledgements

A.M.S. thanks the University of California, Los Angeles (UCLA), Department of Chemistry and Biochemistry for start-up funds, 3M for a Non-Tenured Faculty Award and the Alfred P. Sloan Foundation for a research fellowship in chemistry. The authors thank the MRI program of the National Science Foundation (NSF grant no. 1532232 and no.1625776) for sponsoring the acquisition of SSNMR equipment and SQUID, respectively, at UCLA. Z.J.B. was supported by a grant from the BASF Corporation, and the solid-state MAS NMR measurements at the University of California, Santa Barbara (UCSB), made use of the shared facilities of the UCSB MRSEC (NSF DMR 1720256), a member of the Materials Research Facilities Network (www.mrfn.org). E.C.W. and J.T.M. were supported by the National Science Foundation Energy Research Center for Innovative and Strategic Transformations of Alkane Resources (CISTAR) under the cooperative agreement no. EEC-1647722. J.I.Z. thanks the Student and Research Support Fund for financial support. The computational modelling benefited from access to the Extreme Science and Engineering Discovery Environment, which is supported by NSF Grant ACI-1053575. R.R.L. and M.D. were supported by the US Department of Energy (DOE), Office of Basic Energy Sciences, Division of Chemical Sciences, Biosciences and Geosciences under Contract DE-AC02-06CH11357. This research used resources of the APS, a US DOE Office of Basic Energy Sciences and Office of Science User Facility, operated for the DOE Office of Science by Argonne National Laboratory under contract no. DE-AC02-06CH11357. MRCAT operations, beamline 10-BM, are supported by the DOE and the MRCAT member institutions.

Author contributions

A.M.S. developed the concept of molecular cross-linking and supervised the project. D.J., L.M.A.S. and A.M.S. co-designed the experiments, D.J. and L.M.A.S. performed the synthetic experimental work and D.J. performed the majority of the structural characterization and data analysis. Z.J.B. and B.F.C. designed, conducted and interpreted the SSNMR experiments and data. M.F.E.-K., J.Y.H. and, N.M. performed the electrochemical studies and interpreted the data with R.B.K. D.J., L.M.A.S., E.T., Y.S. and K.M. performed the dye degradation experiments. A.I.W. performed the EPR measurements. J.G. performed the resistivity measurements and interpreted the data with X.D. I.B.M. performed the SQUID measurements. S.K. designed and performed the STEM measurements. E.C.W. performed the XANES and EXAFS measurements and analysed the data with J.T.M. P.S.-C. and B.R. performed the mechanistic photochemical work and analysed the data with J.I.Z. R.R.L. and M.D. performed the TGA-MS and TPD ammonia experiments. J.L.B. performed the Raman spectroscopic measurements. C.H.H. performed the computational modelling. M.G.-J. and J.R. performed the TEM measurements and created the 3D reconstruction. K.W.C. collected and interpreted the high-energy X-ray scattering data. D.J., L.M.A.S., A.M.S., Z.J.B. and B.F.C. co-wrote the manuscript. All the authors discussed the results and commented on the manuscript during its preparation.

Competing financial interests

The authors declare no competing financial interests.

Additional information

Supplementary information is available for this paper at <https://doi.org/10.1038/s41563-018-0021-9>.

Reprints and permissions information is available at www.nature.com/reprints.

Correspondence and requests for materials should be addressed to A.M.S.

Publisher's note: Springer Nature remains neutral with regard to jurisdictional claims in published maps and institutional affiliations.

Methods

General synthetic methods. Dry-box manipulations were carried out under an atmosphere of dinitrogen in a Vacuum Atmospheres NexGen dry-box. THF was dried prior to use by sparging with argon, and then loaded on a solvent purification system (JC Meyer Solvent Systems). THF was then collected and stored over activated 4 Å molecular sieves in a dry box under a dinitrogen atmosphere.

¹H solution NMR spectra were recorded in THF-*d*₈, which was dried and stored over activated 4 Å molecular sieves. NMR samples were prepared under dinitrogen in 5 mm Norell S-5-400-JY-7 tubes fitted with J. Young Teflon valves. ¹H solution NMR spectra were recorded on AV300 spectrometers in ambient conditions and referenced internally to residual protio-solvent and are reported relative to tetramethylsilane ($\delta=0$ ppm). Chemical shifts are quoted in δ (ppm). Combustion analyses of materials 2 and 3 were carried out by the Microanalytical Facility at the College of Chemistry, University of California, Berkeley. The annealing of samples was carried out in an Across International CF1100 muffle furnace.

The following chemicals and materials were sourced from commercial vendors: Ti(OⁿPr)₄ (ACROS Organics), TiO₂ (J. T. Baker), pure anatase (Sigma Aldrich), pure rutile (Sigma Aldrich), Ti₂O₃ (Sigma Aldrich), TiO (Sigma Aldrich), Ti foil (Sigma Aldrich), TiB₂ (Materion), TiC (Strem Chemicals), graphite (Carbon Graphite Materials), crystalline boron (Advanced Materials), amorphous boron (Fisher Scientific), B₂O₃ (J. T. Baker), methylene blue (MB) (ACROS Organics), alizarin red S (ARS) (ACROS Organics), rhodamine B (RhB) (ACROS Organics), Zr(OⁿPr)₄/PrOH (Strem Chemicals) and ZrO₂ (SPEX Industries).

Caesium and (NⁿBu)₄⁺ salts of [B₁₂(OH)₁₂]²⁻ were synthesized by previously reported methods²⁶.

Material 2. [NⁿBu]₄[B₁₂(OH)₁₂] was added to a 20 ml glass scintillation vial and transferred to a muffle furnace. The sample was annealed by heating from room temperature to 500 °C at a rate of 1 °C min⁻¹ and holding at 500 °C for 6 h. After that, the furnace was cooled to room temperature at a rate of 1 °C min⁻¹ and 2 was recovered as a black powder.

Material 3. The synthesis was carried out in an inert atmosphere dry box. In a 20 ml glass scintillation vial, a clear solution of Ti(OⁿPr)₄ (833 mg, 0.87 ml, 2.93 mmol) in THF (1 ml) was added to a stirring suspension of [NⁿBu]₄[B₁₂(OH)₁₂] (200 mg, 0.244 mmol). The reaction mixture became orange on the addition, and was stirred for 6 h at room temperature. The clear red-orange reaction mixture was then brought outside of the dry box, whereupon water (0.8 ml) was carefully added to form an orange gel. The gel was then heat treated at 120 °C for 2 h to remove volatiles and produce a glassy red-orange solid. The sample was annealed in the same way as material 2, and material 3 was recovered as a black powder.

Material 4. The synthesis was carried out in a similar fashion as for material 3. A zirconium tetraisopropoxide isopropanol complex (568 mg, 1.46 mmol) in THF (1 ml) was added to a stirring suspension of [NⁿBu]₄[B₁₂(OH)₁₂] (100 mg, 0.122 mmol). On adding 0.8 ml of water to the reaction mixture, a pink gel was formed. After annealing it at 500 °C in air, material 4 was recovered as a light-brown powder.

Characterization methods and instrumentation. Diffuse reflectance UV-vis spectra were collected using a Cary 5000 UV-vis spectrometer. PXRD was undertaken on a Panalytical X'Pert Pro X-ray powder diffractometer with Cu-K α radiation. Diffraction spectra were collected from a 2θ angle of 10–80° with a step size of 0.04° at a rate of 1° min⁻¹. HRTEM was performed using a FEI Titan S/TEM operated at 300 kV. The samples were prepared by dropping an ethanol dispersion onto copper TEM grids (200 mesh, Formvar/carbon (Ted Pella)) using 1 ml syringes and dried in air. For 3D tomography, samples were crushed into a fine powder by ball milling before being dispersed in 70% ethanol/distilled H₂O at a concentration of 1 mg ml⁻¹. This suspension (2 μ l) was dispersed onto a TEM grid coated with an ultrathin carbon film (Ted Pella) and allowed to air dry. Tomographic data acquisition was performed on a Titan S/TEM (FEI) operated in the TEM mode at 300 keV. Images were acquired on an Ultrascan 2 \times 2 K digital camera (Gatan) at regular 2° tilts between -28 and 30°. Tomographic reconstruction was performed in MATLAB (MathWorks) using the GENFIRE reconstruction algorithm^{30,31}. Briefly images had their contrast inverted and a flat background was subtracted to remove the influence of the substrate. Images were then manually cropped and aligned to their centre of mass before being binned 3 \times 3. Reconstructions were performed for 50 iterations with 5 rounds of orientation refinement.

A Bruker EMX EPR spectrometer was used to acquire EPR spectra, with all the spectra collected on solid powder samples at 298 K. XPS was performed using an AXIS Ultra DLD instrument (Kratos Analytical). All XPS spectra were measured using a monochromatic Al K α X-ray source (10 mA for both survey and high-resolution scans, 15 kV) with a 300 \times 700 nm oval spot size. The pressure of the analyser chamber was maintained below 5 \times 10⁻⁸ Torr during the measurement. Spectra were collected with 160 eV pass energy for the survey spectra and 20 eV for high-resolution spectra of C 1s, O 1s, B 1s and Ti 2p using a 200 ms dwell time. All XPS peaks were charge referenced to the adventitious carbon 1 s signal at

284.6 eV. SEM images were obtained with a field-emission SEM (JEOL JSM 6700F). SQUID magnetometric data were measured by a magnetic property measurement system (MPMS V XL, Quantum Design Company). TGA was carried out on a Pyris Diamond TG/DTA (PerkinElmer instruments) at a heating rate of 5 °C min⁻¹ from room temperature to 1,000 °C under argon flow. Raman spectra were collected by a triple monochromator and detected with a charge-coupled device. Pellets of Cs₂[B₁₂(OH)₁₂], material 3 and TiO₂ were excited by an argon ion laser at a wavelength of 457.9 nm and a laser power of 100 mW. N₂ adsorption isotherms were obtained at 77 K on a TriStar volumetric adsorption analyser (Micromeritics). Ammonia temperature-programmed desorption (TPD) experiments were performed using an Altamira Instruments System (AMI-200) equipped with a thermal-conductivity detector (TCD). Each sample (100 mg) was loaded into a quartz U-tube and the catalyst bed was held in place by quartz wool at both ends. The samples were flushed with helium (30 cm³ min⁻¹) for 10 min at 25 °C. While still flushing with helium, the temperature was increased to 200 °C, held for 60 min, then decreased to 100 °C and held for 15 min. The samples were saturated by flowing 1% NH₃ in argon (30 cm³ min⁻¹) for 60 min at 100 °C and subsequently flushed with helium (30 cm³ min⁻¹) for 70 min. The bed temperature was increased to 650 °C at a ramp rate of 10 °C min⁻¹ under flowing helium and held for 60 min. During this time, the reactor effluent was monitored by the TCD detector. After each TPD experiment, the detector was calibrated by repeated pulsing of 1% NH₃ in argon through a blank sample loop.

Computational modelling. A representative pseudoamorphous model was constructed by first manually building anatase-TiO₂ particulates and then passivating with both protons and B₁₂O₁₂H_{10/11} species to achieve an overall oxidation state of Ti(IV). The model was then initially relaxed using geometrically constrained density functional theory (PBEsol, 500 eV cutoff, PAW pseudopotentials in VASP), with the B–O–Ti distance allowed to relax. The resultant structure was then subjected to a heat-and-quench process at a rate of 0.1 K per 5 fs to 300 K in a canonical ensemble, which yielded one possible orientation of the otherwise amorphous material. Electron-energy alignments were computed using HSE06 and a triple zeta basis set, as implemented in Gaussian09. Each cluster was geometrically optimized in its respective oxidation state and the electron energies were aligned to the vacuum from Janak's theorem.

X-ray absorption spectroscopy. Data collection. X-ray absorption measurements were acquired at the Ti K edge (4.9660 keV) on the bending magnet beam line of the Materials Research Collaborative Access Team (MRCAT) at the Advanced Photon Source (APS), Argonne National Laboratory. The X-ray ring at APS has a current of 102 mA and the beamline has a flux of 5 \times 10¹⁹ photons s⁻¹. Photon energies were selected using a water-cooled, double-crystal Si(111) monochromator, which was detuned by approximately 50% to reduce harmonic reflections. The X-ray beam was 0.5 \times 2.5 mm² and measurements were made in step-scan transmission mode. Data points were acquired in three separate regions: a pre-edge region (-250 to -50 eV; step size, 10 eV; dwell time, 0.25 s), the XANES region (-50 to -30 eV; step size, 5 eV; dwell time, 0.25 s; and -30 to +30 eV; step size, 0.4 eV; dwell time, 0.5 s) and the extended X-ray absorption fine structure (EXAFS) region (0–15 Å⁻¹, step size, 0.05 Å⁻¹; dwell time, 0.5 s). The ionization chambers were optimized for the maximum current with a linear response (~10¹⁰ photons s⁻¹ were detected) with 10% absorption in the incident ion chamber and 70% absorption in the transmission detector. A third detector in series simultaneously collected a Ti foil reference spectrum with each measurement for energy calibration.

Samples were pressed into a cylindrical sample holder that consisted of six wells to form a self-supporting wafer. To achieve an absorbance (μ x) of approximately 1.0, the samples were diluted with boron nitride. The sample holder was placed in a quartz reactor tube (1 inch (2.54 cm) outer diameter, 10 inch (25.4 cm) length) sealed with Kapton windows by two Ultra-Torr fittings through which gas could be flowed. The reactor was purged with He and measurements were taken at room temperature in He.

Analysis of XAS data. XAS spectra were analysed using WinXAS 3.2 software. The data were obtained from -250 eV below the edge to 850 eV above the edge and normalized with linear and cubic fits of the pre-edge and post-edge regions, respectively. The oxidation state of each sample was determined by the XANES edge energy and compared with Ti foil, TiO, Ti₂O₃ and TiO₂ reference compounds.

The EXAFS was extracted by performing a cubic spline fit of the normalized absorption spectrum with 5 nodes from 2.0 to 13 Å⁻¹. EXAFS coordination parameters were obtained through a least-squares fit in *R* space of the *k*²-weighted Fourier transform from 2.8 to 11.4 Å⁻¹. The experimental phase shift and backscattering amplitude fitting functions for Ti–O scattering pairs were determined from TiO₂.

Solid-state ¹¹B MAS NMR. The solid-state ¹¹B MAS NMR measurements at a high magnetic field strength were performed on a Bruker AVANCE-III Ultrashield Plus 800 MHz (18.8 T) narrow-bore spectrometer operating at Larmor frequencies of 256.75 and 800.24 MHz for ¹¹B and ¹H, respectively, and a Bruker 3.2 mm broadband Tri-Gamma H-X-Y probehead was used. The ¹¹B background signal

from the MAS probehead was subtracted from the single-pulse ^{11}B MAS NMR spectra. Spinal-64 (ref. ⁵³) ^1H decoupling was applied during the acquisition period. The ^{11}B shifts were referenced to $\text{BF}_3\text{O}(\text{C}_2\text{H}_5)_2$ in CDCl_3 at 0 ppm, with solid BN as a secondary ^{11}B shift reference and as an external ^{11}B spin counting reference. The ^{11}B spin-lattice (T_1) relaxation times were measured by using a saturation recovery pulse sequence with a rotor-asynchronous saturating pulse train⁵³ and Hahn-echo acquisition. The resulting ^{11}B saturation recovery signal intensities were fit to a stretched exponential fitting function with a stretched exponent of 0.5, which describes the shape of the distribution of ^{11}B T_1 relaxation times⁵⁴. The $^{11}\text{B}\{^1\text{H}\}$ CP-MAS spectra were acquired using a very short ^{11}B - ^1H contact time of 100 μs to probe hydrated ^{11}B environments. The 2D J -mediated NMR spectrum of material 3 was acquired at 18.8 T, 10 kHz MAS and 298 K using a refocused INADEQUATE sequence with an experimentally optimized half-echo τ delay of 0.4 ms.

The low-temperature ^{11}B MAS NMR spectra of material 3 were acquired at 9.4 T, 8 kHz MAS and 95 K using a Bruker H-X-Y 3.2 mm low-temperature MAS probehead and at Larmor frequencies of 128.40 and 400.20 MHz for ^{11}B and ^1H , respectively. The low-temperature 2D dipolar mediated $^{11}\text{B}\{^{11}\text{B}\}$ spectrum of material 3 was acquired at 4.6 kHz MAS using a CP-mediated spin-refocused SR26, (ref. ¹¹) dipolar recoupling sequence⁵⁵ using an experimentally-optimized recoupling period of 1.74 ms (eight rotor periods) for the excitation and reconversion of the double-quantum coherences.

PDF analysis. Total scattering data suitable for PDF analysis were collected at beamline 11-ID-B at the APS at the Argonne National Laboratory using 58.6 keV (0.2115 Å) X-rays. Data were collected using an amorphous silicon area detector at approximately 18 cm from the sample. Calibrations of the sample-detector distance, detector tilt and reduction of data to 1D patterns were performed using FIT2D. PDFs were obtained from the data with PDFgetX2 to a Q_{max} of 24 \AA^{-1} . Structural models were refined against the data in PDFgui.

Electrochemical measurements. All electrochemical experiments were collected using a Biologic VMP3 electrochemical workstation (VMP3b-10, Science Instruments). For all the measurements, a three-electrode configuration was employed with a platinum foil counter electrode (Sigma-Aldrich) and Ag/AgCl, 3 M NaCl reference electrode (Bioanalytical Systems). The redox system used for the evaluation of the electron transfer kinetics was 5 mM $\text{K}_3[\text{Fe}(\text{CN})_6]/\text{K}_4[\text{Fe}(\text{CN})_6]$ (1:1 molar ratio) dissolved in 1.0 M KCl solution. The working electrodes were material 3, anatase TiO_2 (Sigma-Aldrich) and rutile TiO_2 (Sigma-Aldrich), material 2 and pyrolytic graphite, all with a working area of 1 cm^2 . The working electrodes were prepared by mixing 80 wt% active materials, 10 wt% carbon black and 10% (1:1 CMC/SBR) binder in water. The homogeneous solution was drop cast onto a graphite current collector. The heterogeneous electron-transfer-rate constant (k_{obs}^0) was calculated using a method developed by Nicholson, which relates the peak separation (ΔE_p) to a dimensionless kinetic parameter, ψ , and consequently to k_{obs}^0 according to the equation⁵⁶:

$$\psi = \frac{(D_{\text{O}}/D_{\text{R}})^{\alpha/2} k^0}{(\pi D_{\text{O}} \nu F / RT)^{1/2}}$$

where D_{O} and D_{R} are the diffusion coefficients of the oxidized and reduced species, respectively. The other variables are the transfer coefficient (α), heterogeneous electron-transfer-rate constant (k^0), scan rate (ν), Faraday constant (F), general gas constant (R) and temperature (T). The diffusion coefficients for the oxidized and reduced forms of the solution-phase probe redox couple are equal, and therefore $(D_{\text{O}}/D_{\text{R}})^{\alpha/2} \approx 1$. A diffusion coefficient of $[\text{Fe}(\text{CN})_6]^{3-/4-}$ is $7.26 \times 10^{-6} \text{ cm}^2 \text{ s}^{-1}$ in 1.0 M KCl electrolyte^{57,58}.

Assembly of supercapacitors. Both pouch cells and coin cells were assembled to test the capacitive performance of the different materials. A Celgard 3501 separator was utilized to complete the assembly of the cells. Supercapacitor electrodes were prepared following the procedure described in the previous section. A pouch cell was assembled by sandwiching a Celgard separator with two identical pieces of the coated films. This stack was then inserted into an aluminium-laminated bag followed by the addition of some electrolytes. To assemble the coin cells, the electrode films were punched into discs of 14 mm in diameter, whereas the Celgard 3501 membranes were punched into 17 mm to avoid the two electrodes shorting. A stack of electrode 1, separator and electrode 2 was placed into the bottom cap followed by the addition of 500 μl of the electrolyte (1.0 M Na_2SO_4). A stainless-steel spacer and a spring were placed on top of that to enable an electrical connection with the positive and negative terminals of the pouch cell. Eventually, the top cap was added and the full stack crimped using the CR 2032 coin-cell crimper (MTI Corp). All the cells were assembled in the air.

The gravimetric capacitance (C_g (mF g⁻¹)) of each device was calculated from CV curves using the formula:

$$C_g = \frac{1}{m(V_f - V_i)} \int_{V_i}^{V_f} i(V) dV$$

where i is the current response (mA), $V_f - V_i$ is the potential window (V), where V_f and V_i are the final and initial voltage, respectively, and m is the mass of the active materials on both electrodes.

Resistivity measurements. The resistivity measurements were carried out using a probe station (Lakeshore Model PS-100 Tabletop Cryogenic Probe Station) under vacuum conditions. The meter was Agilent B2902A Precision Source/Measure Unit. By sweeping the voltage applied on two ends of our material, we obtained the current and voltage (CV) curves of ten different devices. Then, the resistances were determined by calculating the ratio of the maximum voltage and the corresponding current. After normalizing the resistance with the geometries of our material, we achieved the resistivity and the statistics.

Visible-light photocatalytic degradation. The visible-light photocatalytic activity of material 3 was investigated by monitoring the decomposition of the organic dyes ARS, MB and RhB in an aqueous solution under a 630 nm red LED light. For the degradation of ARS, 0.050 g of material 3 was added to 15 ml of solution with a concentration of 20 mg l⁻¹ and the suspension was stirred in the dark overnight to reach an equilibrated adsorption of the suspension to the catalyst. In the case of RhB and MB, 0.010 g of material 3 was added to 15 ml of MB solution with concentrations of 10 and 20 ppm, respectively, and the suspensions were stirred in the dark for 1 h before illumination. At given irradiation time intervals (2 h), aliquots of 2.5 ml were taken out, centrifuged and subsequently filtered through a filter (EMD Millipore, pore size 0.22 μm) to remove any remaining material 3. The filtrates were then analysed by UV-vis spectra with a spectrometer (Shimadzu UV-3101PC). Maximum absorptions at 420, 554 and 660 nm were monitored for ARS, RhB and, MB degradation, respectively.

Detection of ROS. A solution was prepared in a beaker that contained 12.5 ppm 1,3-diphenylisobenzofuran (DPBF) (Sigma) in acetonitrile. After irradiating for 2 h under visible light (630 nm red LED) for stabilization, 10 mg of material 2 or 3 were added to 80 ml of DPBF solution. The system was opened to air and subsequently aerated to provide more oxygen. At given time intervals, aliquots were collected and their absorbance was recorded at 410 nm.

Data availability. All the data generated or analysed during this study are included within this article and its Supplementary Information files.

References

- Pryor, A. Jr. et al. GENFIRE: a generalized Fourier iterative reconstruction algorithm for high-resolution 3D imaging. *Sci. Rep.* **7**, 10409 (2017).
- Yang, Y. et al. Deciphering chemical order/disorder and material properties at the single-atom level. *Nature* **542**, 75–79 (2017).
- Fung, B. M., Khitrin, A. K. & Ermolav, K. An improved broadband decoupling sequence for liquid crystals and solids. *J. Magn. Reson.* **142**, 97–101 (2000).
- Yesinowski, J. P. Finding the true-spin-lattice relaxation time for half-integral nuclei with non-zero quadrupolar couplings. *J. Mag. Reson.* **252**, 135–144 (2015).
- Johnston, D. C. Stretched exponential relaxation arising from a continuous sum of exponential decays. *Phys. Rev. B.* **74**, 184430 (2006).
- Brouwer, D. H., Kristiansen, P. E., Fyfe, C. A. & Levitt, M. H. Symmetry-based ^{29}Si dipolar recoupling magic angle spinning NMR spectroscopy: a new method for investigating three-dimensional structures of zeolite frameworks. *J. Am. Chem. Soc.* **127**, 542–543 (2005).
- Nicholson, R. S. Theory and application of cyclic voltammetry for measurement of electrode reaction kinetics. *Anal. Chem.* **37**, 1351–1355 (1965).
- Moldenhauer, J., Meier, M. & Paul, D. W. Rapid and direct determination of diffusion coefficients using microelectrode arrays. *J. Electrochem. Soc.* **163**, H672–H678 (2016).
- Konopka, S. J. & McDuffie, B. Diffusion coefficients of ferri- and ferrocyanide ions in aqueous media, using twin-electrode thin-layer electrochemistry. *Anal. Chem.* **42**, 1741–1746 (1970).

In the format provided by the authors and unedited.

A molecular cross-linking approach for hybrid metal oxides

Dahee Jung^{1,2}, Liban A. M. Saleh¹, Zachariah J. Berkson³, Maher F. El-Kady^{1,2}, Jee Youn Hwang¹, Nahla Mohamed^{1,4}, Alex I. Wixtrom¹, Ekaterina Titarenko¹, Yanwu Shao¹, Cassandra McCarthy¹, Jian Guo⁵, Ignacio B. Martini¹, Stephan Kraemer⁶, Evan C. Wegener⁷, Philippe Saint-Cricq¹, Bastian Rühle¹, Ryan R. Langeslay⁸, Massimiliano Delferro ⁸, Jonathan L. Brosmer ¹, Christopher H. Hendon⁹, Marcus Gallagher-Jones ^{1,2}, Jose Rodriguez ^{1,2}, Karena W. Chapman ¹⁰, Jeffrey T. Miller⁷, Xiangfeng Duan^{1,2}, Richard B. Kaner^{1,2,5}, Jeffrey I. Zink^{1,2}, Bradley F. Chmelka³ and Alexander M. Spokoyny ^{1,2*}

¹Department of Chemistry and Biochemistry, University of California, Los Angeles, Los Angeles, CA, USA. ²California NanoSystems Institute (CNSI), University of California, Los Angeles, Los Angeles, CA, USA. ³Department of Chemical Engineering, University of California, Santa Barbara, Santa Barbara, CA, USA. ⁴Department of Chemistry, Faculty of Science, Cairo University, Giza, Egypt. ⁵Department of Materials Science and Engineering, University of California, Los Angeles, Los Angeles, CA, USA. ⁶Materials Research Center, University of California, Santa Barbara, Santa Barbara, CA, USA. ⁷Davidson School of Chemical Engineering, Purdue University, West Lafayette, IN, USA. ⁸Chemical Sciences and Engineering Division, Argonne National Laboratory, Argonne, IL, USA. ⁹Department of Chemistry and Biochemistry, University of Oregon, Eugene, OR, USA. ¹⁰X-ray Science Division, Advanced Photon Source, Argonne National Laboratory, Argonne, IL, USA. *e-mail: spokoyny@chem.ucla.edu

A Molecular Cross-linking Approach for Hybrid Metal Oxides

Dahee Jung, Liban M. A. Saleh, Zachariah J. Berkson, Maher F. El-Kady, Jee Youn Hwang, Nahla Mohamed, Alex I. Wixtrom, Ekaterina Titarenko, Yanwu Shao, Kassandra McCarthy, Jian Guo, Ignacio B. Martini, Stephan Kraemer, Evan C. Wegener, Philippe Saint-Cricq, Bastian Ruehle, Ryan R. Langeslay, Massimiliano Delferro, Jonathan L. Brosmer, Christopher H. Hendon, Marcus Gallagher-Jones, Jose Rodriguez, Karena W. Chapman, Jeffrey T. Miller, Xiangfeng Duan, Richard B. Kaner, Jeffrey I. Zink, Bradley F. Chmelka and Alexander M. Spokoyny*

SUPPLEMENTARY INFORMATION

Email: spokoyny@chem.ucla.edu

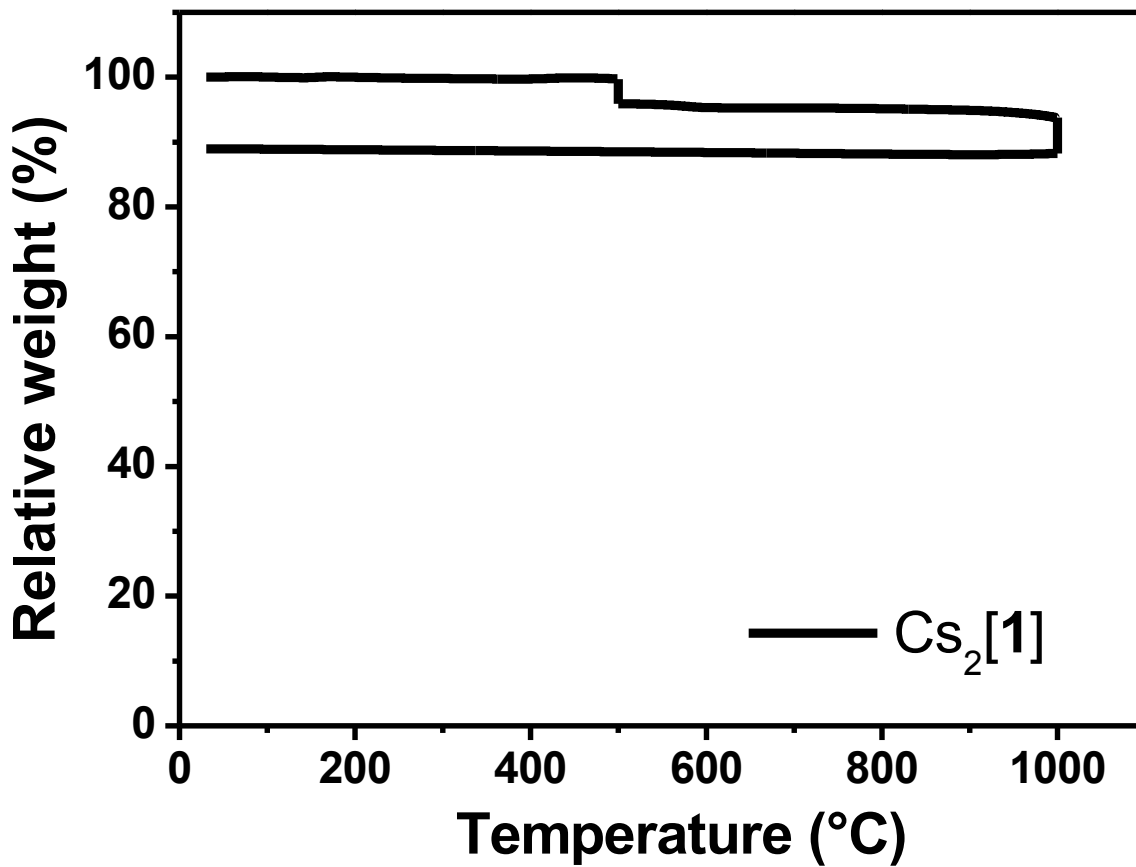


Fig. S1.
TGA analysis of $\text{Cs}_2[1]$.

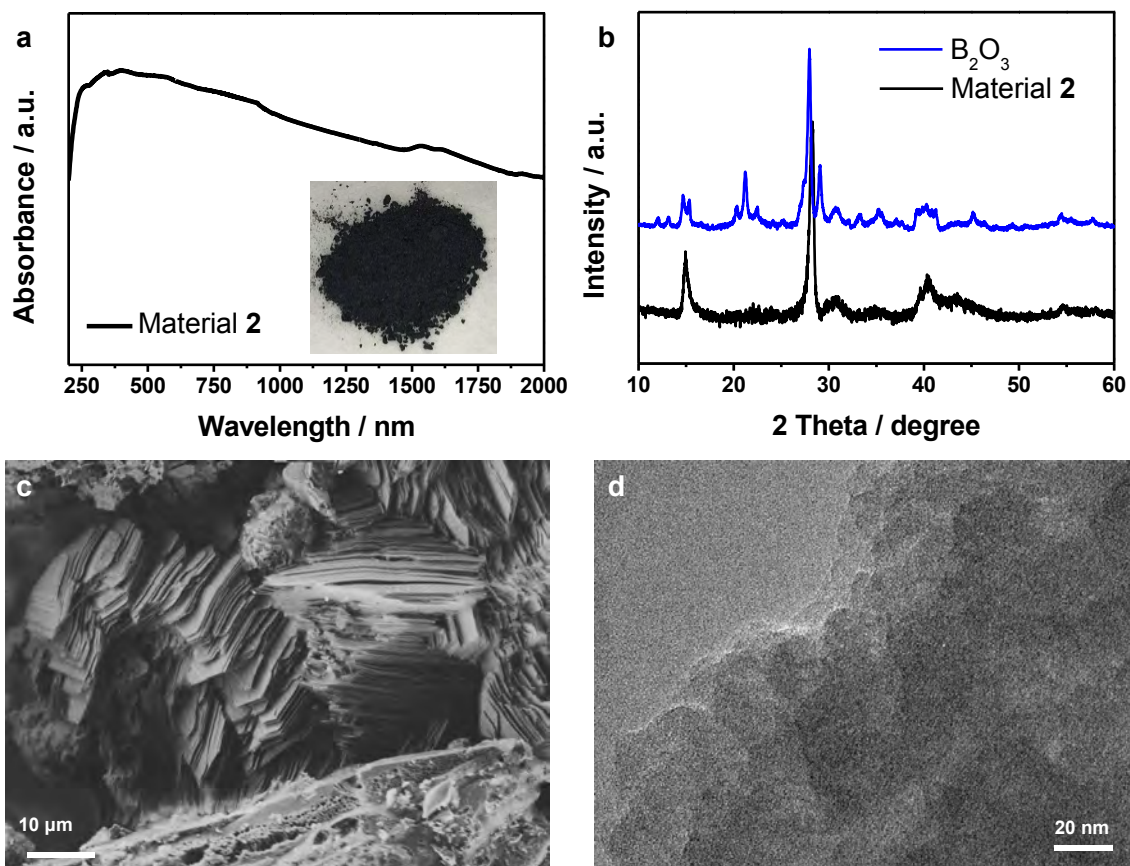


Fig. S2.

Characterization of material **2**. **(a)** Diffuse reflectance UV-Vis spectroscopy of **2**, showing absorption out to the near-IR range; **(b)** PXRD pattern of **2**, with B_2O_3 control; **(c)** SEM image of **2**; **(d)** TEM image of **2**, being consistent with the PXRD data in suggesting no long range order present.

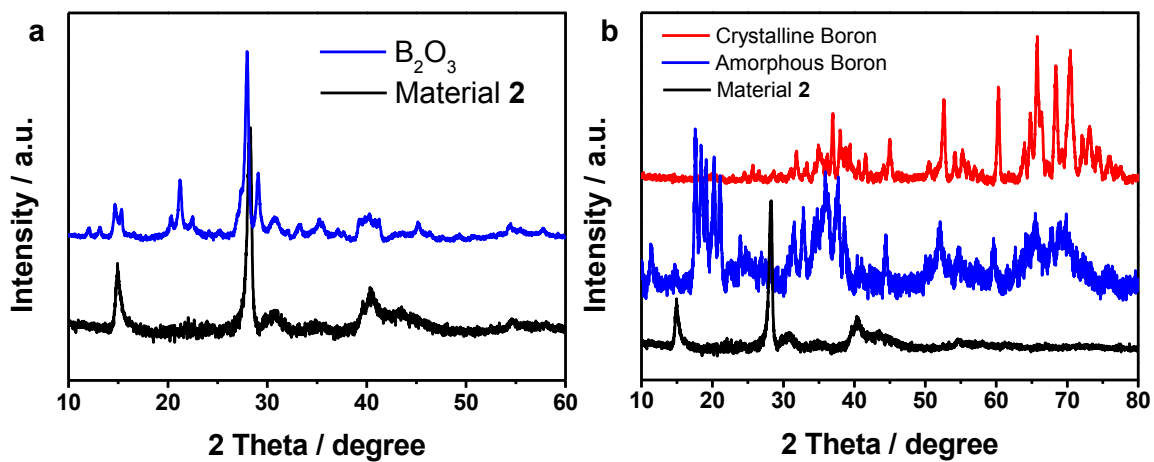


Fig. S3. PXRD of material **2** with B₂O₃, crystalline and amorphous elemental boron controls. (a) B₂O₃ and **2**; (b) crystalline and amorphous elemental boron and **2**.

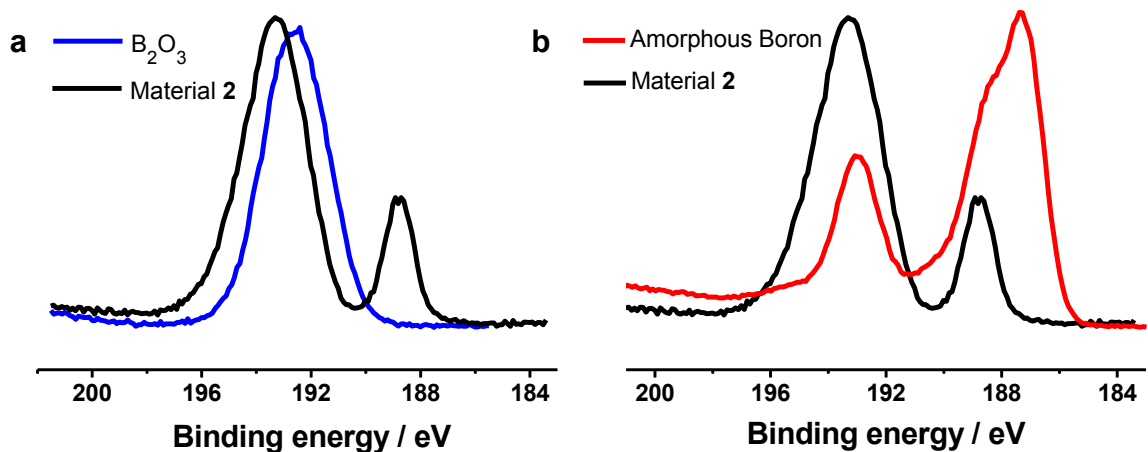


Fig. S4.

XPS of material **2** showing the boron 1s region, with B₂O₃ and amorphous elemental boron included as controls. **(a)** boron 1s region of B₂O₃ and material **2**. Two peaks are observed in the boron 1s region for **2** corresponding to intact clusters (188.8 eV) and a form of boron oxide at higher energy (193.3 eV), and excludes the presence of elemental boron.; **(b)** boron 1s region amorphous elemental boron and **2**.

% Found	C	H	N
Trial 1	3.99	4.97	0.73
Trial 2	4.06	5.08	0.73

Table S1.

Combustion analysis of material **2**. It confirms the presence of ~ 4 % carbon in the material, assigned as graphitic carbon based on the XPS binding energy. The appearance of graphitic carbon suggests a likely templating effect imposed by the clusters, reminiscent of the cross-linked “molecular frameworks” recently reported by Bao and co-workers^{1,2}, albeit with significantly lower carbon content in the case of **2**.

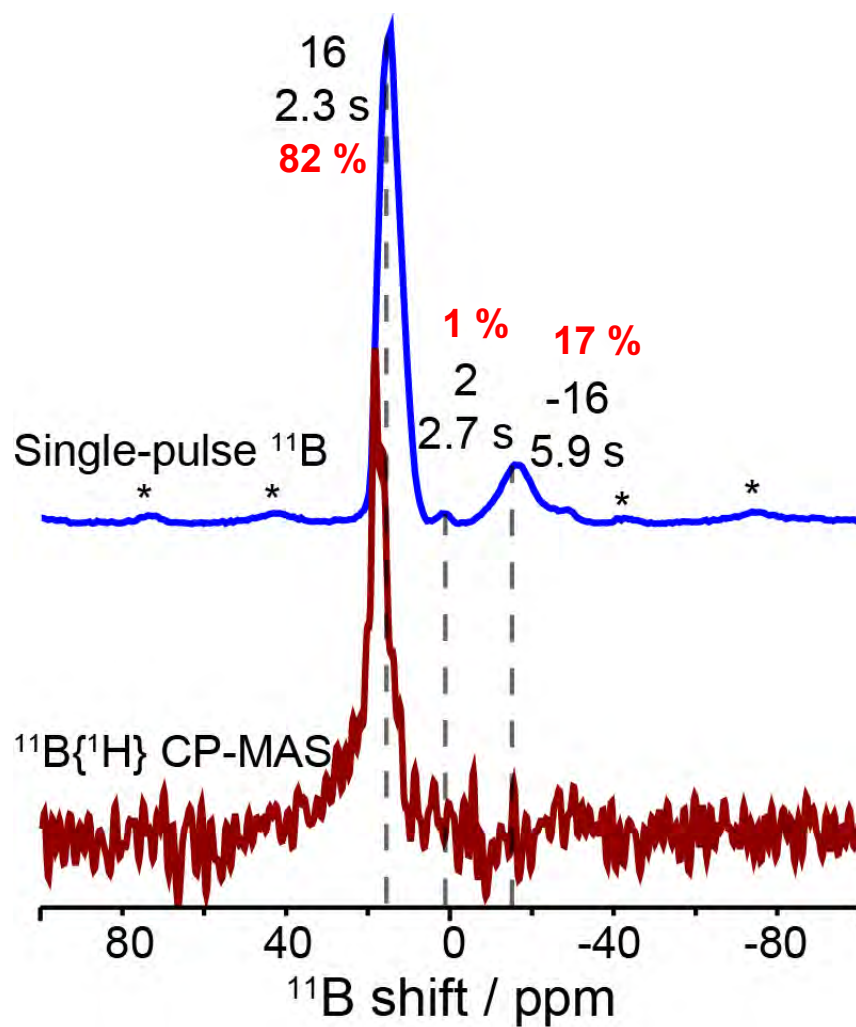


Fig. S5.

Solid-state 1D single-pulse ^{11}B MAS NMR (top) and $^{11}\text{B}\{^1\text{H}\}$ CP-MAS (bottom) spectra of material 2, acquired at 18.8 T and 298 K. A single ^{11}B signals at -16 and 2 ppm are detected from the molecular B_{12} -based clusters. ~80 % of the boron content is in the oxidized form.

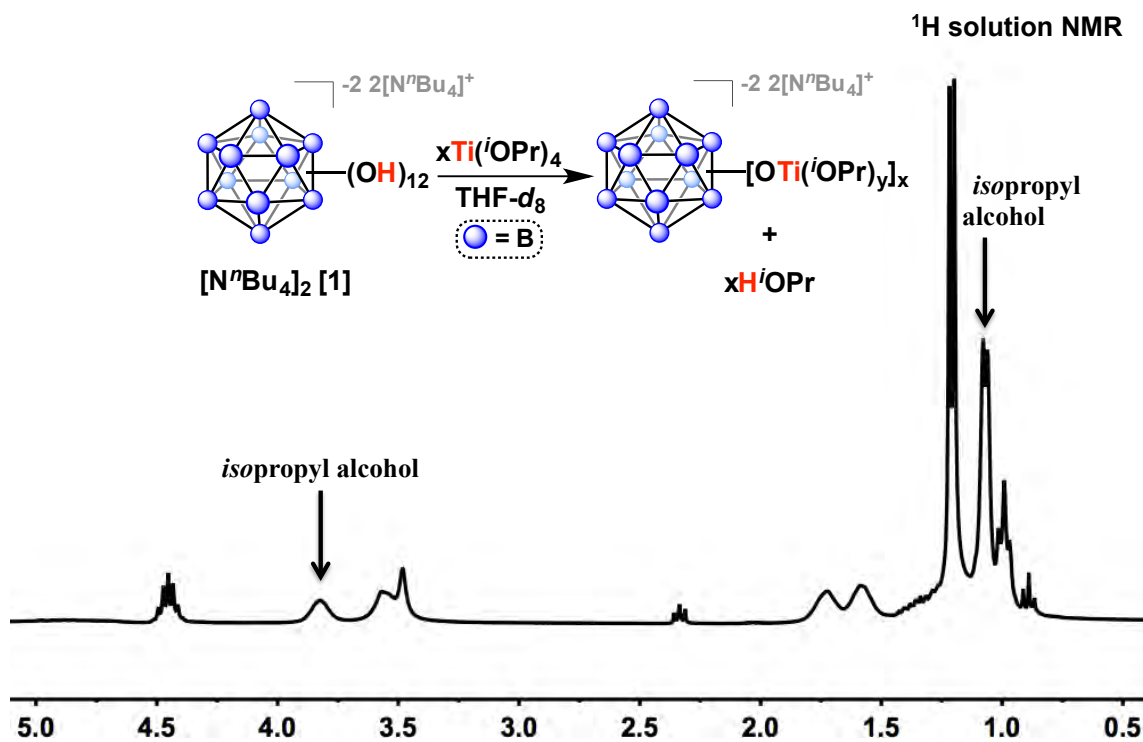


Fig. S6.

¹H solution NMR of the test reaction of Ti(OⁱPr)₄ with [N^uBu₄]₂[1] in THF-*d*₈. A solution of Ti(OⁱPr)₄ (31 mg, 0.03 mL, 0.11 mmol) in THF-*d*₈ (0.3 mL) was added to a suspension of [N^uBu₄]₂[1] (15 mg, 0.018 mmol) in THF-*d*₈ (0.3 mL). The resultant orange mixture was allowed to stir for 2 h at room temperature. The sample was then transferred to an NMR tube with a J. Young Teflon valve for the ¹H solution NMR experiment. Peaks associated with *isopropyl alcohol* (marked with arrows) can be observed, indicating formation of B–O–Ti bonds.

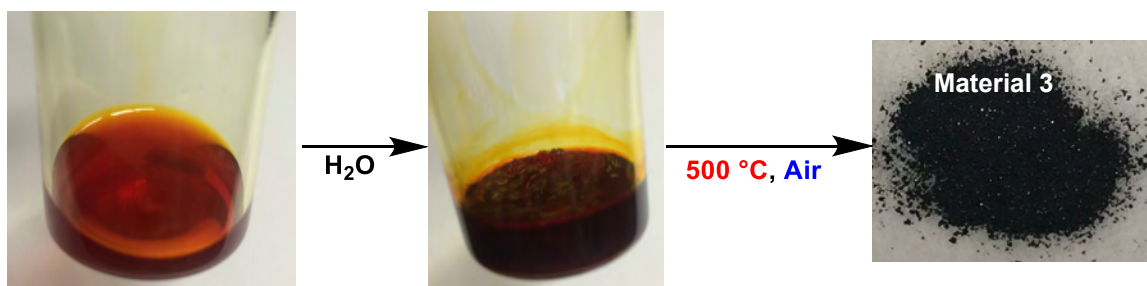


Fig. S7.

A reaction of $[\text{N}^n\text{Bu}_4]_2[\mathbf{1}]$ with $\text{Ti}(\text{O}^i\text{Pr})_4$ in THF. It produces a clear red-orange solution, which is subsequently hydrolyzed to form a red-orange gel. After calcining at $120\text{ }^\circ\text{C}$, the now dark orange solid is annealed at $500\text{ }^\circ\text{C}$ in air to produce material **3** as a shiny black solid.

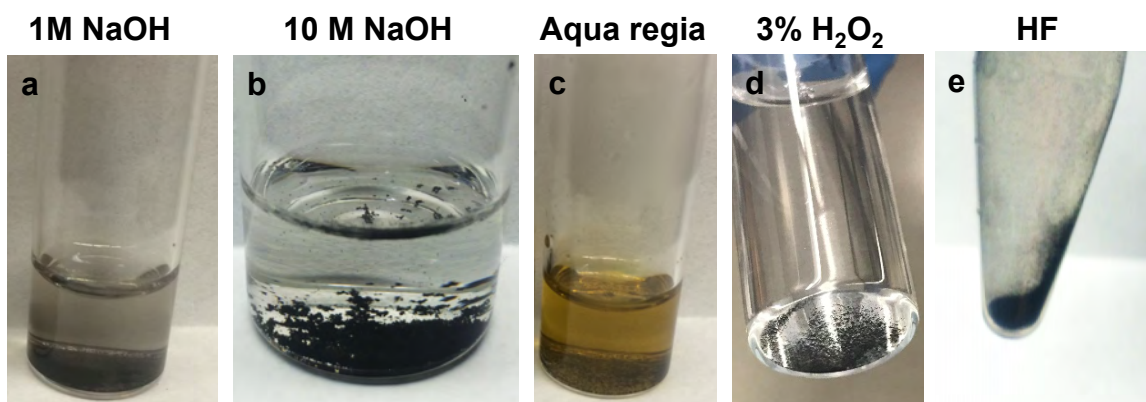


Fig. S8.

Chemical stability test of material **3** in (a) 1M NaOH; (b) 10 M NaOH; (c) Aqua regia; (d) 3 % H₂O₂; (e) HF. **3** resisted prolonged exposure to a variety of strong acids, bases, and 3 % H₂O₂ consistent with its hypothesized highly cross-linked composition.

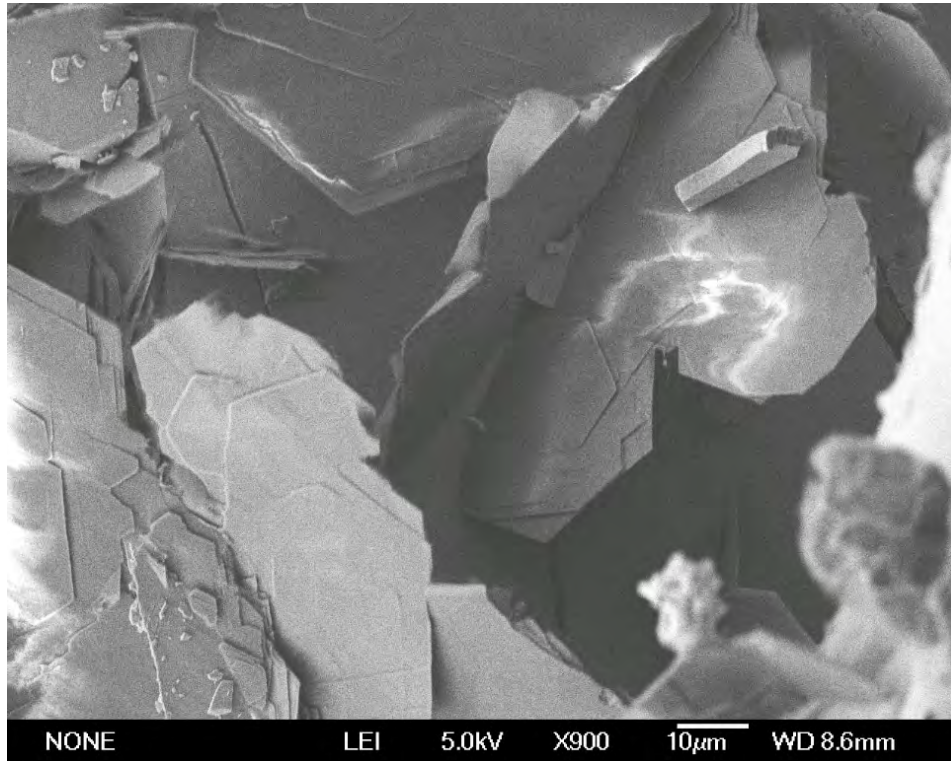


Fig. S9.
SEM image of material 3.

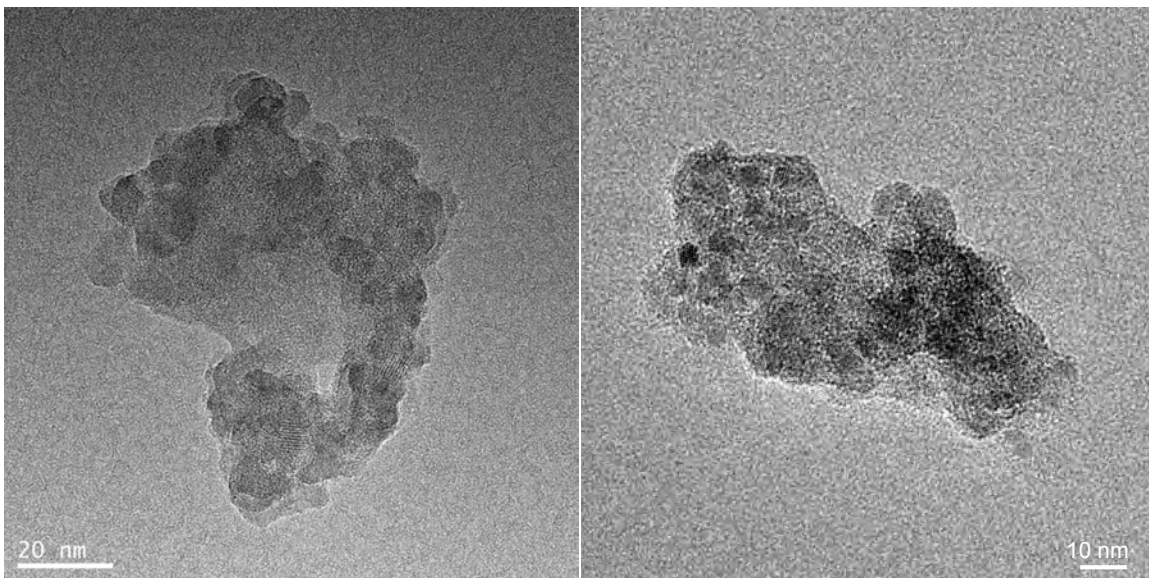


Fig. S10.

High-resolution TEM images of **3** after ball-milled into ~ 100 nm. Even smaller pieces of **3** still contain TiO_2 nanocrystals embedded in amorphous B_{12} -based clusters.

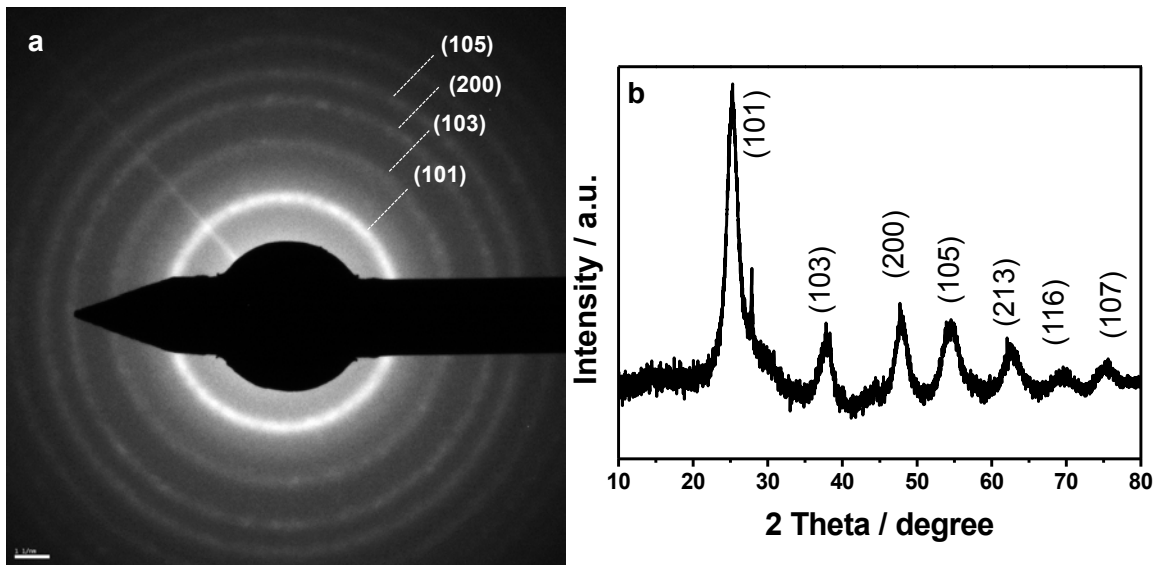


Fig. S11.

(a) Selected area electron diffraction (SAED) pattern of material **3**, confirming polycrystalline nature of the material. The individual diffraction rings can be indexed to anatase phase of TiO_2 ; (b) PXRD pattern for **3**, consistent with SAED assignment.

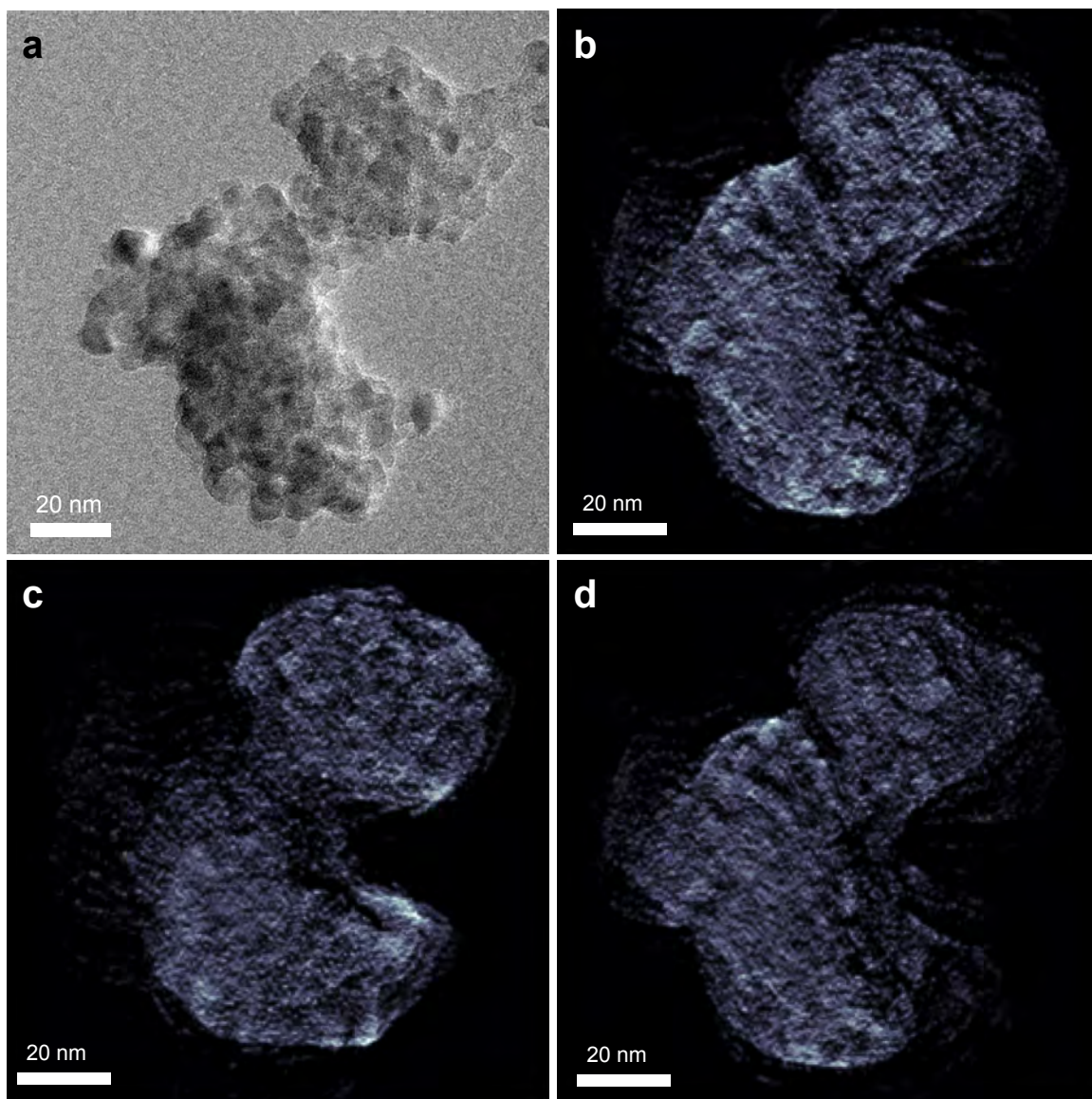


Fig. S12. (a) High-resolution TEM image of **3**. (b-d) The middle slice images of the 3D reconstructed density of **3** shown in (a) as viewed from different angles.

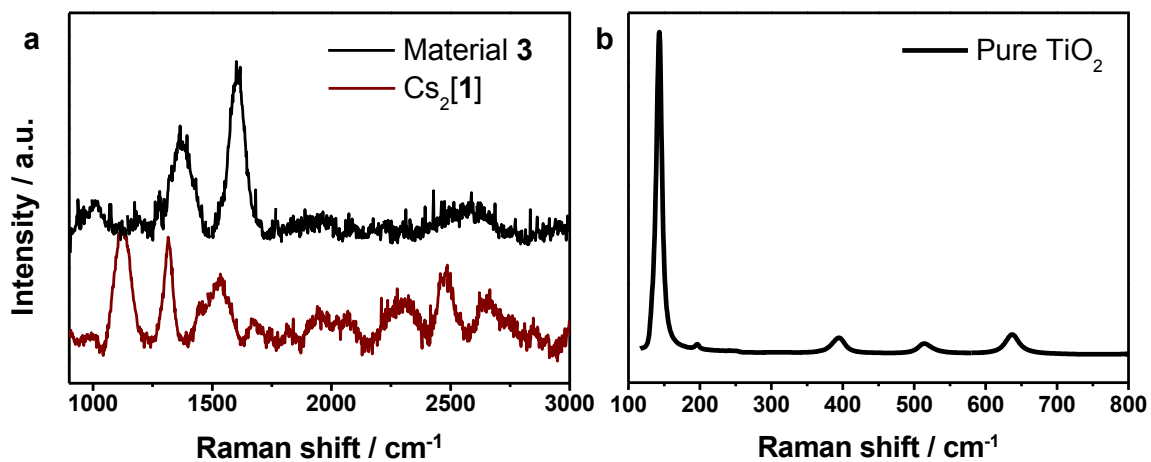


Fig. S13.

Raman spectra of (a) Cs₂[1] and material 3. No vibrational modes were observed below 1000 cm⁻¹, which is where modes associated with TiO₂ would be seen; (b) Raman of a sample of commercial TiO₂ for reference.

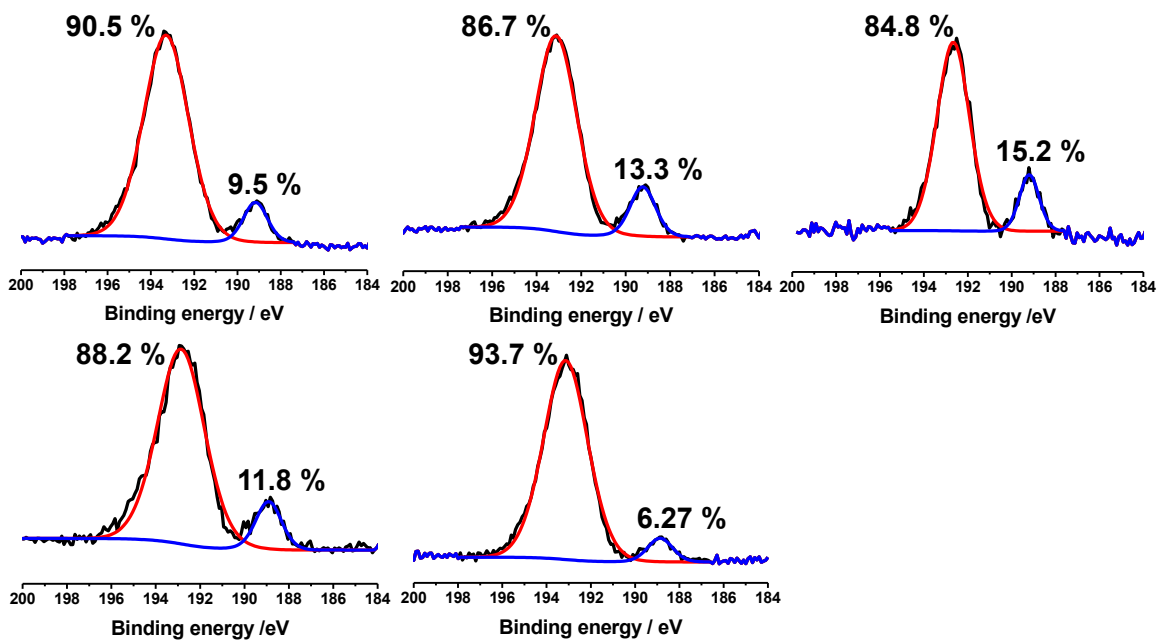


Fig. S14.

XPS obtained from five different material **3** samples, showing the boron 1s region. On average, 10 % of the boron content is intact clusters and 90 % of it is in oxidized form at the surface.

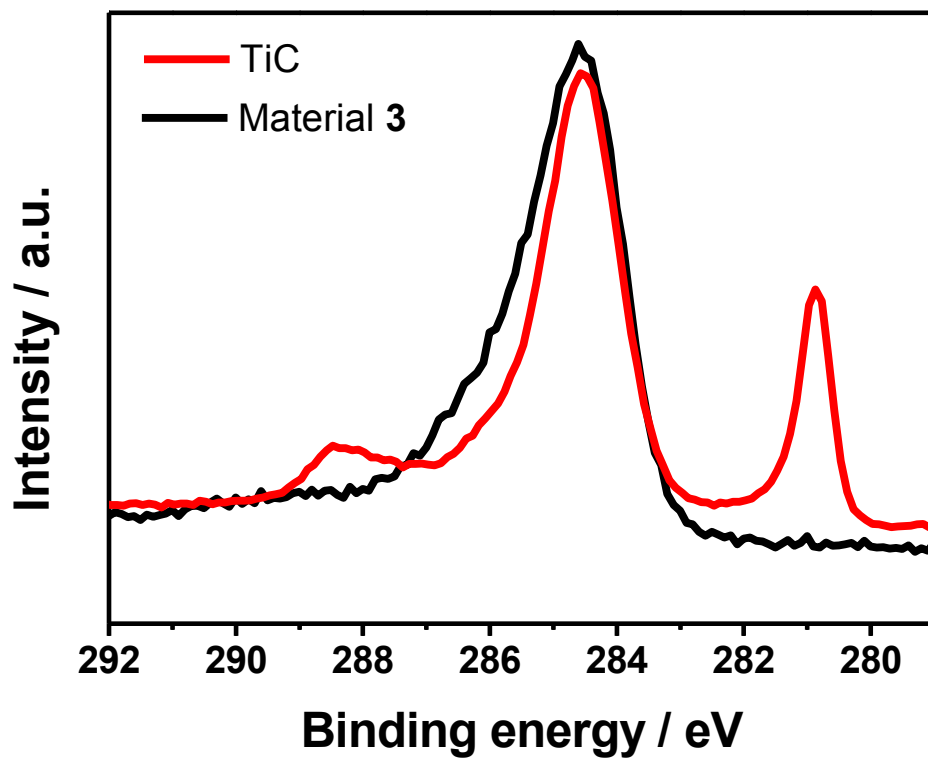


Fig. S15.

XPS for material 3, looking at the carbon 1s region. While graphitic carbon can be observed, a titanium carbide (TiC) control confirms no TiC in 3.

% Found	C	H	N
6 h reaction	8.72	2.03	0.98
20 h reaction	9.42	0.43	1.19

Table S2.

Combustion analysis of material **3** depending on the reaction time, showing the carbon content in **3** is independent of the reaction time.

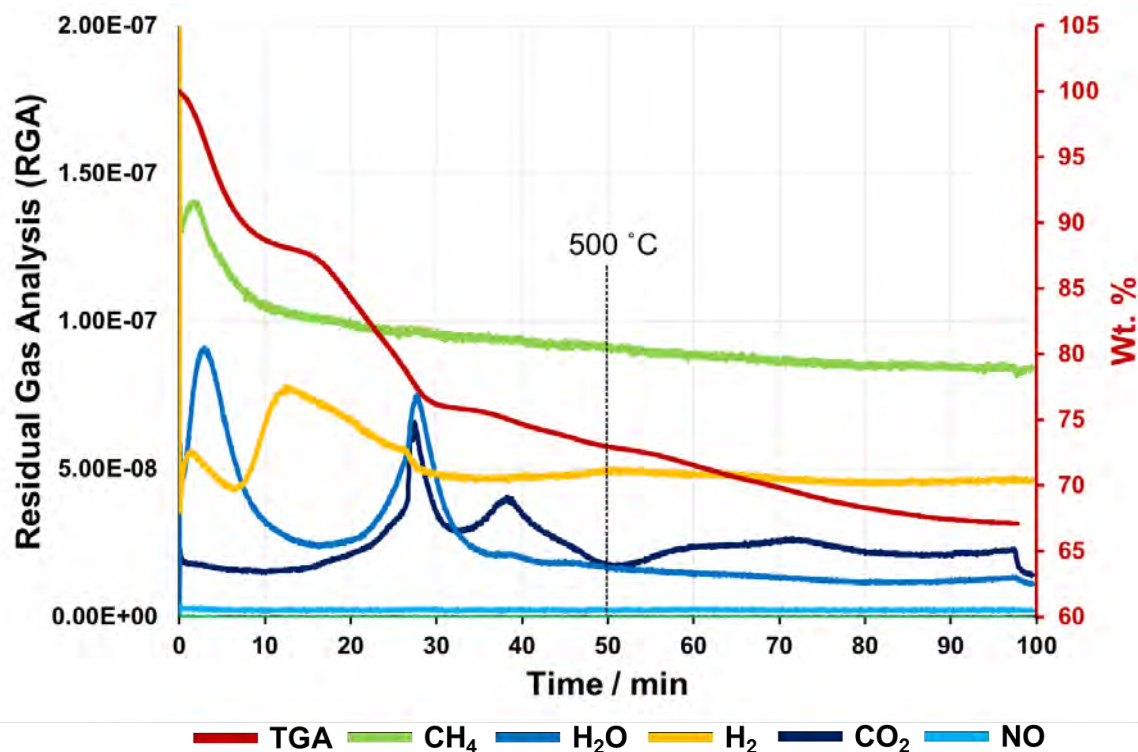


Fig. S16.

TGA-mass spectroscopy (TGA-MS) of pre-annealed material **3**. (A heating rate of 10 °C min⁻¹ was used, therefore the scale can be read as: 10 mins= 100 °C) Several different mass loss events are observed between room temperature and 450 °C, where water and then CO₂ are released in distinct phases. Between 450 °C and 550 °C however, production of CO₂ stops, and then begins again at >550 °C, with only concomitant minor mass loss.

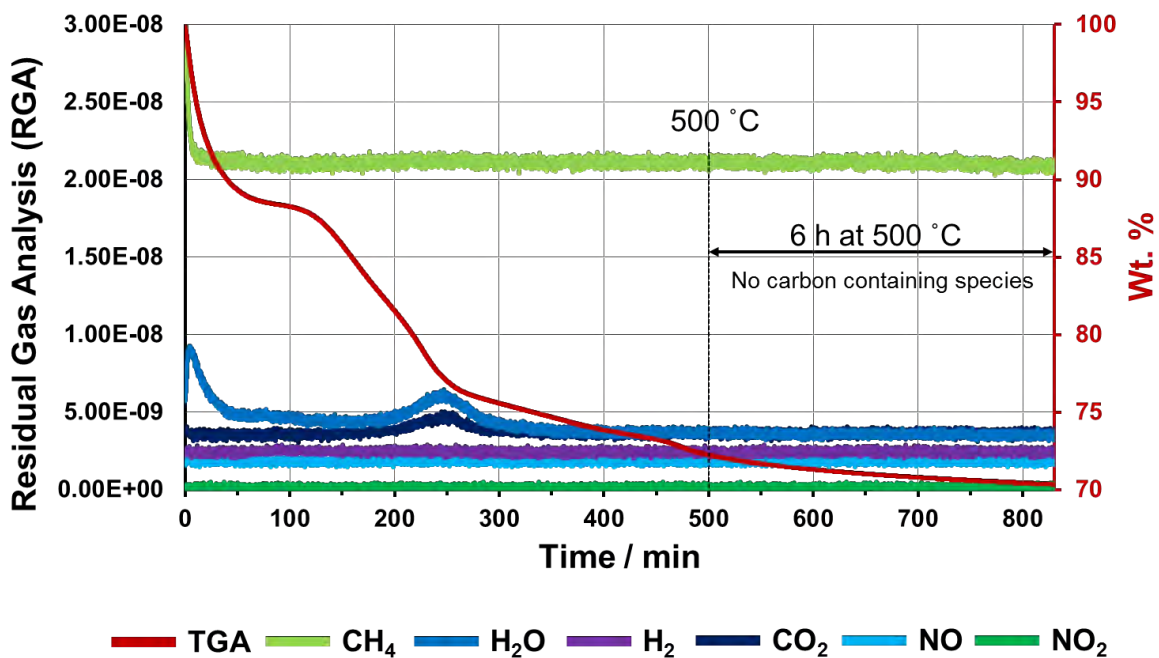


Fig. S17.

TGA-mass spectroscopy (TGA-MS) of pre-annealed material **3**, using the exact synthetic conditions: heating from room temperature to 500 °C at a rate of 1°C/min and holding at 500 °C for six hours. No carbon containing species are released during the annealing process, indicating remaining carbons are entrapped in **3**.

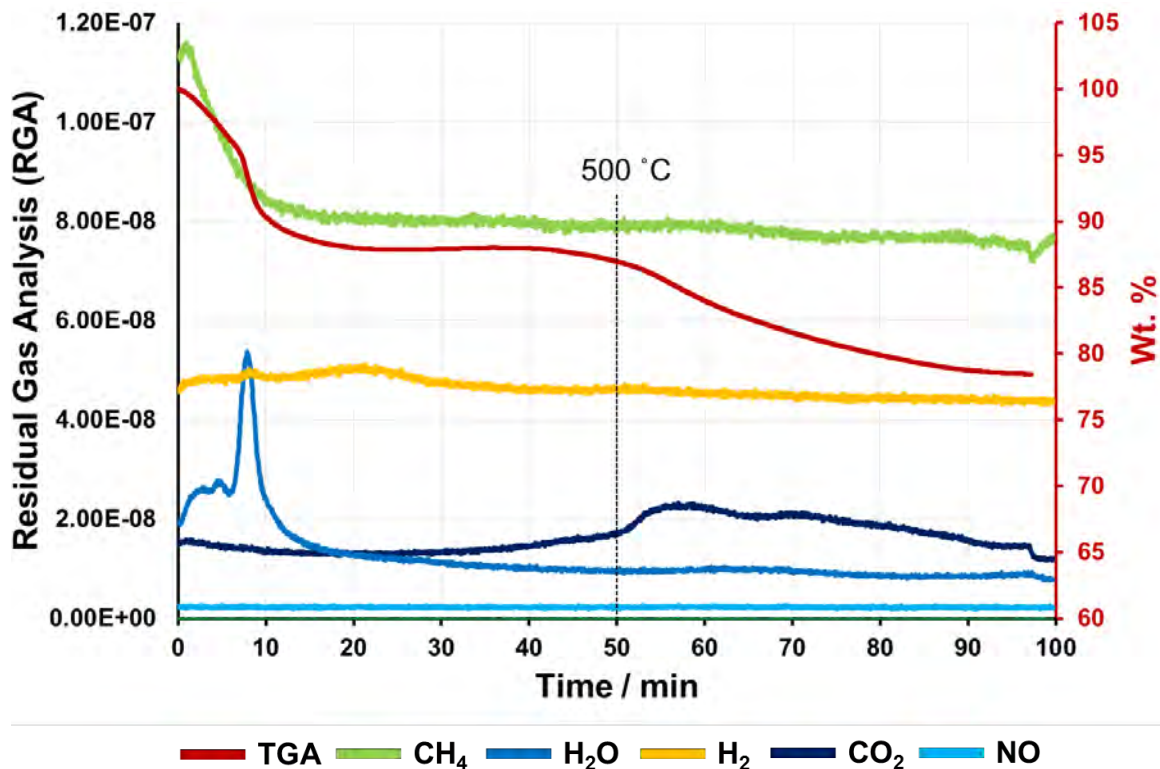


Fig. S18.

TGA-mass spectroscopy (TGA-MS) of material **3**, showing the different mass loss events during the annealing process to form **3**. (A heating rate of $10\text{ }^{\circ}\text{C min}^{-1}$ was used, therefore the scale can be read as: 10 mins = 100 °C)

Elemental Compositions in Atomic %

	C	B	O	Ti
1	44.7	10.5	37.3	7.5
2	42.3	13.8	37.6	6.3
3	32.3	10.9	45.9	10.9
4	32.7	10.9	44.9	11.5
Ave.	38.0	11.5	41.4	9.1

Table S3.

Elemental compositions in material **3** by TEM/EDX in atomic %. The high percentage of carbon is due to the carbon-based TEM grid.

Sample	Pre-edge energy / keV	Edge energy / keV	$N_{\text{Ti-O}}$	R / Å	$\Delta\sigma^2$ ($\times 10^3$)	E_o / eV	Comments
TiO ₂	4.9689, 4.9718, 4.9743	4.9785	6	1.96	0	-0.4	Ti(IV) Ref
Ti ₂ O ₃	-	4.9678	-	-	-	-	Ti(III) Ref
TiO	-	4.9668	-	-	-	-	Ti(II) Ref
TiC	-	4.9668	-	-	-	-	Ti(II)
TiB ₂	-	4.9677	-	-	-	-	Ti(III)
Ti foil	-	4.9660	-	-	-	-	Calibration
Material 3	4.9690, 4.9707, 4.9741	4.9790	4.2	1.95	3.0	-0.3	Ti(IV)

Table S4.

Table showing the summary of the results from XANES and EXAFS for material **3** and several reference materials. The XANES of pre-edge peaks and edge energy of **3** are consistent with Ti(IV) oxide.

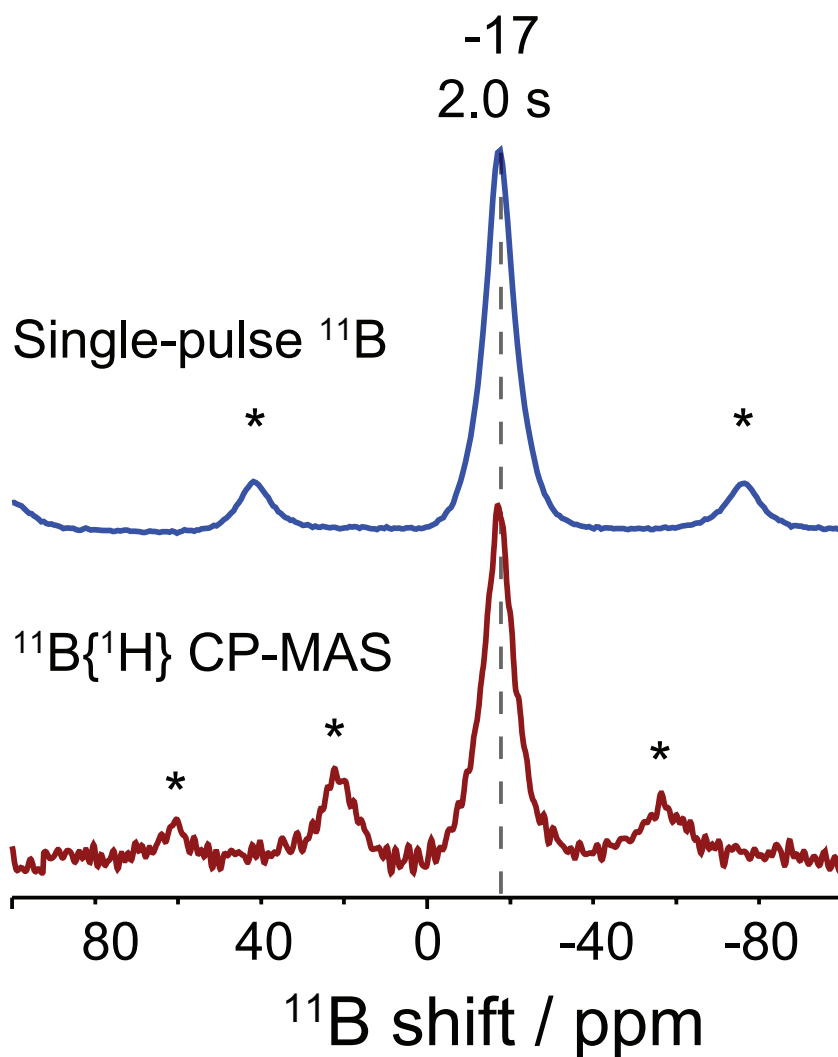


Fig. S19.

Solid-state 1D single-pulse ^{11}B MAS NMR (top) and $^{11}\text{B}\{^1\text{H}\}$ CP-MAS (bottom) spectra of a reference material containing intact B_{12} clusters, $\text{Cs}_2[\mathbf{1}]$, acquired at 18.8 T and 298 K. A single ^{11}B signal (9 ppm FWHM) at -17 ppm is detected from the molecular B_{12} clusters. The ^{11}B spin-lattice relaxation behavior of $\text{Cs}_2[\mathbf{1}]$ showed no signs of paramagnetic interactions and the ^{11}B T_1 relaxation times was measured to be 2.0 s.

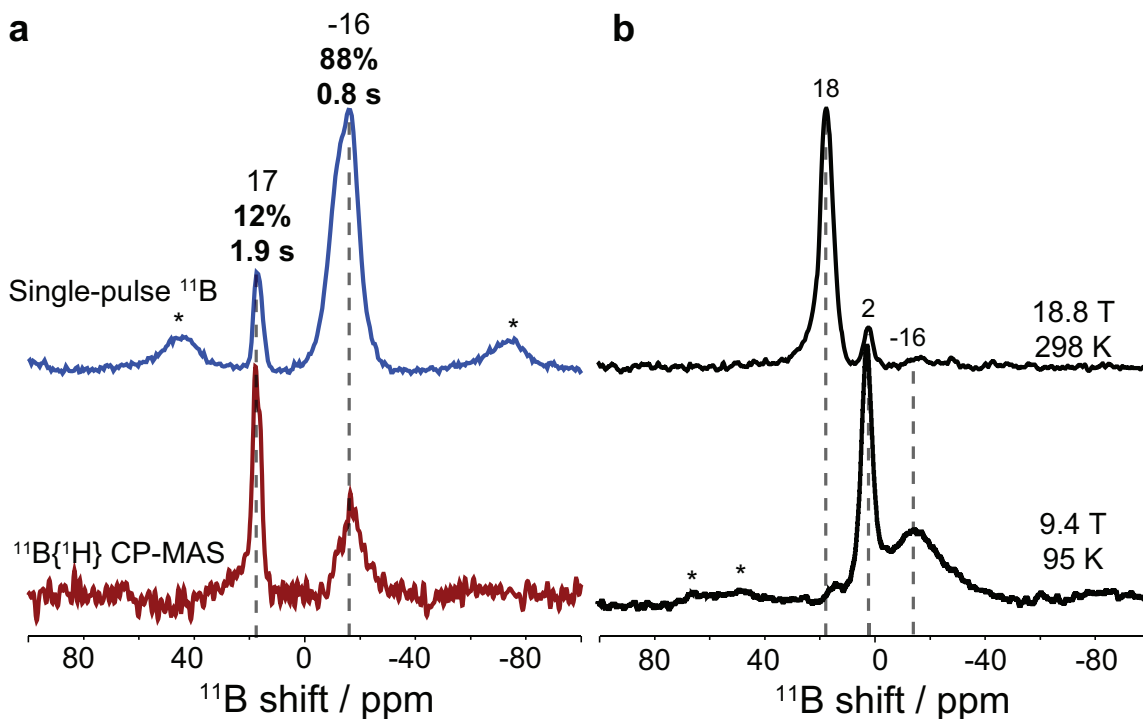


Fig. S20.

(a) Solid-state 1D single-pulse ^{11}B MAS NMR (top) and $^{11}\text{B}\{^1\text{H}\}$ CP-MAS (bottom) spectra of pre-annealed material **3**, showing that the majority of the sample is still composed of intact boron clusters; (b) $^{11}\text{B}\{^1\text{H}\}$ CP-MAS spectra of material **3** obtained at 18.8 T and 298 K (top) and 9.4 T and 95 K (bottom). At the lower temperature, paramagnetic relaxation effects are slowed, enabling better CP-MAS enhancement of the signals at 2 ppm and -16 ppm. However, the ^{11}B signal at 18 ppm is greatly broadened at the lower magnetic field strengths due to the field-dependent quadrupolar interactions of boron oxide³ and reappearance of the peak at -16 ppm suggests that the associated boron atoms are in a highly symmetrical environment, as found for boron atoms in a cluster. The molecular B_{12} are then likely cross-linked and terminated by B-O-B and B-O-Ti bonds, consistent with their incorporation into the metal oxide matrix. Asterisks indicate spinning sidebands.

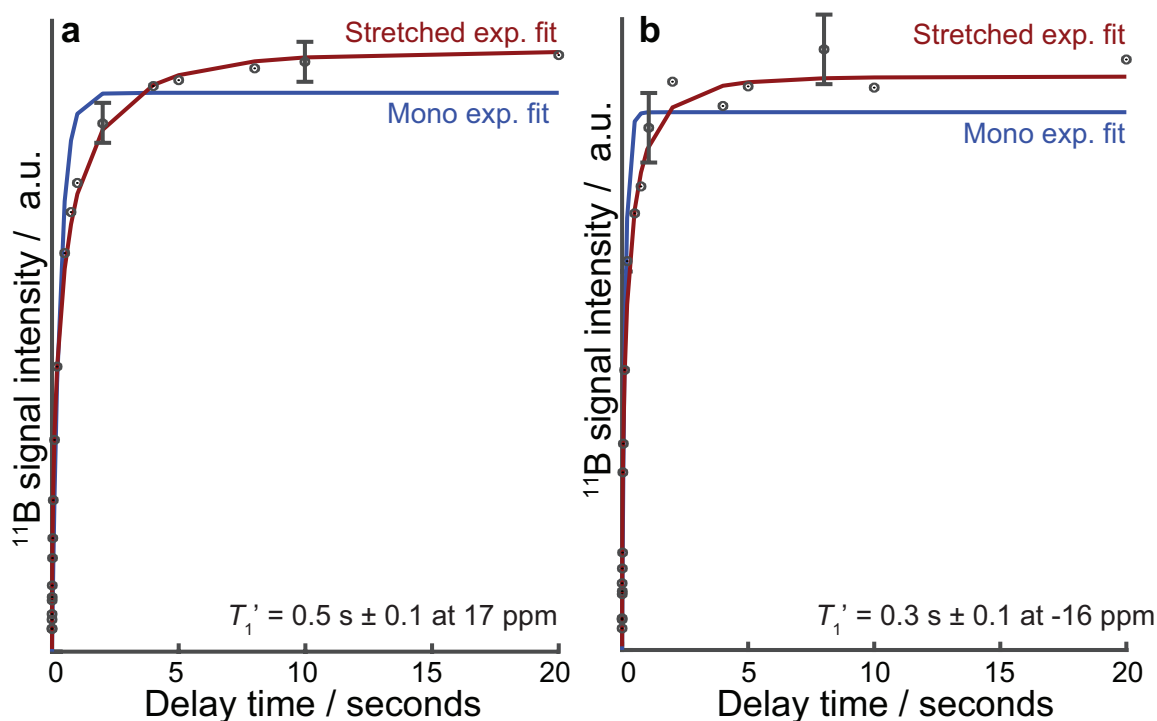


Fig. S21.

^{11}B relaxation analysis of material **3**. Measured ^{11}B saturation recovery signal intensities (black points) compared with stretched (red) and mono- (blue) exponential fitting functions for the ^{11}B signals at (a) 17 ppm and (b) -16 ppm. The measured ^{11}B signal intensities show good agreement with the stretched exponential function as expected for paramagnetic relaxation. The different ^{11}B species in material **3** are proximate to paramagnetic centers, as evidenced by ^{11}B spin-lattice (T_1) relaxation measurements, which are strongly influenced by the interactions of nuclear spins and unpaired electrons. Analysis of the ^{11}B T_1 relaxation behaviors shows that the different ^{11}B species in material **3** each exhibit a distribution of T_1 relaxation times. These distributions can be described by a stretched exponential function with a characteristic relaxation time T_1' and a stretched exponent of 0.5, which is typical of nuclear T_1 relaxation that arises from coupling to paramagnetic electron spins^{4,5}. The measured ^{11}B T_1' relaxation times of material **3** are shown in Fig. 4a the respective ^{11}B signals. The species associated with the ^{11}B signal at -16 ppm exhibited the shortest T_1' (0.3 s), suggesting that they are closest to the paramagnetic centers in material **3**, which, on the basis of the EPR results, are likely localized on the molecular boron clusters.

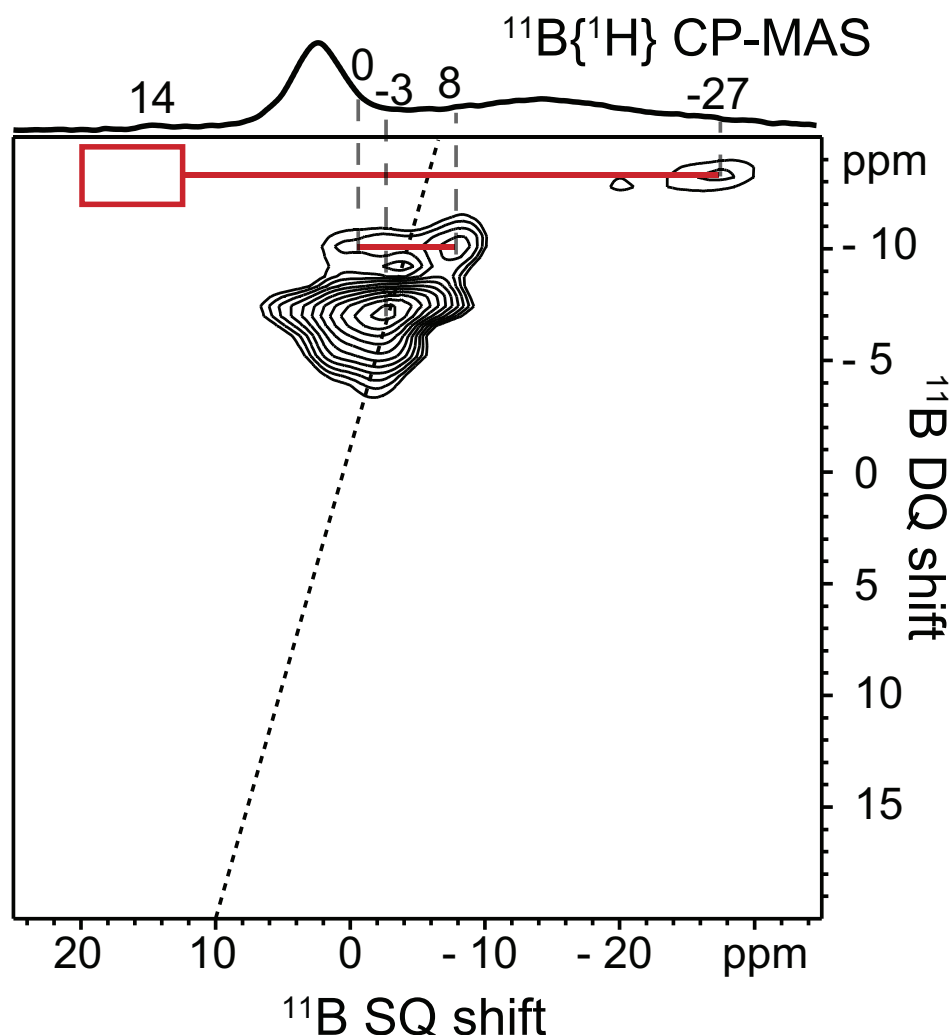


Fig. S22.

Two-dimensional dipolar-mediated (through-space) $^{11}\text{B}\{^{11}\text{B}\}$ correlation spectrum of material **3**, acquired at 9.4 T, 4.6 kHz MAS, and under low temperature conditions of 95 K to slow the nuclear spin relaxation kinetics and allow for more efficient dipolar recoupling. A 1D $^{11}\text{B}\{^1\text{H}\}$ CP-MAS spectrum acquired under the same conditions is shown above for comparison with the 2D spectrum. ^{11}B signals correlated across the diagonal arise from ^{11}B - ^{11}B spin pairs which are dipole-dipole coupled through space (< 1 nm). The 2D spectrum shows signals at ^{11}B SQ shift positions of 0, -3, and -8 ppm, all of which arise from ^{11}B species in B_{12} clusters that are in close mutual proximities. Additionally, a signal at SQ: -27 ppm indicates that the B_{12} clusters are in close molecular proximity (< 1 nm) with ^{11}B species in the boron oxide matrix (red line). The expected corresponding pair signal intensity around 14 ppm is not observed (red box), likely due to quadrupolar broadening of the ^{11}B signals from boron oxide at the lower magnetic field strengths (9.4 T) used to acquire the 2D dipolar-mediated NMR spectrum (see Fig. S20). Taken together, the 2D $^{11}\text{B}\{^{11}\text{B}\}$ NMR results establish the interconnectivities of intact B_{12} clusters, as well as the nanoscale proximities of B_{12} clusters with the oxide matrix.

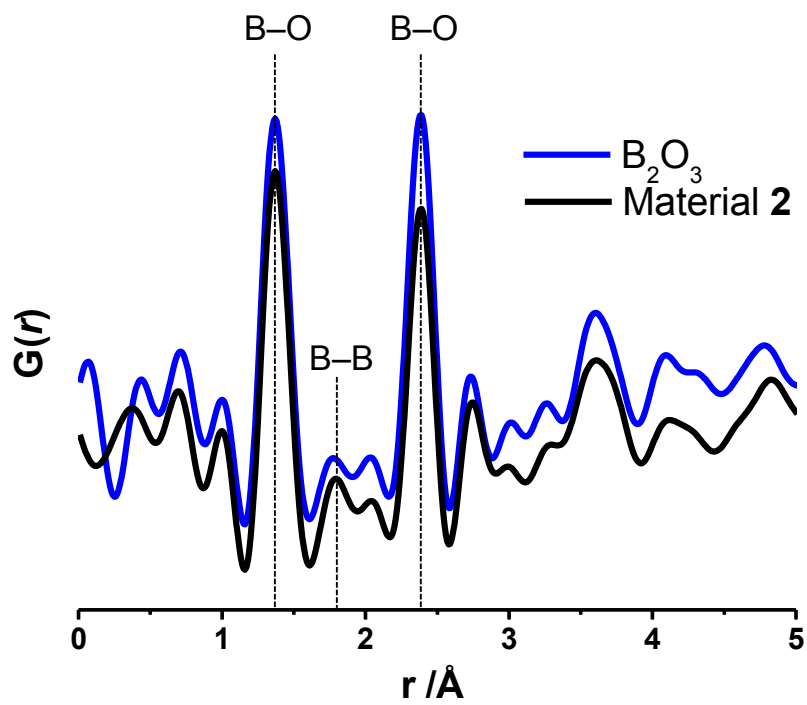


Fig. S23.

Pair distribution function (PDF) analysis of material 2 and B_2O_3 control. Although reduced in intensity, the peak corresponding to B-B bound atoms (at $\sim 1.87 \text{ \AA}$) can be observed for 2.

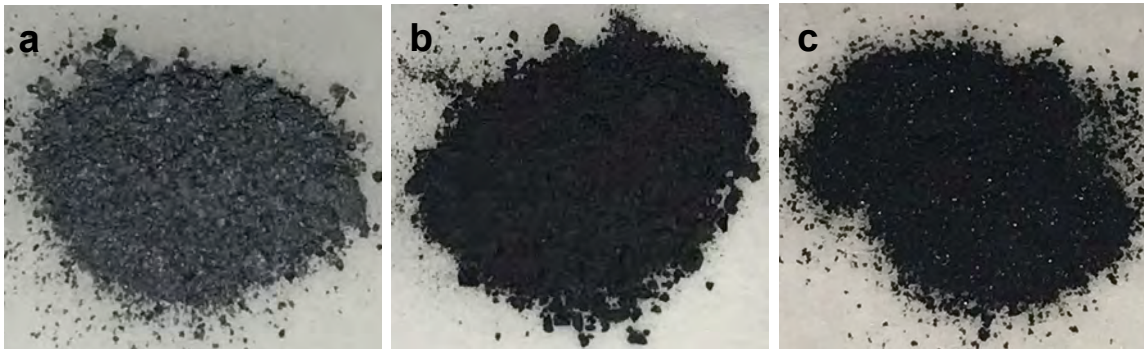


Fig. S24.

A control reaction was performed where 10 % graphite (by mass) was added to $\text{Ti}(\text{O}^i\text{Pr})_4$, hydrolyzed and annealed under the same conditions for materials **2** and **3** to form a composite graphitic TiO_2 material (image **a**). The combustion analysis confirmed the composite graphitic TiO_2 contained ~5 % carbon. The optical images show that this material, despite its similar carbon content, was a grey color rather than the intense black of materials **2** (image **b**) and **3** (image **c**) suggesting that the carbon content alone in the material is insufficient to produce the observed color.

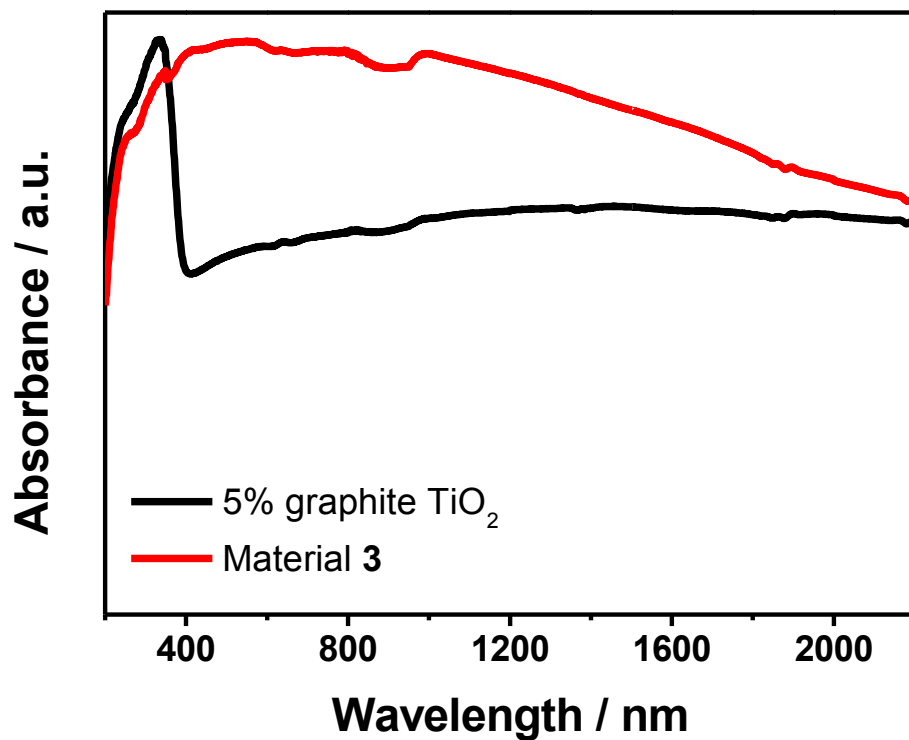


Fig. S25.

Diffuse reflectance UV-Vis spectroscopy of a composite graphitic TiO₂ (Fig. S24a) and material 3, showing different light absorption properties. This experiment clearly suggests that the carbon content alone is insufficient to produce the strong light absorption properties.

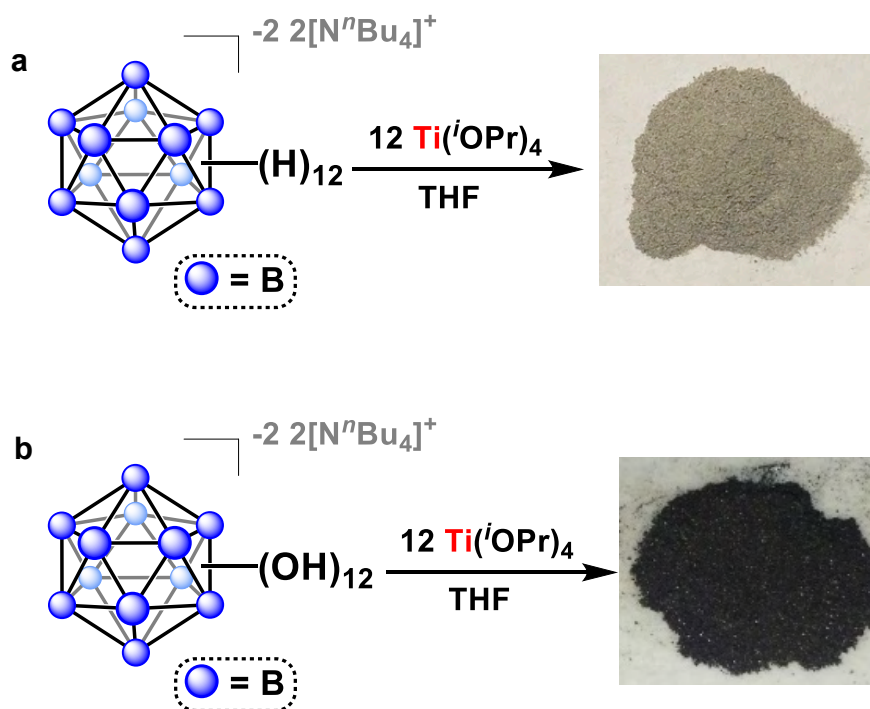


Fig. S26.

(a) A control reaction was performed where $[N^tBu_4]_2[B_{12}H_{12}]$ was added to $Ti(O^iPr)_4$, hydrolyzed and annealed under the same conditions for materials **3** to form a non cross-linked TiO_2 material. (b) A synthetic route to produce material **3**. These results further corroborate that cross-linking B_{12} -based clusters is indeed important for the observed black color.

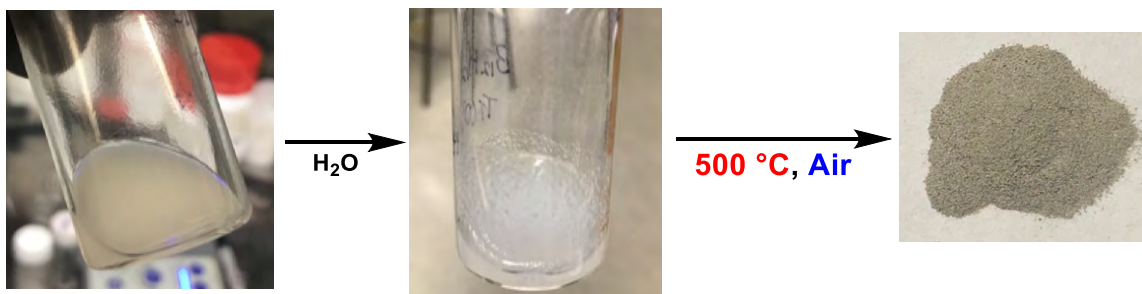


Fig. S27.

A reaction of $[\text{N}^i\text{Bu}_4]_2[\text{B}_{12}\text{H}_{12}]$ with $\text{Ti}(\text{O}^i\text{Pr})_4$ in THF. It produces a cloudy white solution, which is subsequently hydrolyzed to form a white slurry. After calcining at $120\text{ }^\circ\text{C}$, the solid is annealed at $500\text{ }^\circ\text{C}$ in air to produce a non cross-linked TiO_2 material.

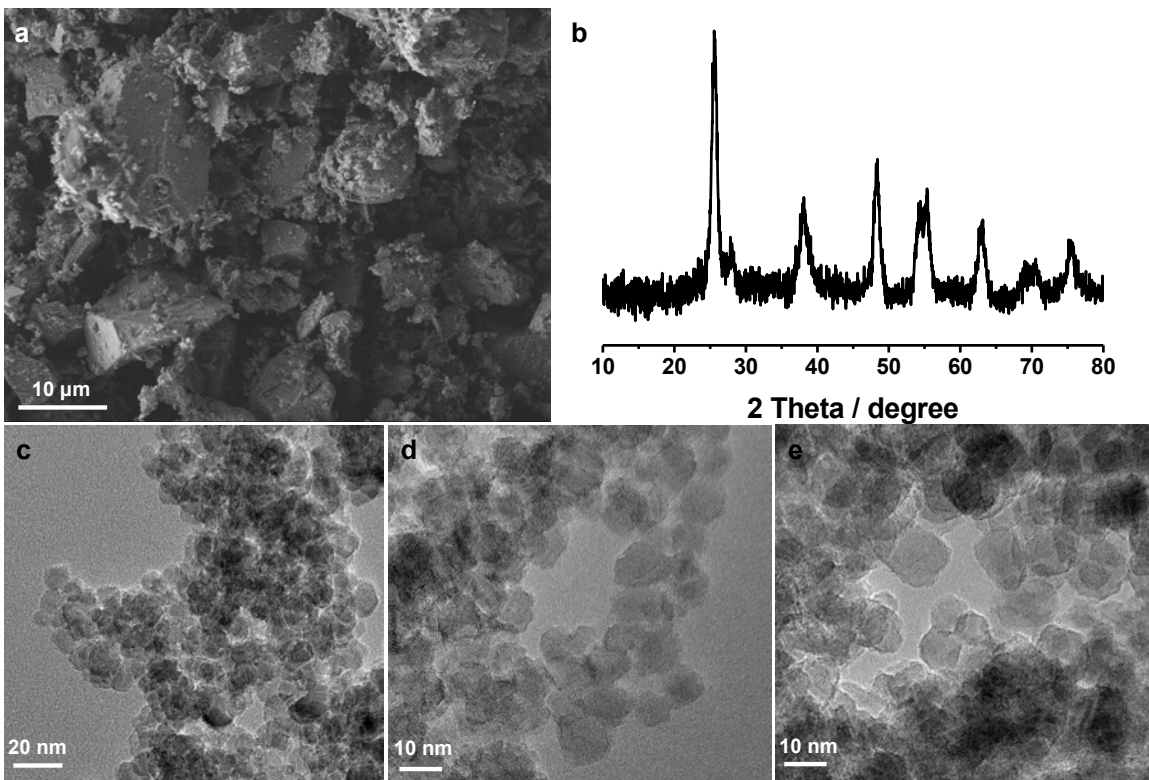


Fig. S28.

(a) SEM image; (b) PXRD pattern; (c-e) TEM images of a non cross-linked TiO₂ (see Fig S27). Based on the structural characterizations, we confirmed the resulting compound did not have a cross-linked morphology.

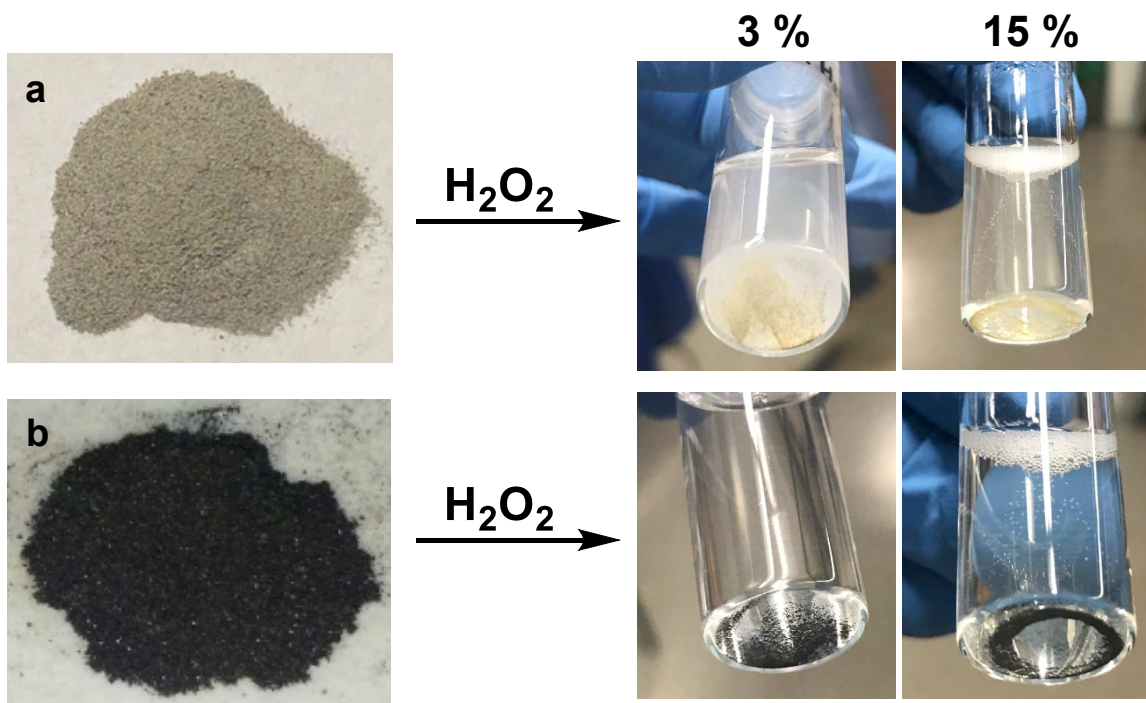


Fig. S29.

Chemical stability test of (a) a non cross-linked TiO_2 and (b) material **3** in 3 % and 15 % H_2O_2 . While **3** resisted prolonged exposure to both 3 % and 15 % H_2O_2 , a non cross-linked TiO_2 lost its color upon the exposure to H_2O_2 . Given the light color and weak chemical stability of the non cross-linked TiO_2 , cross-linking B_{12} -based clusters to TiO_2 is indeed important for the observed intense color and robustness.

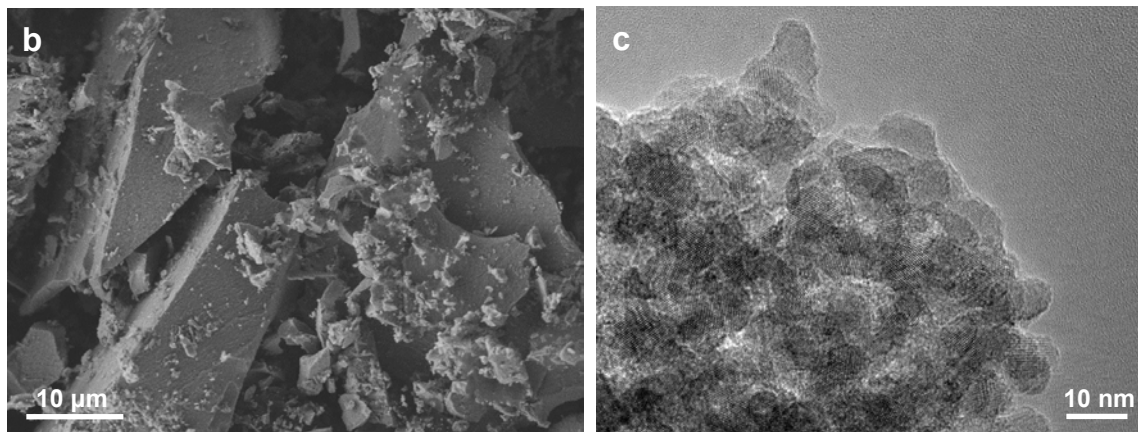
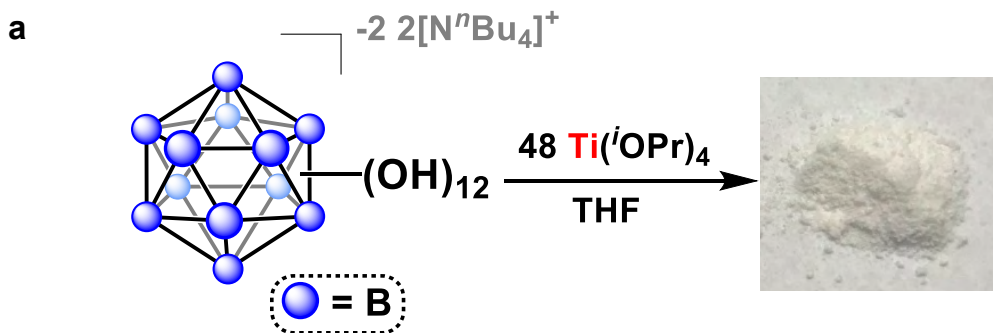


Fig. S30.

(a) A control reaction was performed where $[\text{N}^n\text{Bu}_4]_2[\mathbf{1}]$ was added to 48 equivalent of $\text{Ti}(\text{O}^i\text{Pr})_4$, which is four times more titanium precursors than material **3**. It was then hydrolyzed and annealed under the same conditions for materials **3** and the resulting compound was a white powder as the excess TiO_2 diluted the amount of the cross-linkers. (b) SEM image; (c) TEM image of the resulting compound, showing the cross-linked morphology to some extent.

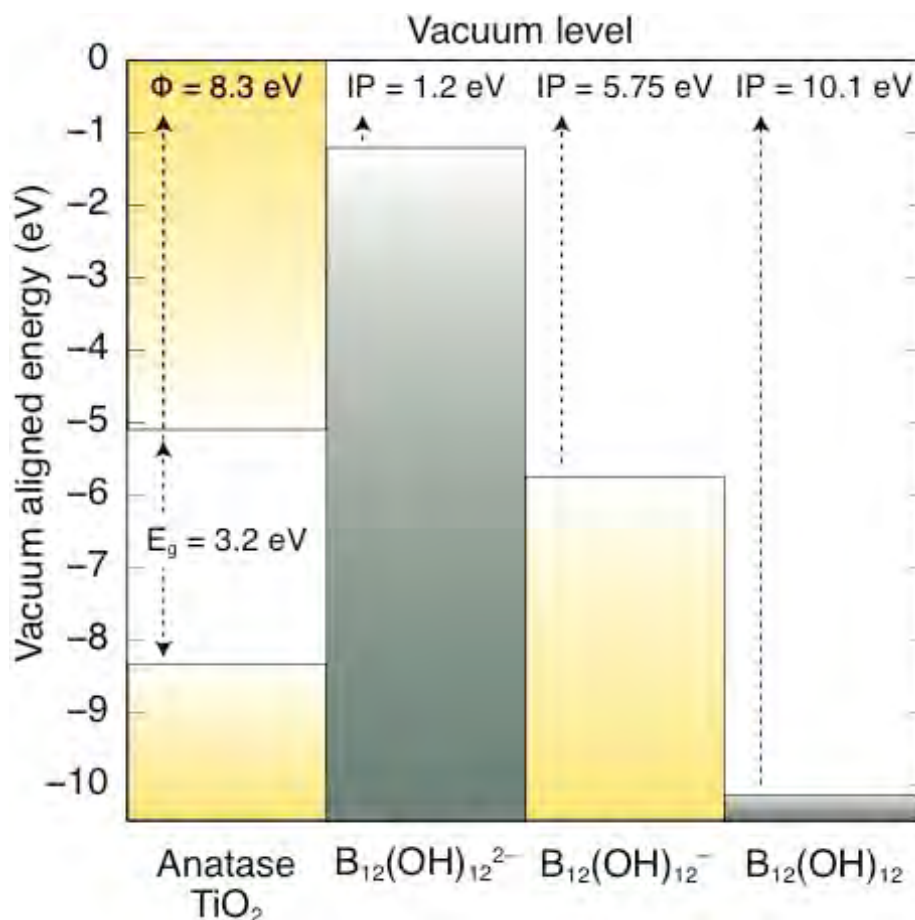


Fig. S31.

Electron energy alignments of anatase TiO₂, and B₁₂-based clusters in different oxidation states. Anatase TiO₂ has a band gap of 3.2 eV and a work function of 8.3 eV (*Nature Mater.* **2013**, *12*, 798). The [B₁₂(OH)₁₂]²⁻ species has an extremely low ionization potential (IP = 1.2 eV), indicating that the valence electrons are loosely bound, or highly reducing. Upon single electron oxidation, [B₁₂(OH)₁₂]⁻ features a HOMO located midgap to TiO₂, resulting in an extremely narrow charge transfer excitation (0.65 eV) which would give rise to a black material and absorption in the near IR to some extent. The charge neutral compound, B₁₂(OH)₁₂ is stable, with tightly bound valence electrons as evidenced by the ionization potential = 10.1 eV. In this case, the zero charge clusters would be expected to deplete TiO₂ of electron density from the oxygen valence of TiO₂, making an electron deficient O-Ti site. Based on the similar light absorption properties observed in material **2** and **3**, a variety of charge transfer transitions would likely give rise to the broad absorbance: intervalence charge transfers between clusters in different valence states, and charge transfers between the clusters and the boron/titanium oxides, as well as some absorbance from trapped carbon.

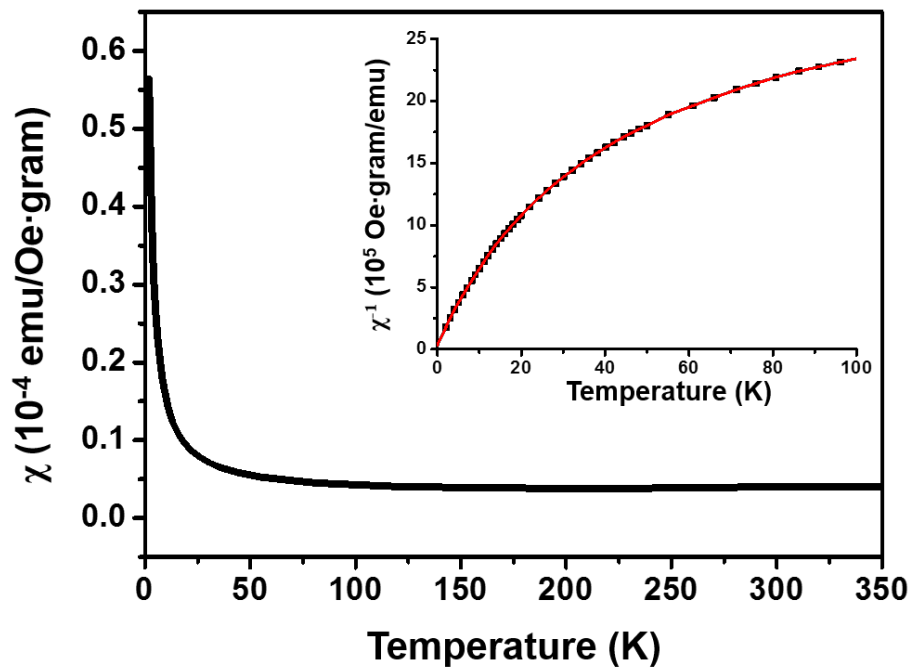


Fig. S32.

Plot of the SQUID magnetometric data obtained for material **3**, along with a plot of inverse of the magnetic susceptibility against temperature (inset).

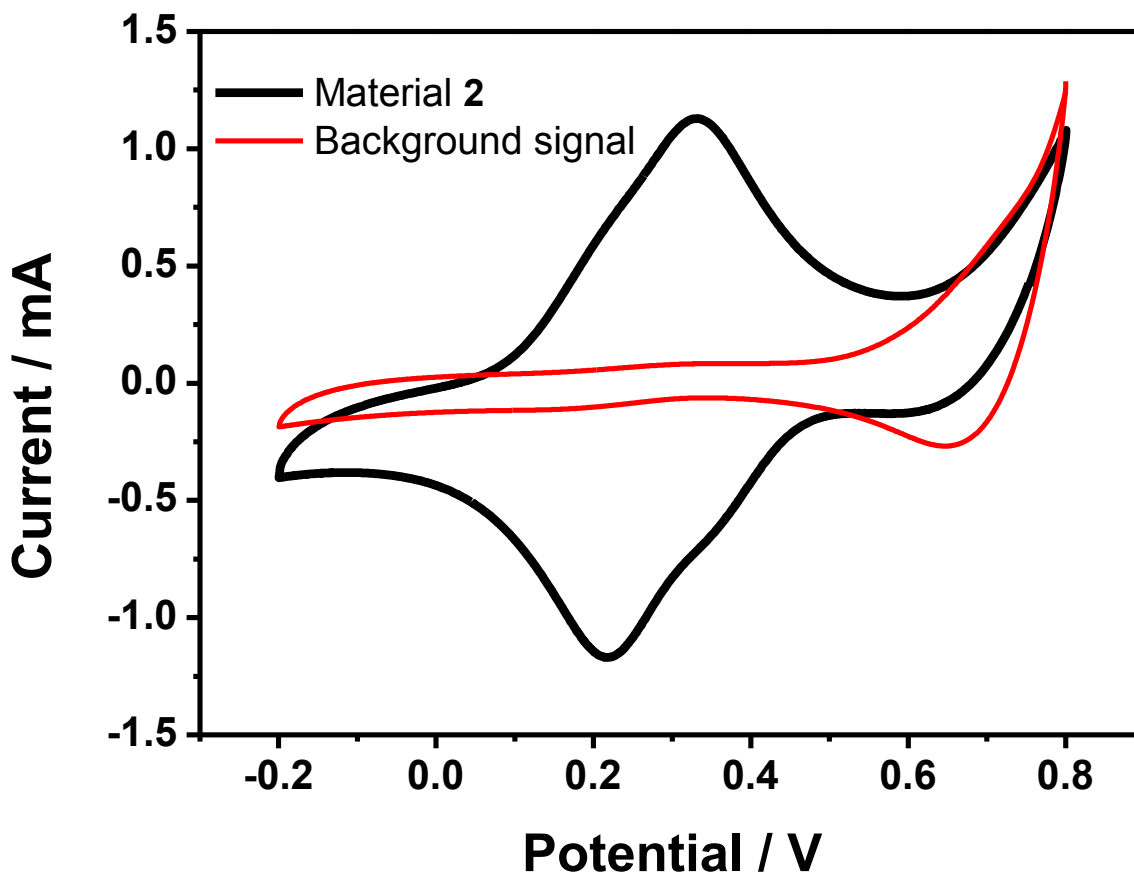


Fig. S33.

CV curves of material **2** for the ferri/ferrocyanide redox couple (black) and the supporting electrolyte only (red). Material **2** is electrochemically active by itself, but the peak-to-peak separation (116 mV) is larger than material **3** (89 mV). The oxidation wave at 0.8 V is consistent with the previously observed redox feature of unfunctionalized $[\text{B}_{12}(\text{OH})_{12}]^{2-}$ cluster undergoing single electron oxidation to a radical species $[\text{B}_{12}(\text{OH})_{12}]^{1-6}$.

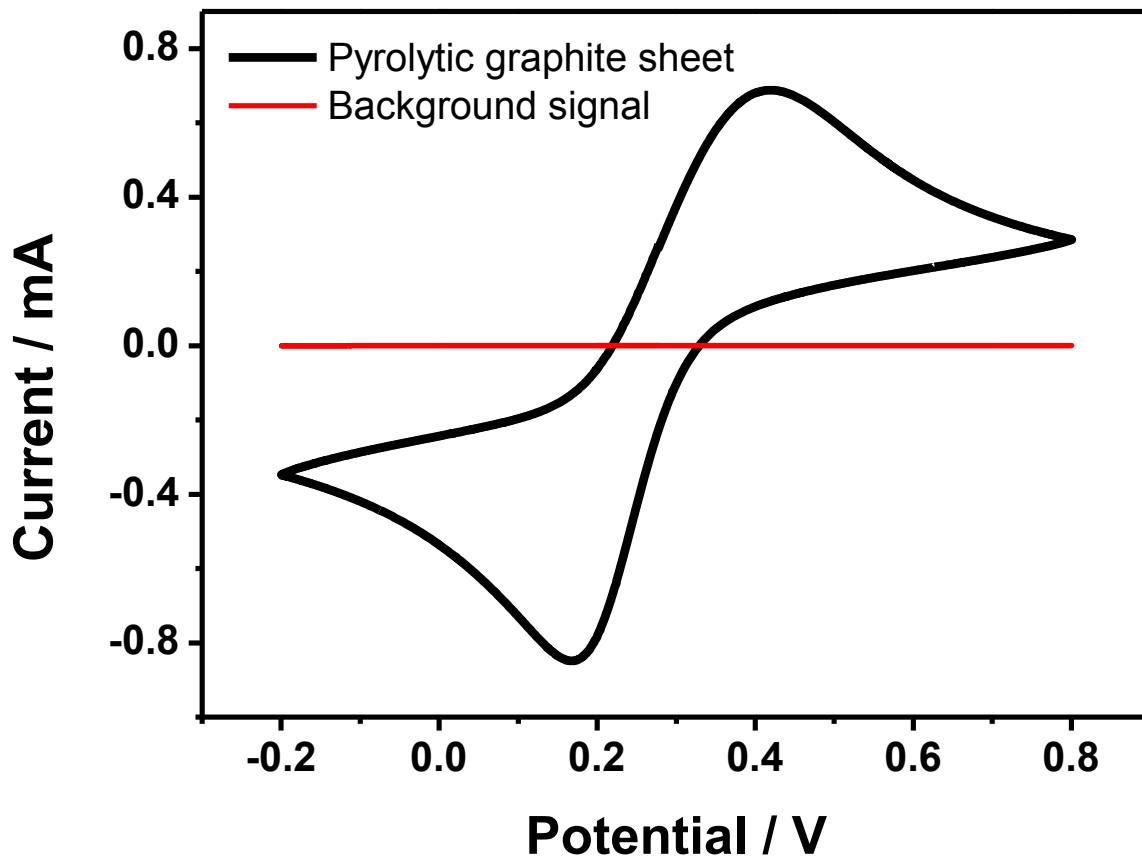


Fig. S34.

CV curves of pyrolytic graphite sheet electrodes for the ferri/ferrocyanide redox couple (black) and the supporting electrolyte only (red). The peak-to-peak separation of the pyrolytic graphite sheet (253 mV) is much larger than material **3** (89 mV).

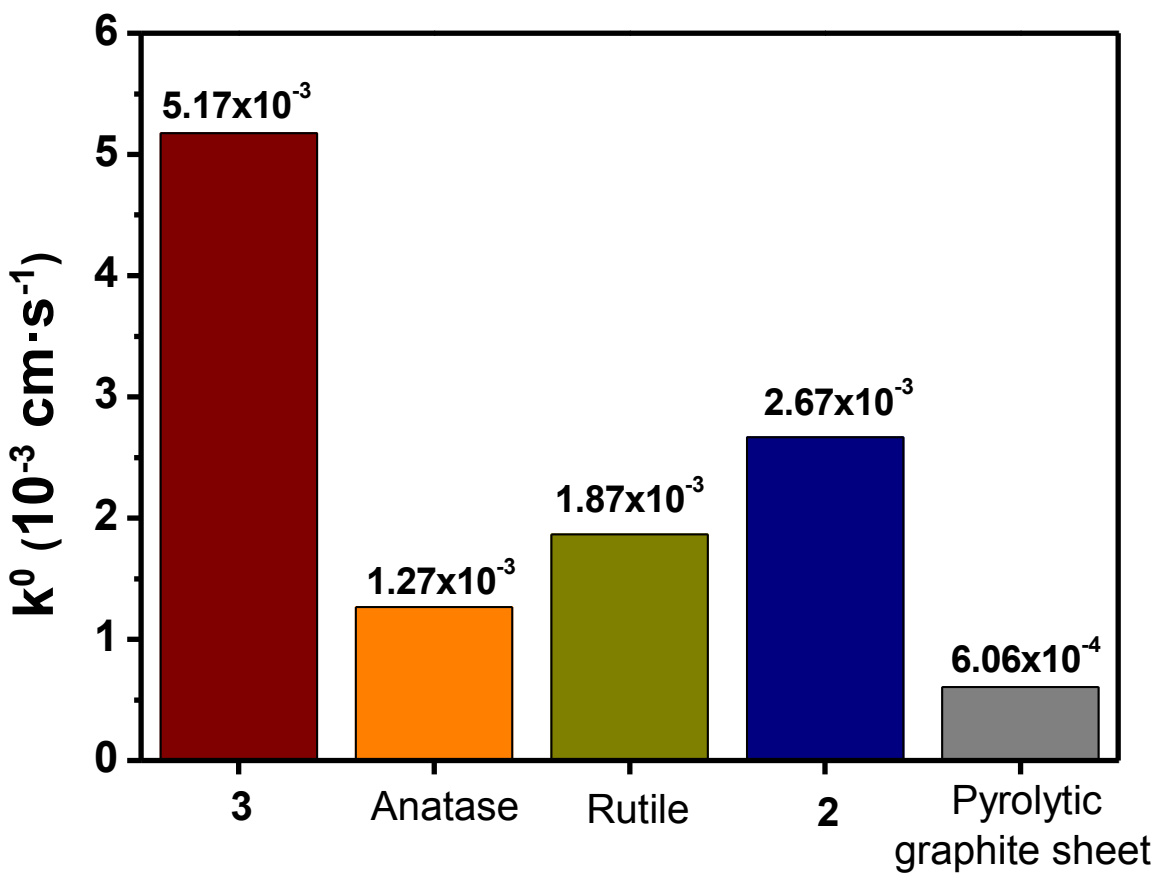


Fig. S35.

Bar chart showing the electron transfer rate constants for material **3**, anatase, rutile TiO₂, material **2**, and pyrolytic graphite sheet. Commercially available TiO₂ consists of spherical nanoparticles with ~100 nm in diameter (see Fig. S36b). In this case, charge transfer is limited to the surface of the material only. On the other hand, material **3** contains nanocrystalline TiO₂ (<10 nm) cross-linked with B₁₂-based clusters, while the bulk material itself remains micron-sized. This features a unique structure, creating internal mesopores that can act as electrolyte solution reservoirs. This explains the faster electron transfer kinetics at the material **3** electrodes. Charge transfer occurs at the electrode/electrolyte interface, meaning that a material with higher surface area will possess more active sites where the charge transfer may occur. Material **3** has high specific surface area, leaving behind 3 nm mesopores that provide more room for charge transfer to occur (see Fig. S37). Additionally, defect sites on the structure such as step edges shown in Figure S29a are responsible for the favorable electrochemical activity^{7,8}. The improved electrical conductivity of material **3** than commercial TiO₂ (see Fig. S43d) and material **2** (see Fig. S41) also results in the faster charge transfer kinetics⁹.

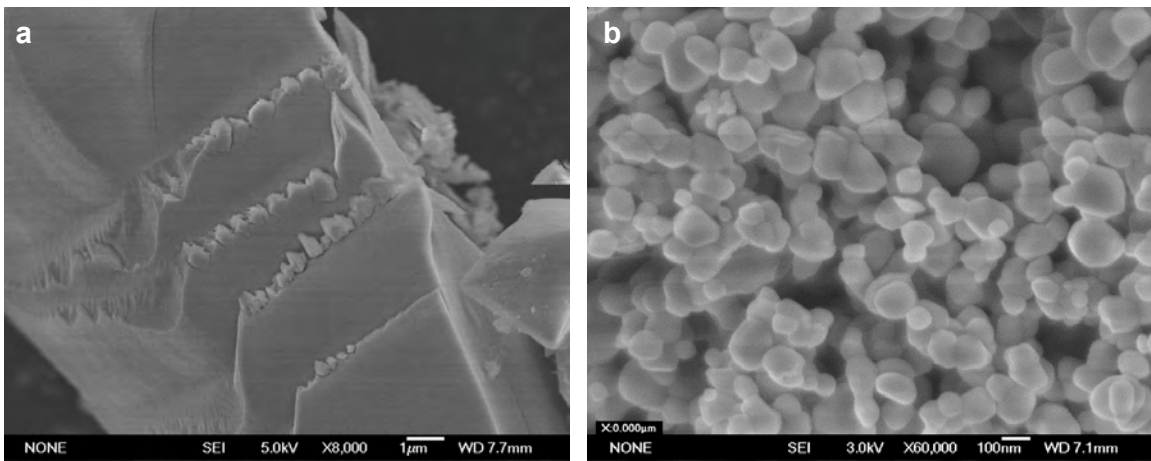


Fig. S36.
SEM images of (a) material 3; (b) anatase TiO₂.

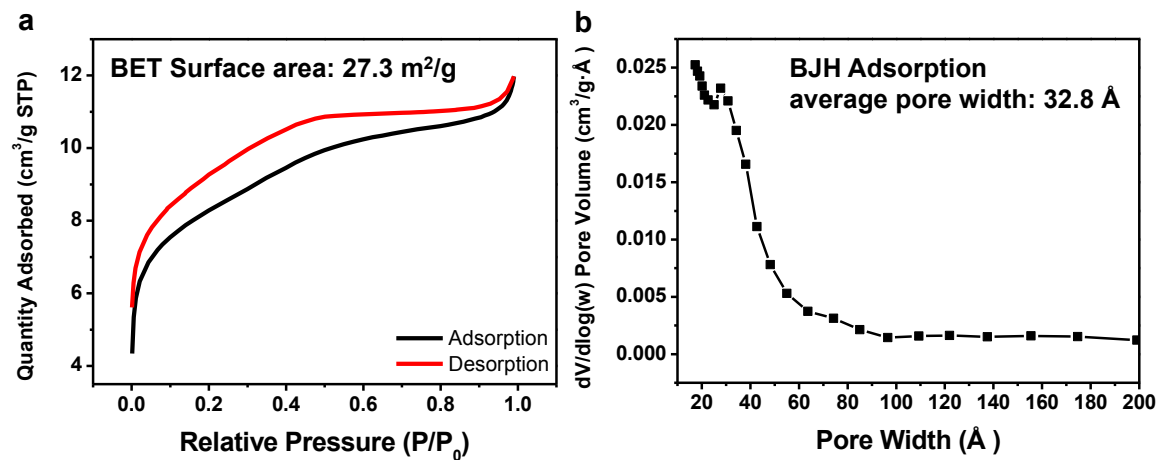


Fig. S37.

(a) Low pressure N₂ adsorption isotherms of material **3**. The Brunauer-Emmett-Teller (BET) surface area is 27.3 m²/g; (b) Calculated pore size distribution of material **3** using the Barret-Joyner-Halenda (BJH) equation.

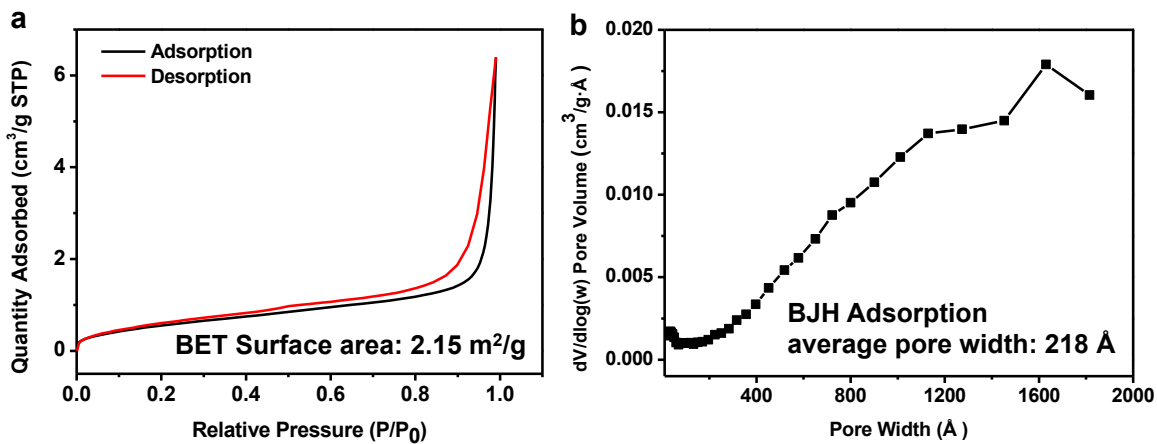


Fig. S38.

(a) Low pressure N₂ adsorption isotherms of material **2**. The Brunauer-Emmett-Teller (BET) surface area is 2.15 m²/g; (b) Calculated pore size distribution of material **2** using the Barret-Joyner-Halenda (BJH) equation.

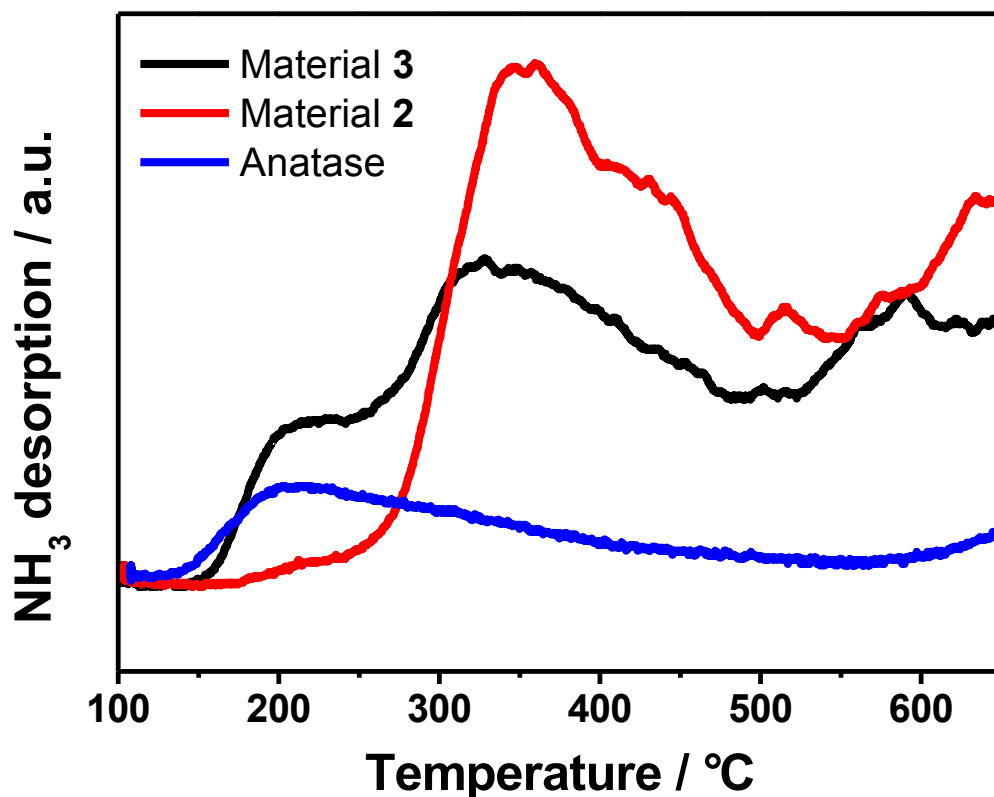
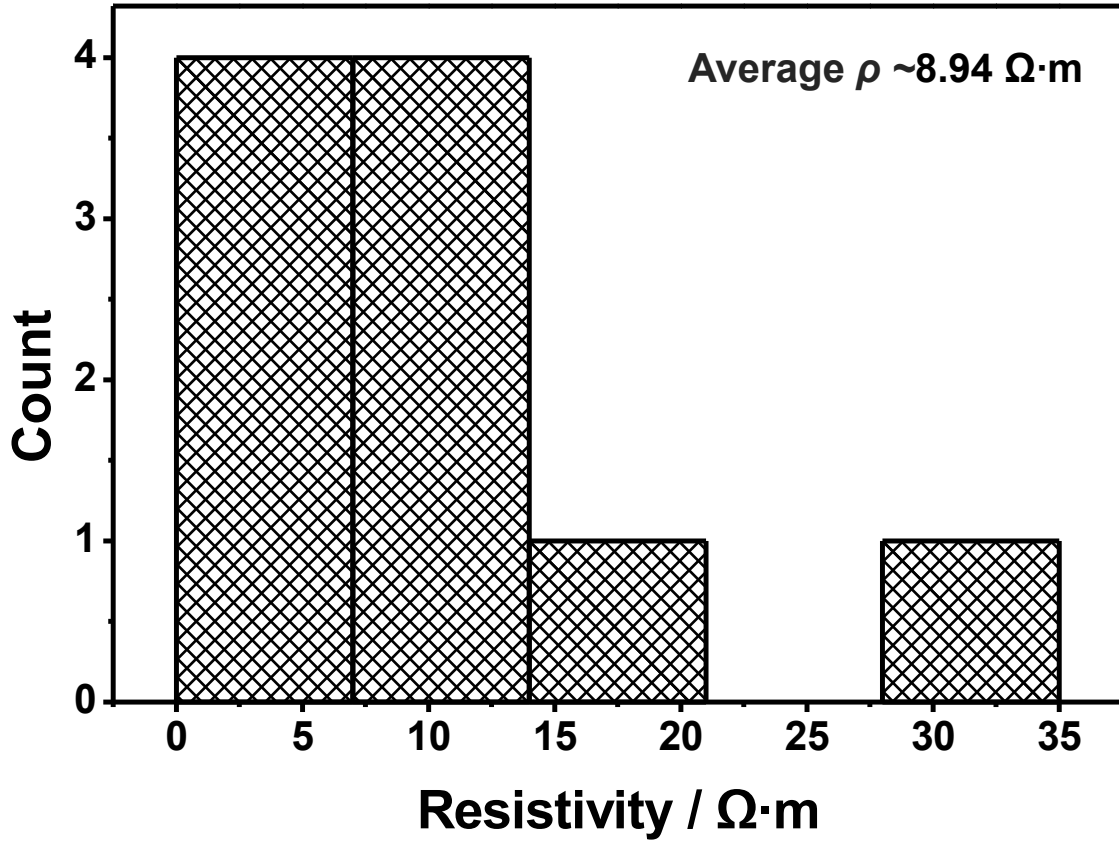


Fig. S39.

Temperature-programmed desorption (TPD) of ammonia from the surface of material **2**, **3** and anatase. The desorption peak at lower temperature regime ($< 300\text{ }^{\circ}\text{C}$) is assigned to weak acidic sites, and the peak at higher temperatures ($>300\text{ }^{\circ}\text{C}$) is attributed to the strong acidic sites. On the basis of desorption temperatures of ammonia, material **2** predominantly possesses strong acidic sites, while **3** possesses both weak and strong acidic sites. It has been previously reported that desorption of ammonia from TiO_2 surface occurs at $222\text{ }^{\circ}\text{C}$ when the ammonia was absorbed at $100\text{ }^{\circ}\text{C}$ ¹⁰. These results are consistent with the desorption data at the lower temperature region in **3** and anatase. Overall, **3** exhibits hybrid surface properties, which arise from both material **2** and TiO_2 .



$$R_S = R/(L/W) = R/(3.0) = 5.94 \times 10^7 \Omega / 3.0 = 2.0 \times 10^7 \Omega$$

$$\rho = R_S \cdot t = 2.0 \times 10^7 \times 398.6 \text{ nm} = 8.0 \Omega \cdot m$$

$$\sigma \text{ (Conductivity)} = 1/\rho = 0.13 \Omega^{-1} \cdot m^{-1}$$

Fig. S40.

Plot of the statistics of ten different devices fabricated from **3** as a function of resistivity (ρ).

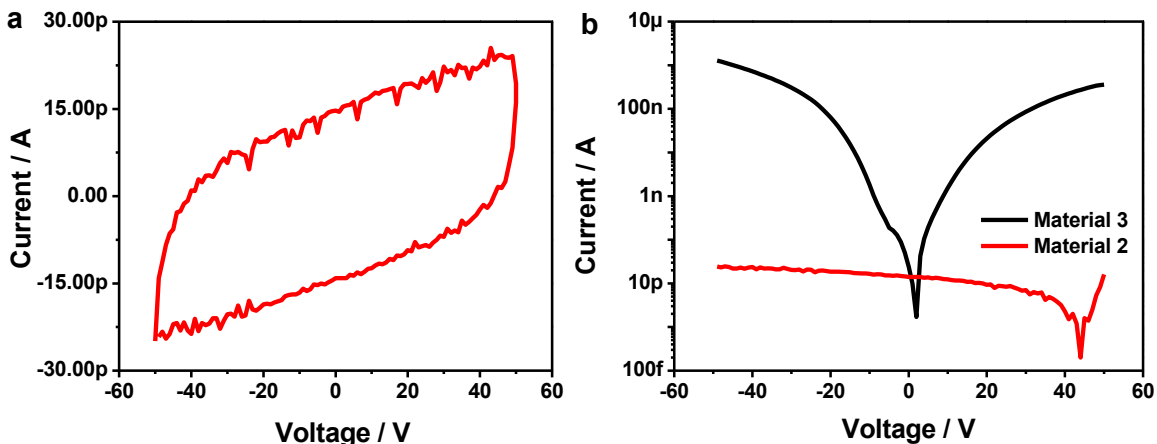


Fig. S41.

(a) Linear-scale plot of the I-V curve of material **2**. The measured current is close to the lower limit of the system, indicating a low electrical conductivity of **2**; (b) Log-scale I-V curves of Material **2** and **3**, showing the current response is much higher in **3**. The calculated conductivity of **2** and **3** is $1.1 \times 10^{-5} \Omega^{-1} \cdot \text{m}^{-1}$ and $4.2 \times 10^{-2} \Omega^{-1} \cdot \text{m}^{-1}$, respectively. This indicates the hybrid molecular boron oxide material (material **2**) is not very conductive, however, when metal oxides are incorporated, its conductivity is much improved (material **3**). The possible explanation for the conductivity of material **3** can be a result of the creation of charge transfer between the hybrid molecular boron oxide material and metal oxides¹¹. In addition, increasing carrier concentration by cross-linking B₁₂-based clusters to TiO₂ can be another reason for the improved conductivity¹².

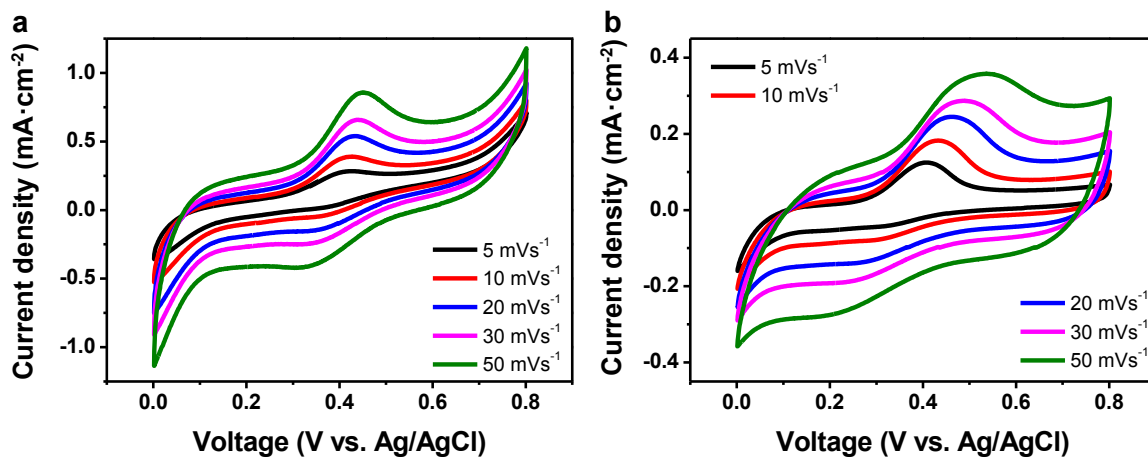


Fig. S42.

Cyclic voltammograms (CV) of (a) material 3 and (b) Commercial TiO_2 at different scan rates.

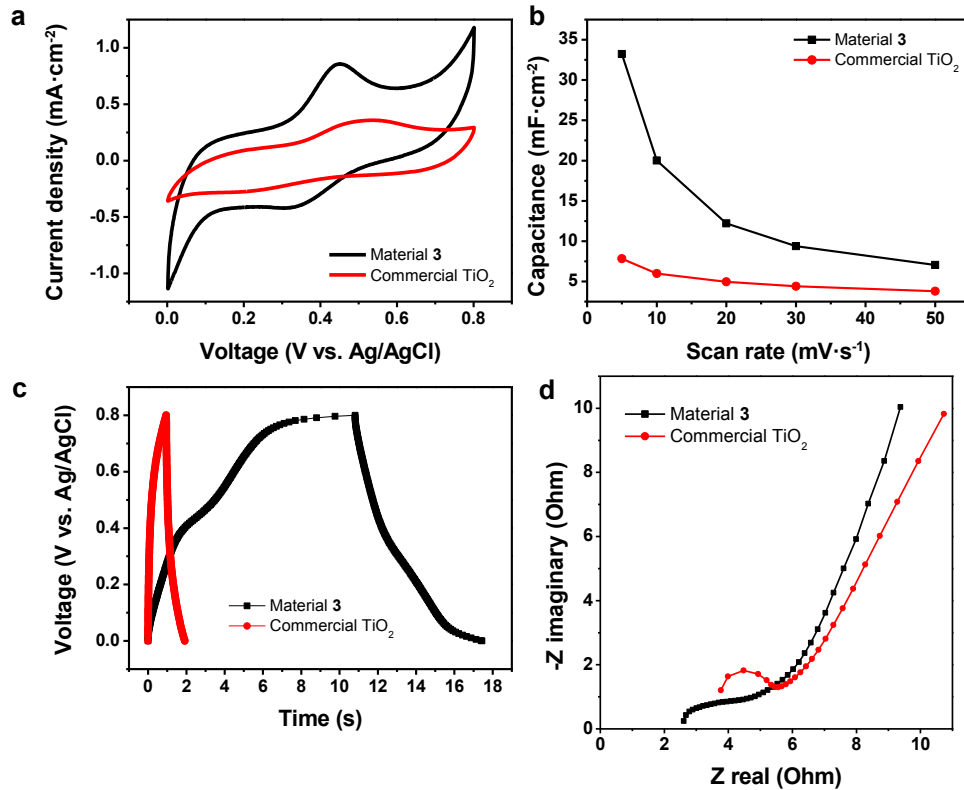


Fig. S43.

Three-electrode electrochemical cell measurements of material **3** and commercial TiO₂. (a) CV curves at a scan rate of 50 mV/s; (b) Areal capacitance as a function of scan rates; (c) Galvanostatic charge/discharge curves; (d) Nyquist plots. Compared to commercial TiO₂, material **3** has larger integrated area along with the higher current response, and its calculated areal capacitance of electrodes as a function of scan rate is much larger than commercial TiO₂ (Fig. S43a and b). Moreover, galvanostatic charge/discharge curve of **3** is significantly prolonged over the pristine TiO₂ (Fig. S43c). Electrochemical impedance spectroscopy (EIS) is further studied to evaluate the capacitive characteristics of electrode materials. In the Nyquist plots, the intercept at the real axis in the higher frequency region represents the equivalent series resistance (ESR), which arises from the electric resistance of the electrode material and the interface resistance. Material **3** reveals a lower ESR than that of the commercial TiO₂, implying an improved electrical conductivity in **3** (Fig. S43d). In addition, the straight line of **3** in the lower frequency area is steeper than that of TiO₂, representing a lower diffusion resistance and an ideal polarizable capacitance. Overall, the results show the electrochemical performance of **3** is substantially improved than TiO₂ as an electrode for supercapacitors. The areal capacitance of the materials (C_A) was calculated using the formula

$$C_A = \frac{1}{\nu A (V_f - V_i)} \int_{V_i}^{V_f} i(V) dV$$

, where i is the current response (mA), $V_f - V_i$ is the potential window (V), ν is the scan rate (V/s), and A is the footprint area of the electrode in three-electrode measurements.

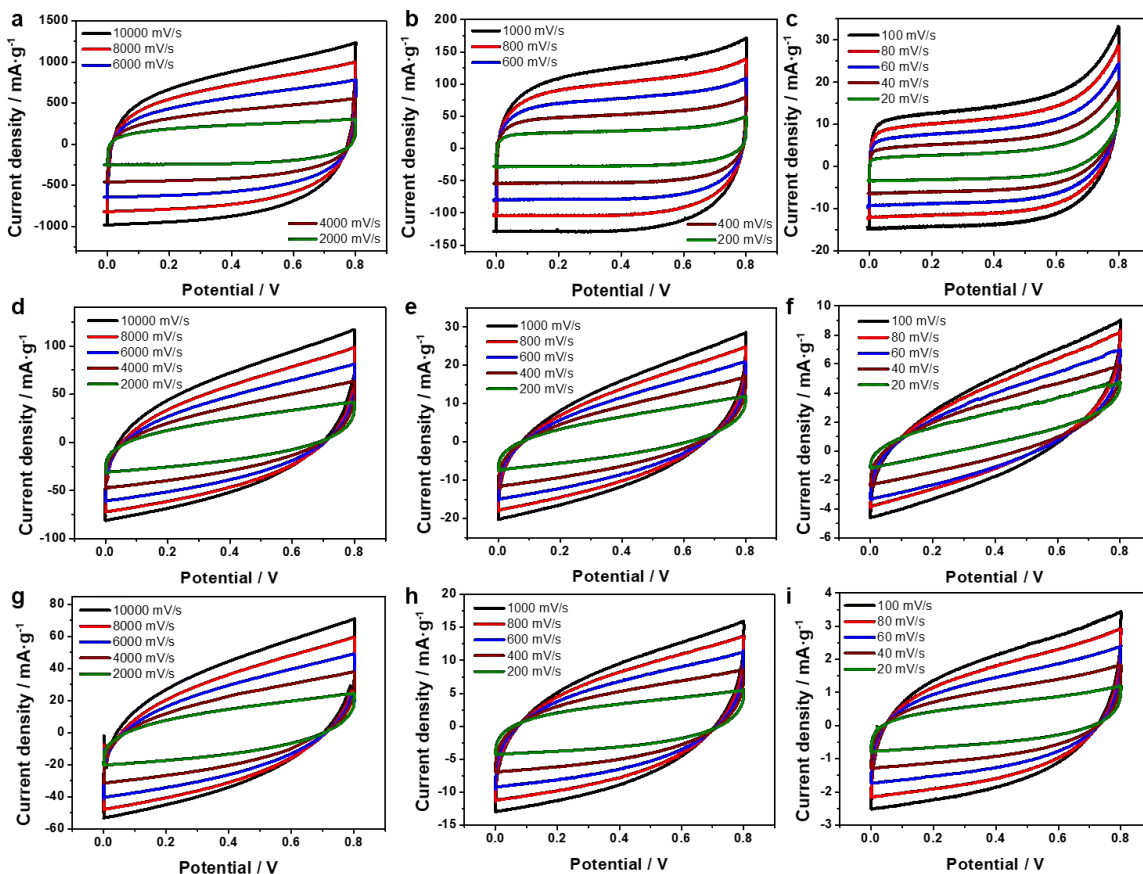


Fig. S44.

Cyclic voltammograms (CV) of (a-c) material **3**, (d-f) anatase, and (g-i) rutile TiO₂ at scan rates from 20 mV/s to 10,000 mV/s. **3** exhibits much enhanced performances at each scan rate, featuring much larger integrated area along with the higher current responses than both forms of TiO₂. Importantly, material **3** shows more rectangular CV profiles even when tested at an ultrafast scan rate of 10,000 mV/s, indicating its excellent rate capability.

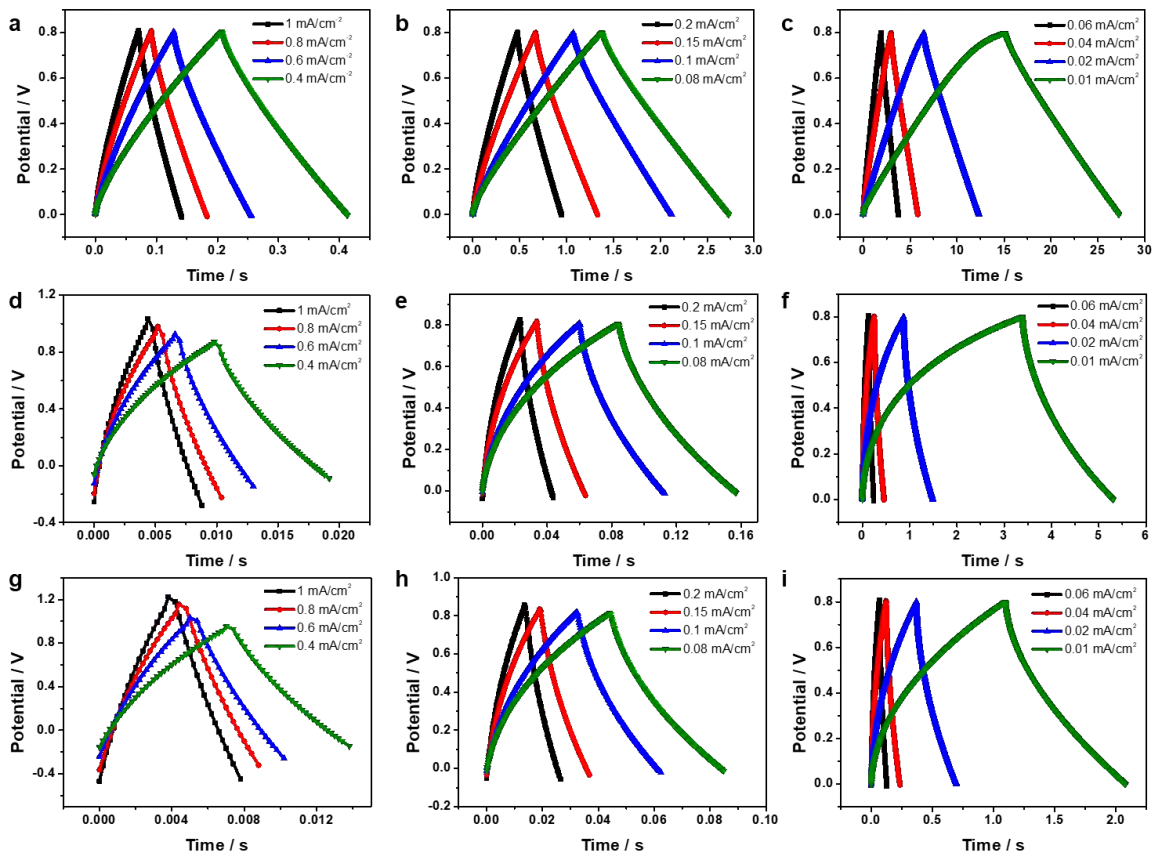


Fig. S45.

Galvanostatic cycling charge/discharge profiles of (a-c) material **3**, (d-f) anatase, and (g-i) rutile TiO_2 at different current densities. At each current density, the charge/discharge curves of **3** are dramatically prolonged over both forms of TiO_2 .

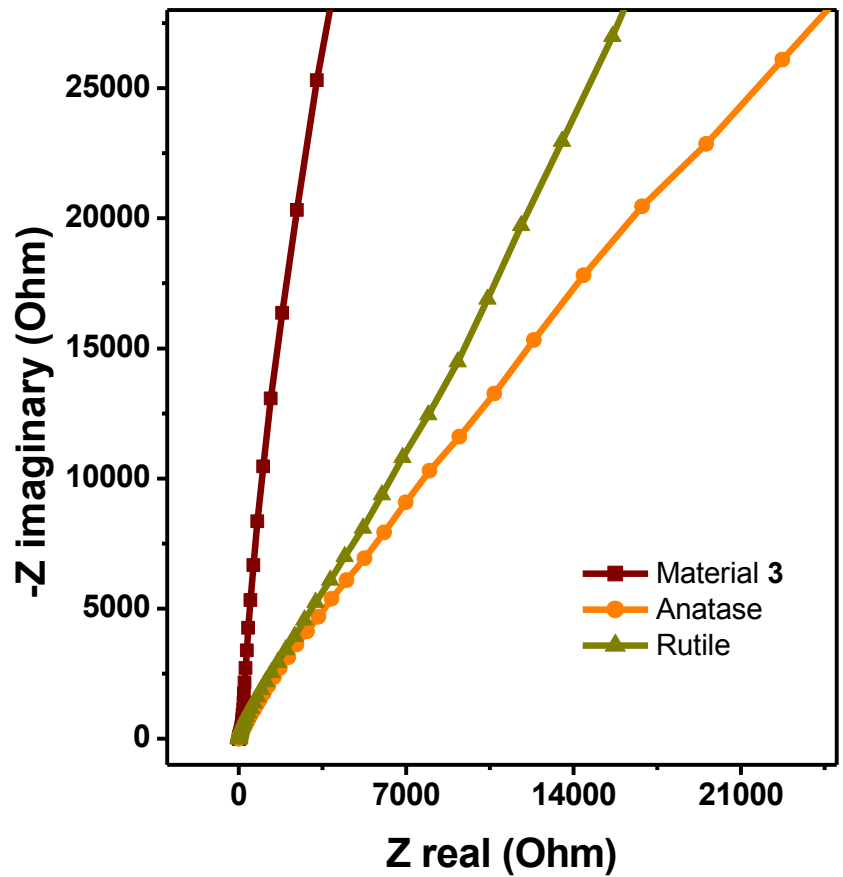


Fig. S46.

Nyquist plots of material **3**, anatase, and rutile TiO₂, showing the straight line of **3** in the lower frequency area is much steeper than that of both forms of TiO₂. It represents a lower diffusion resistance and an ideal polarizable capacitance in **3**.

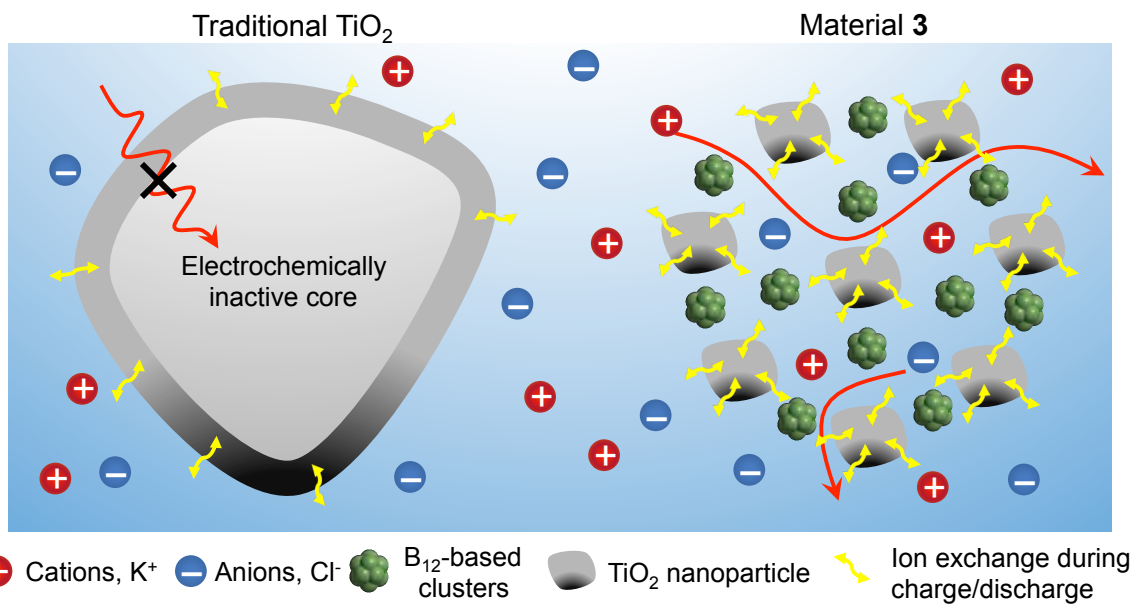


Fig. S47.

A schematic illustration of electrochemical processes in TiO₂ vs. material **3**. Material **3** enables the full utilization of TiO₂ surfaces whereas in the traditional TiO₂ only the external surfaces are available for charge storage.

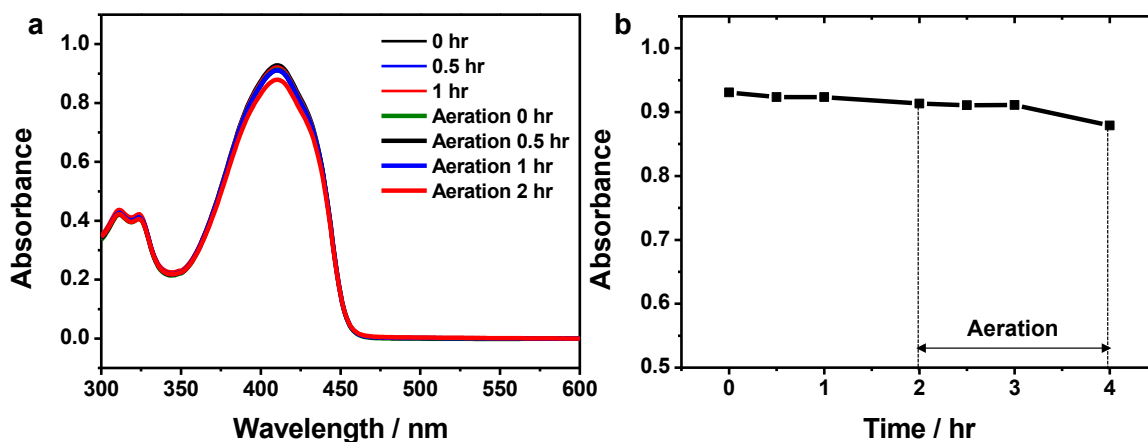


Fig. S48.

(a) Control UV-Vis spectrum depicting the progression of the consumption of DPBF in the presence of **2** and irradiation with red (~ 630 nm) LED lights. DPBF is a sensitive probe for ROS, and a decrease in its absorbance at 410 nm is indicative of the production of ROS. Even after aeration of the reaction mixture, decomposition of DPBF was barely observed, indicating the absence of photocatalytic activity of **2**; (b) a chart showing the rate of consumption of DPBF.

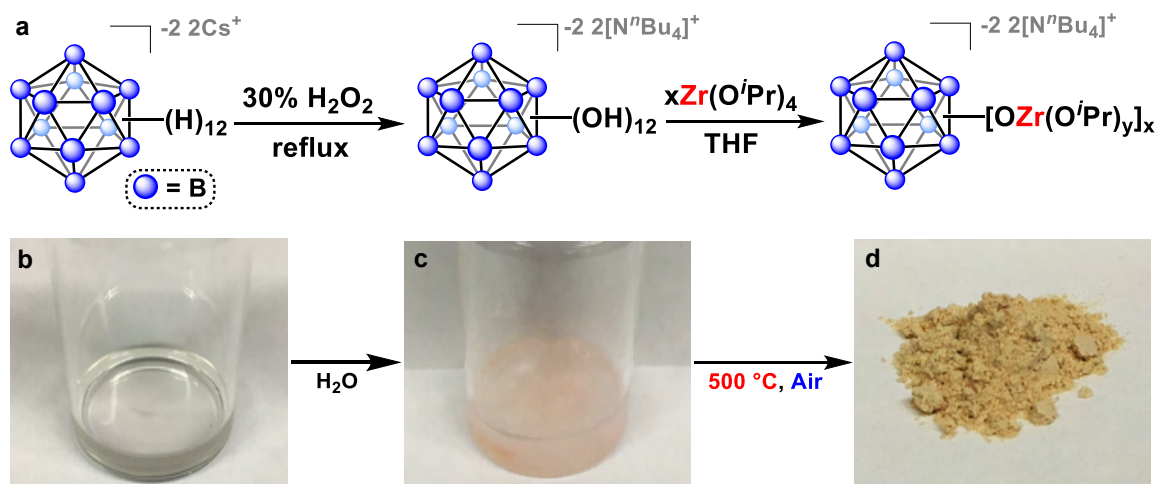


Fig. S49.

(a) Synthetic route towards the synthesis of material **4** utilizing the robust polyhedral boron cluster $[N^n\text{Bu}_4]_2[\mathbf{1}]$ as a key precursor. A reaction of $[N^n\text{Bu}_4]_2[\mathbf{1}]$ with $\text{Zr}(\text{O}^i\text{Pr})_4 \cdot i\text{PrOH}$ in THF produces a clear solution (**b**), which is subsequently hydrolyzed to form a pink gel (**c**). After calcining at $120\text{ }^\circ\text{C}$, the now brown solid is annealed at $500\text{ }^\circ\text{C}$ in air to produce material **4** as a light brown solid (**d**).

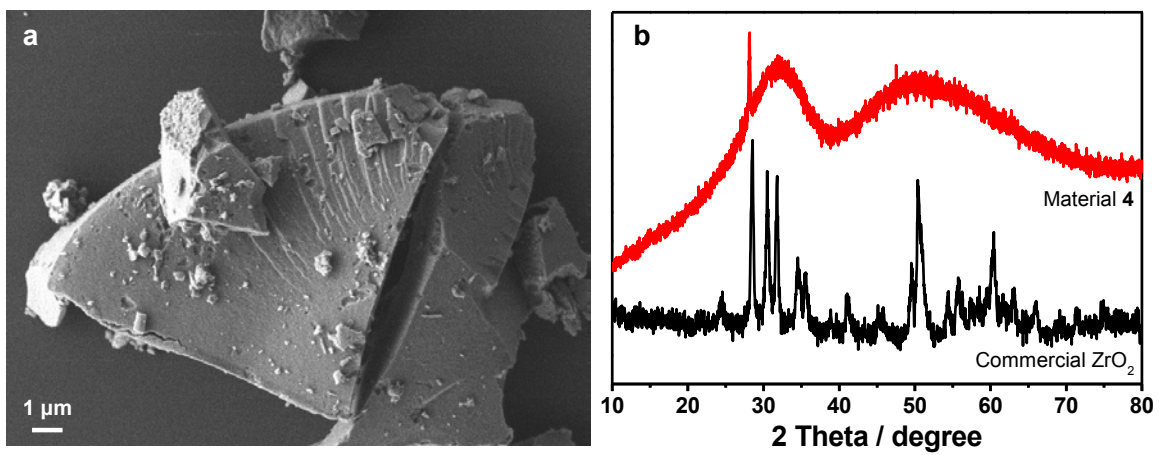


Fig. S50.

(a) SEM image of material 4; (b) PXRD pattern of material 4, with ZrO₂ control.

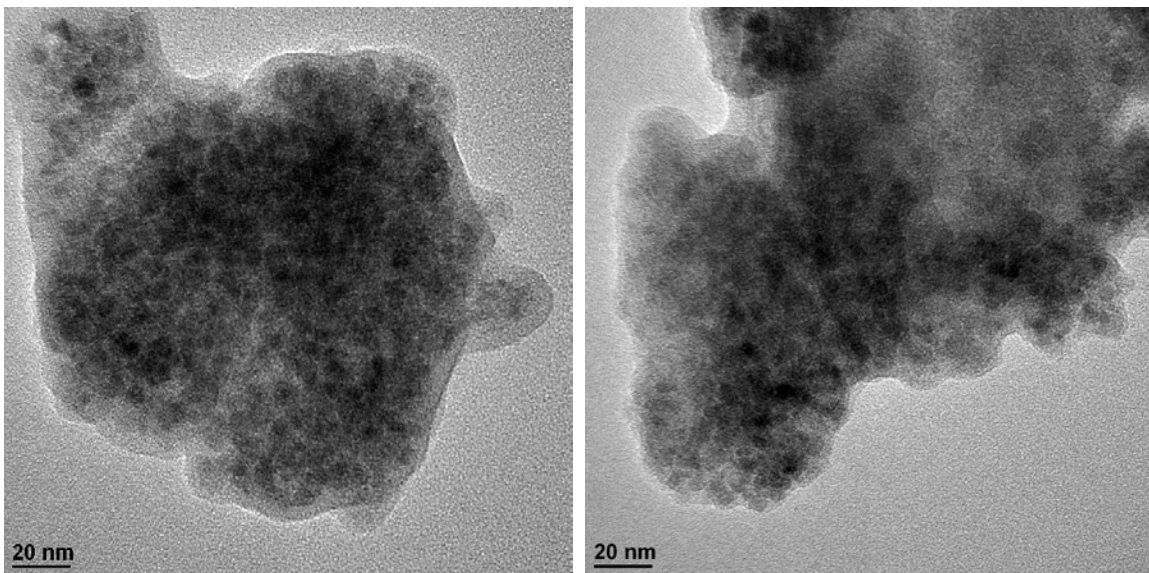


Fig. S51.
High-resolution TEM images of material **4**, showing the similar cross-linked morphology as the previous case of material **3**.

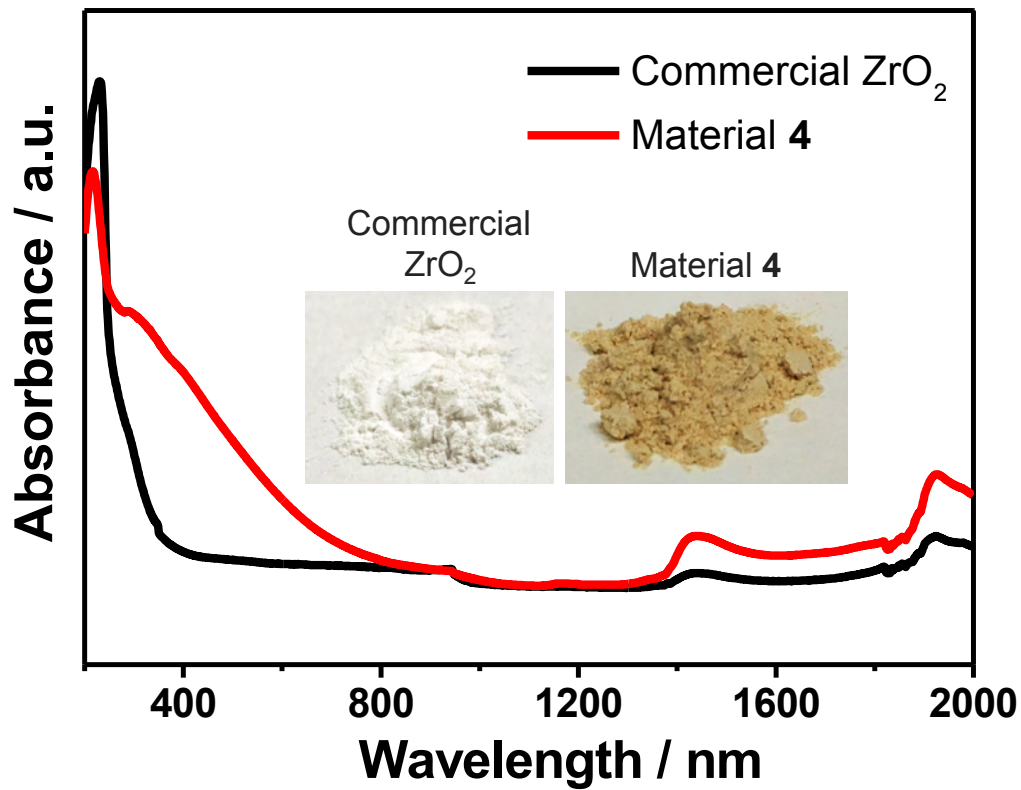


Fig. S52.
Diffuse-reflectance UV-Vis data for material 4, plotted with data for ZrO₂ to highlight the difference in light absorption properties of the materials.

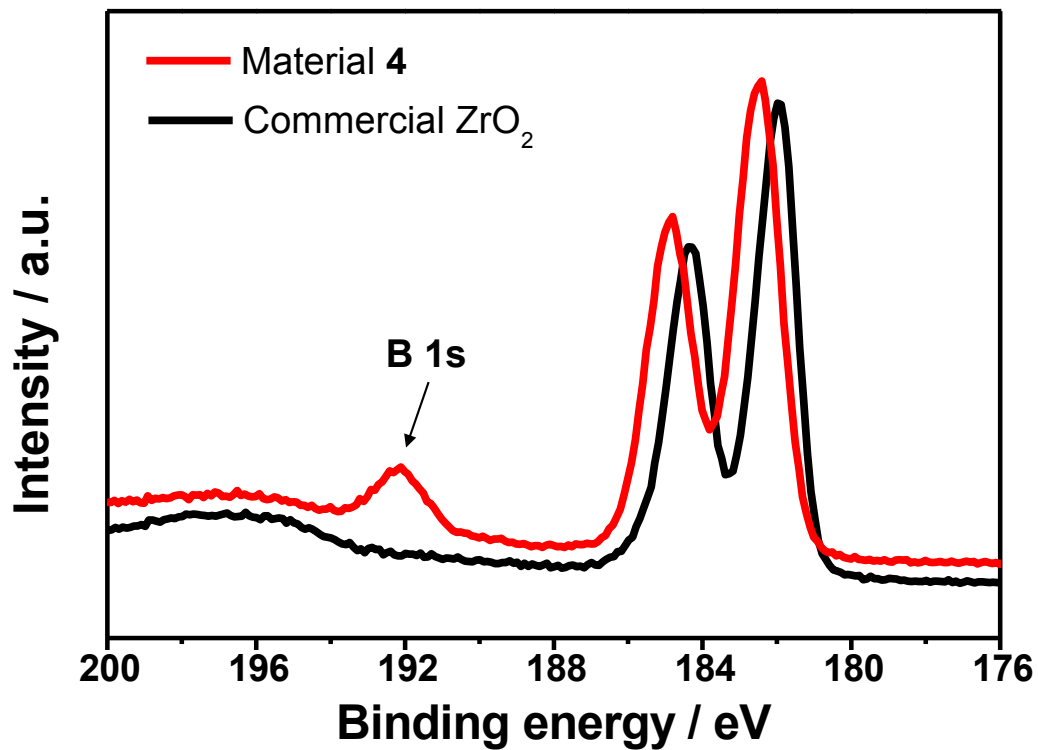


Fig. S53.

The zirconium *3d* region of material **4** shows well-resolved spin-orbit components at 182.4 eV and 184.8 eV, indicating Zr⁴⁺. The boron *1s* region is overlapping with Zr *3d* region, but material **4** clearly shows a boron *1s* peak at 192.1 eV.

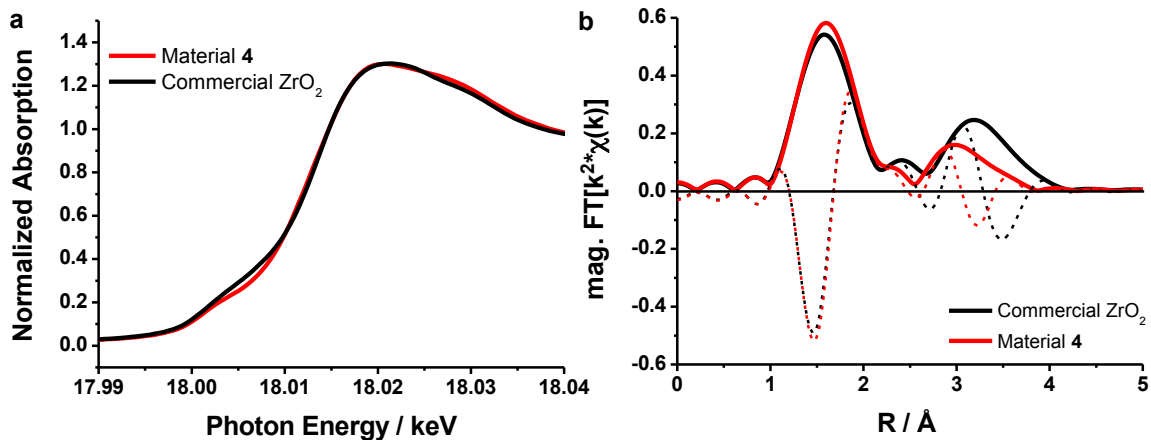


Fig. S54.

a, XANES measurements on material **4** were compared to that measured for ZrO₂. The Zr K edge structure for material **4** matches that found for zirconia, confirming the presence of zirconium exclusively in the 4+ oxidation state. **b**, The k-squared weighted EXAFS function of material **4** and ZrO₂. From this data, an average Zr–O bond distance of 2.14 Å for ZrO₂ in material **4** can be extracted.

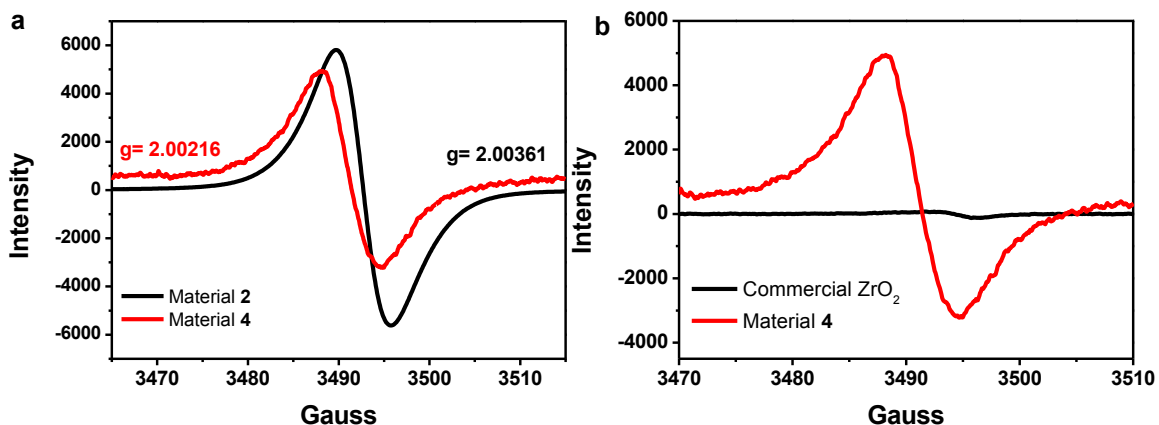


Fig. S55.

(a) Electroparamagnetic resonance (EPR) spectroscopy at room temperature of materials **2** and **4**. Each material produces a peak, with corresponding g -values of 2.00361 and, 2.00216 very close to that found for single molecular boron cluster radicals. The origin of the paramagnetism is related to **2** and the paramagnetism is perturbed when ZrO_2 is introduced to **2**. (b) EPR spectroscopy of material **4** plotted with data for ZrO_2 . While commercial ZrO_2 showed the absence of paramagnetism, material **4** clearly produced a signal arise from cross-linked B_{12} -based clusters.

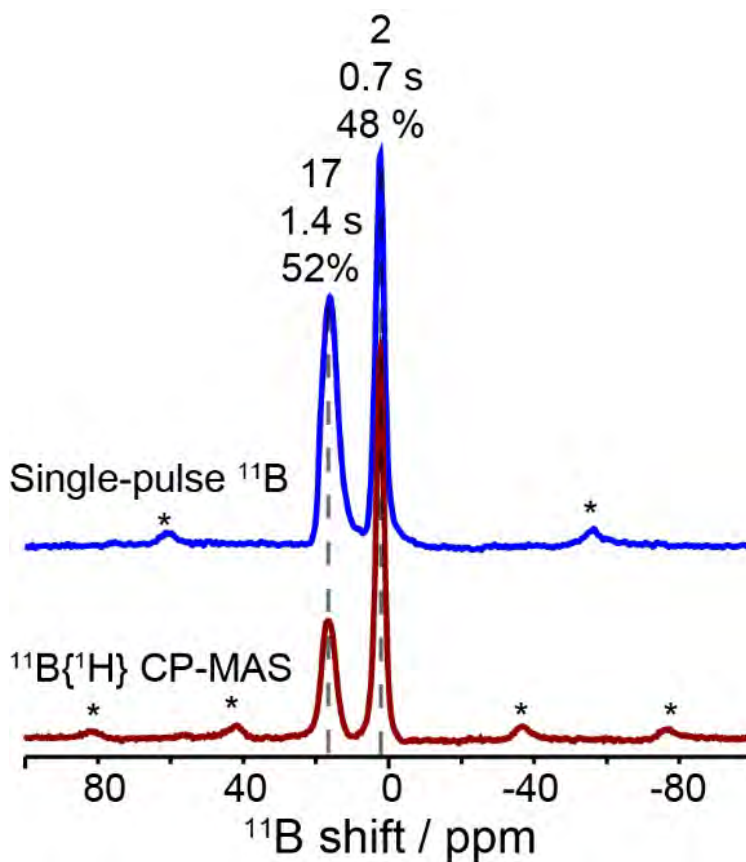


Fig. S56. Solid-state 1D single-pulse ^{11}B MAS NMR (top) and $^{11}\text{B}\{^1\text{H}\}$ CP-MAS (bottom) spectra of material **4** acquired at 18.8 T and 298 K, showing two resolved ^{11}B signals at 2, and 17 ppm, assigned to surface boron clusters, and boron oxide/borates, respectively, and the corresponding percentages are 48 and 52 %, respectively.

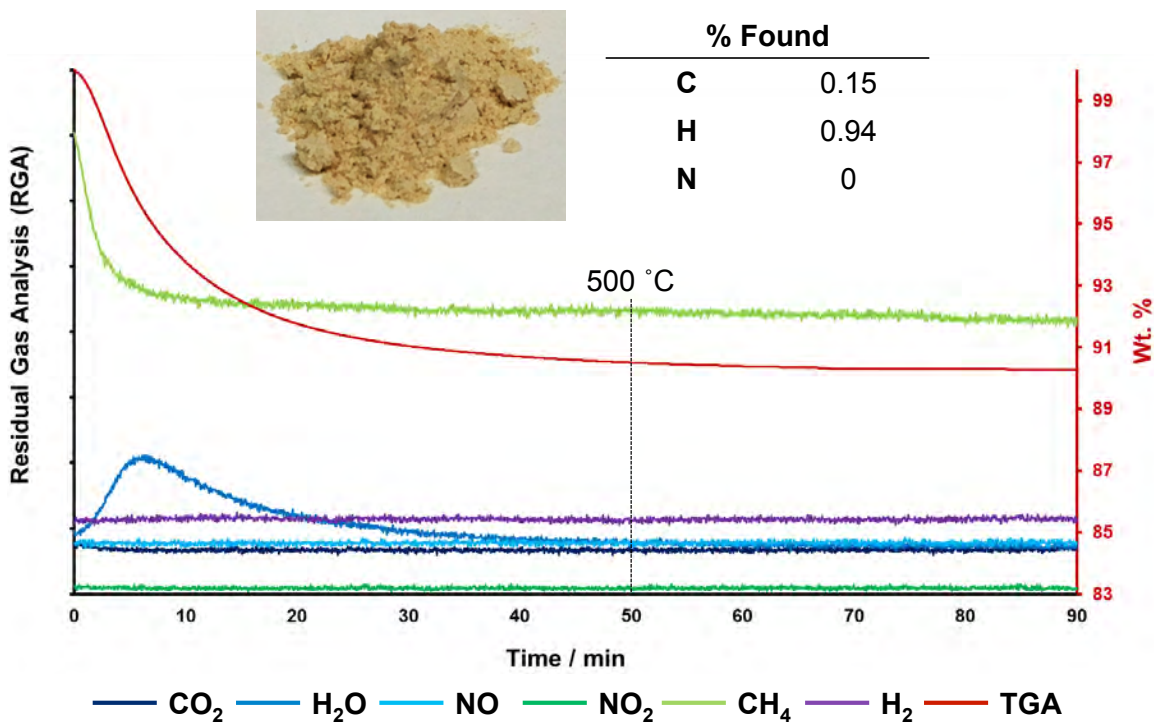


Fig. S57.

TGA-mass spectroscopy (TGA-MS) of material **4**, showing the different mass loss events during the annealing process to form **4**. (A heating rate of $10\text{ }^{\circ}\text{C min}^{-1}$ was used, therefore the scale can be read as: 10 mins = $100\text{ }^{\circ}\text{C}$). The elemental analysis shows material **4** contains $\sim 0.15\%$ of carbon (inset table).

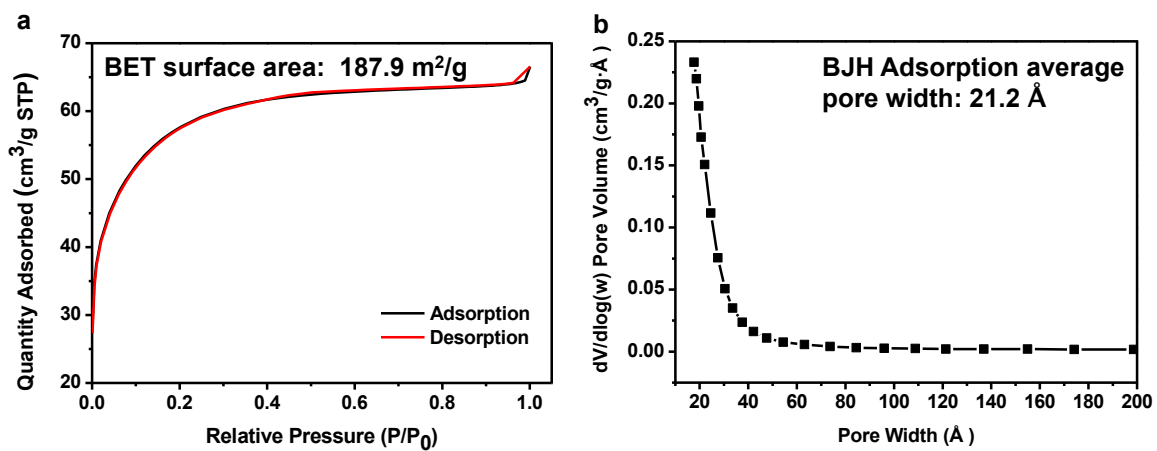


Fig. S58.

(a) Low pressure N₂ adsorption isotherms of material **4**. The Brunauer-Emmett-Teller (BET) surface area is 187.9 m²/g; (b) Calculated pore size distribution of material **4** using the Barret-Joyner-Halenda (BJH) equation.

References

1. Pan, L. *et al.* Hierarchical nanostructured conducting polymer hydrogel with high electrochemical activity. *Proc. Natl. Acad. Sci. U.S.A.* **109**, 9287–9292 (2012).
2. To, J. W. F. *et al.* Ultrahigh surface area three-dimensional porous graphitic carbon from conjugated polymeric molecular framework. *ACS Cent. Sci.* **1**, 68–76 (2015).
3. Feng, N. *et al.* Boron environments in B-doped and (B,N)-codoped TiO₂ photocatalysts: a combined solid-state NMR and theoretical calculation study. *J. Phys. Chem. C* **115**, 2709–1719 (2011).
4. Rorschach, H. E. Nuclear relaxation in solids by diffusion to paramagnetic impurities, *Physica* **30**, 38–48 (1964).
5. Lowe, I. J. & Tse, D. Nuclear spin-lattice relaxation via paramagnetic centers. *Phys. Rev.* **166**, 2, 279–291 (1968).
6. Van, N. *et al.* Oxidative perhydroxylation of [*closo*-B₁₂H₁₂]²⁻ to the stable inorganic cluster redox system [B₁₂(OH)₁₂]^{2-/·-}: Experiment and theory. *Chem. Eur. J.* **16**, 11242–11245 (2010).
7. Zhong, J. -H. *et al.* Quantitative correlation between defect density and heterogeneous electron transfer rate of single layer graphene. *J. Am. Chem. Soc.* **136**, 16609–16617 (2014).
8. Boopathi, S., Narayanan, T. N., Kumar, S. S. Improved heterogeneous electron transfer kinetics of fluorinated graphene derivatives. *Nanoscale* **6**, 10140–10146 (2014).
9. Mao, X., Guo, F., Yan, E. H., Rutledge, G. C., Hatton, T. A. Remarkably high heterogeneous electron transfer activity of carbon-nanotube-supported reduced graphene oxide. *Chem. Mater.* **28**, 7422–7432 (2016).
10. Odriozola, J. A., Heinemann, H., Somorjai, G. A., Garcia de la Banda, J. F., Pereira, P. AES and TDS Study of the adsorption of NH₃ and NO On V₂O₅ and TiO₂ Surfaces: Mechanistic implications. *J. Catal.* **119**, 71 (1989).
11. Saxman, A. M., Liepins, R., Aldissi, M. Polyacetylene: Its Synthesis, Doping, and Structure. *Pro. Polym. Sci.* **11**, 57–89 (1985).
12. Tian, H., Xin, F., Tan, X., Han, W. High lithium electroactivity of boron-doped hierarchical rutile submicrosphere TiO₂. *J. Mater. Chem. A* **2**, 10599 (2014).